technische universität dortmund

MgO/Co/GaAs(001) - An Interface Analysis by Means of XPS and XPD

Dissertation
zur Erlangung des Doktorgrades
der Naturwissenschaften
(Dr. rer. nat.)
der Fakultät Physik
der Technischen Universität Dortmund
vorgelegt von

Karim Shamout
geboren in Detmold

-2018-

1. Gutachter : Prof. Dr. Carsten Westphal

2. Gutachter : Prof. Dr. Mirko Cinchetti

Abgabedatum: 14. September 2018
Eingereicht bei der Fakultät für Physik der Technischen Universität Dortmund

Kurzfassung

Diese Arbeit befasst sich mit den Oberflächen- und Grenzflächeneigenschaften des Mehrschichtsystems MgO/Co/GaAs(001) im Bezug auf Struktur und chemische Bindungen. Im gesamten Forschungsfeld der Spintronik findet sich dieses Schichtsystem wieder, wobei der magnetische Tunnelwiderstand (TMR) als fundamentales Phänomen genutzt wird. Da dieser Effekt sehr empfindlich auf die Grenzfläche von Heterostrukturen reagiert, sind die Photoelektronenspektroskopie (XPS) und die Photoelektronenbeugung (XPD) ideale Untersuchungsmethoden, um die Grenzflächenverbindungen und die lokale strukturelle Umgebung dieses Schichtsystems zu untersuchen. Photonen führen hierbei zu einer Emission von Kernniveau-Elektronen aufgrund des Photoeffekts. Sie liefern elementspezifische Informationen über die benachbarten Verbindungen innerhalb der Probe. Durch Variation des Detektionswinkels, d.h. des Polar- und Azimutwinkels, werden Intensitätsmodulationen innerhalb des XPS-Spektrums aufgrund des Wellencharakters der Elektronen beobachtet. Das Interferenzmuster enthält präzise Strukturinformationen mit chemischer Auflösung. Diese Messungen werden an der Synchrotronstrahlungsquelle DELTA der Technischen Universität Dortmund durchgeführt. Eine Synchrotronquelle liefert nicht nur deutlich höhere Photonenintensitäten, sondern auch eine durchstimmbare Energie. So werden zeitaufwändige Experimente wie XPD innerhalb weniger Stunden durchgeführt und durch Abstimmung der kinetischen Energie der Elektronen wird eine grenzflächensensitive Messung durchgeführt. Darüber hinaus ermöglicht die hohe Auflösung eine genauere Bestimmung der chemischen Verbindungen innerhalb des Mehrschichtsystems. Als Hauptergebnis dieser Arbeit wird die Ga-reiche GaAs(001) c(8×2) Rekonstruktion zugunsten einer Co_3Ga-Legierung an der Co/GaAs-Grenzfläche aufgehoben. Diese kristalline Legierung bildet eine seltene $D0_3$-Struktur zwischen einem As-terminierten GaAs Substrat und dem darauf befindlichen Co(bcc)-Film. Leichte Relaxationen sind hier in jeder Schicht zu beobachten. Da die Gitterkonstante von GaAs perfekt mit der von Co_3Ga übereinstimmt, wird der Schluss gezogen, dass dieses Wachstum substratbedingt ist. As hingegen diffundiert in den Co-Film und bildet amorphe Bindungen. MgO wird anschlieSSend auf die gut geordneten Co-Schichten aufgebracht, wobei das Mg:O-Verhältnis von 1:1 erhalten bleibt. Für MgO-Schichtdicken unter 4 Monolagen bildet MgO keine kristalline Struktur. Bei Schicktdicken von oberhalb 4 Monolage wächst MgO in einer stark verzerrten Halitstruktur auf, aufgrund einer Gitterfehlanpassung zu Co(bcc). Daher wird die minimale Schichtdicke für eine kristallines MgO-Wachstums auf Co(bcc) bestimmt. An der Grenzfläche ist keine Verbindungsbildung oder Co-Oxidation zu beobachten.

Abstract

This work focuses in the surface and interface properties of the multi-layer system MgO/Co/GaAs(001) in terms of structure and chemical bondings. This system is found throughout the research field of spintronics wherein the tunneling magnetoresistance (TMR) effect is considered to make use of the electrons' spins. Since this effect is highly sensitive to the interface of heterostructures, x-ray photoelectron spectroscopy (XPS) and x-ray photoelectron diffraction (XPD) are ideal tools to investigate the sample's interface bondings and its local structural environment. Photons lead to an emission of electrons originating from the core-levels of the elements. They yield element-specific information on the near neighboring bondings within the sample. By varying the recording angle, i.e. the polar and azimuth angle, intensity modulations within the XPS spectrum are observed due to the wave character of the electrons. The interference pattern contains precise structural information with chemical resolution.

These measurements are performed at the synchrotron radiation source DELTA at the Technical University Dortmund. A synchrotron source yields not only significantly higher photon intensities but also provides a tunable energy. Hence, time-consuming experiments like XPD are performed within several hours only and by tuning the kinetic energy of the electrons an interface sensitive measurement is carried out. Further, the high resolution allows a more precise determination of the chemical bondings within the multi-layer system.

As a main result of this work, the Ga-rich GaAs(001) c(8×2) surface reconstruction is destroyed in favor of a Co_3Ga alloy at the Co/GaAs interface. This crystalline alloy forms a rare $D0_3$ structure between an As-terminated GaAs(001) substrate and the Co(bcc) film on top of it. It shows slight relaxations in every layer. Since the GaAs' lattice constant matches perfectly to the one of Co_3Ga, it is concluded that this growth is substrate induced. As diffuses into the Co film forming amorphous bondings. MgO is then deposited on the well ordered Co layers preserving the Mg:O ratio by 1:1. For MgO thicknesses below than 4 monolayers MgO forms no crystalline structure. For a thicknesses above 4 monolayers MgO grows in a highly distorted halite structure due to a lattice mismatch to Co(bcc). Therefore, the minimum thickness of crystalline MgO growth on Co(bcc) is determined. At the interface no compound formation or Co oxidation is observed.

Contents

1 Introduction **1**

2 Theory **5**
2.1 X-Ray Photoelectron Spectroscopy (XPS) 5
2.1.1 Photoelectric Effect 5
2.1.2 XPS Spectrum 7
2.1.3 XPS Line Shape 8
2.1.4 Surface Sensitivity 15
2.2 X-Ray Photoelectron Diffraction (XPD) 19
2.2.1 XPD Pattern 19
2.2.2 XPD Analysis 24

3 Experimental Aspects **29**
3.1 UHV-chamber 29
3.2 Sample Holder 30
3.3 Sputtergun 32
3.4 Low Energy Electron Diffraction 33
3.5 Electron Beam Evaporator 34
3.6 Synchrotron Light Source DELTA 35

4 Multi-Layer System Characteristics & Preparation **37**
4.1 GaAs 37
4.2 Co/GaAs 41
4.3 MgO/Co/GaAs 43

5 Results & Discussion **45**
5.1 Co/GaAs Interface 45
5.1.1 XPS Analysis 45
5.1.2 XPD Analysis 52
5.1.3 Discussion 61
5.2 MgO/Co interface 65
5.2.1 XPS Analysis 65
5.2.2 XPD Analysis 68

5.2.3 Discussion 74

6 Summary & Outlook **79**
6.1 Summary 79
6.2 Outlook 82

Bibliography **83**

Publications **93**

Acknowledgment **95**

1 Introduction

In search of novel electronic devices not only the charge of the electrons is considered but also the their spins. This leads to the field of spintronic devices which is currently in the focus of present research [1–3]. Possible applications vary from magnetoresistive random access memory (MRAM) to read heads in hard drive disks (HDD) and flexible spintronic devices [4, 5]. A way to realize them is to make use of the tunneling magnetoresistance (TMR) effect. TMR-based devices are called magnetic tunnel junctions (MTJ) consisting of two ferromagnets separated by a thin insulating barrier. In 1975 M. Julliere analyzed tunneling electrons for parallel and anti-parallel magnetizations of the ferromagnets within the Fe/Ge-O/Co multilayer system [6]. A graphic of the TMR effect in a MTJ is shown in Fig. 1.1. He found out that the electric current which tunnels from one ferromagnet to the other through the insulating barrier depends on the magnetization of the Fe and Co electrodes. Their magnetization can be controlled by an external magnetic field. The magnetoresistance (MR) ratio r was defined as

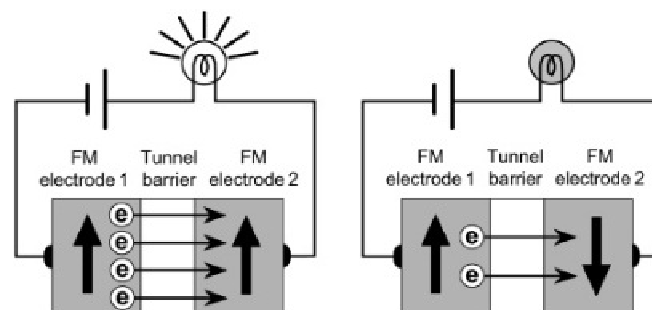

Figure 1.1: Schematic representation of the TMR effect for a parallel (left) and anti-parallel (right) magnetization of the ferromagnets. Depending on the magnetization the amount of electrons tunneling through the insulating barrier can be tuned. Taken from [7].

ratio of the electric current for parallel R_{p} and anti-parallel R_{ap} magnetization $r = \frac{R_{\mathrm{ap}} - R_{\mathrm{p}}}{R_{\mathrm{p}}}$. Julliere determined the MR ratio for the Fe/Ge-O/Co junction to be 14% at $T = 4.2\,\mathrm{K}$. From that moment on, scientists started exploring different ferromagnets and insulators for building MTJs and for understanding the physics behind the TMR process [8, 9]. This led to profound theories and even to the discovery of the giant magnetoresistance (GMR) by P. Grünberg and A. Fert in metallic magnetic multilayers [10, 11]. Therefore, the TMR effect attracted much attention achieving MR ratios of 18% at room-temperature [12, 13]. A main result from recent research is that the ferromagnetic electrodes need to be as flat as possible, i.e. a very low roughness is necessary [14]. This can be achieved by ion beam milling. Otherwise, inhomogeneous barrier thicknesses are produced during the deposition process which lead to a significant reduction in the TMR ratio. Further, the current tunneling through the insulating barrier decays exponentially. Therefore, the insulator needs to be as thin as possible and it needs to be crystalline [15, 16]. MTJs with amorphous insulating barriers like Al_2O_3 do not sufficiently reach high MR ratios. Therefore, crystalline insulating barriers like MgO or $SrTi_2O$ are more promising in terms of spintronic research. For instance, a MR ratio of $r = 1000\%$ was predicted for the Co/MgO/Co multilayer system from first principle electronic structure calculations [17]. It shows one of the largest MR ratios [18]. Yet, experiments did not exceed a ratio of $r \approx 410\%$ [19]. In general, as these films become thinner [20], the interface, surface roughness, and non-bulk typed effects become more important. For example, it has been shown that a single amorphous layer at the interface can lead to a significant reduction in MR ratio [21]. Therefore, a detailed analysis of interface effects is necessary to adjust the current MTJ and TMR understanding and for exploring new materials.

In current research, mainly bcc ferromagnets in (001) orientation such as Co, Fe, CoFeB, or Heusler-alloys are used as electrodes since therein Bloch states are fully spin-polarized at the Fermi level E_{F} [22–24]. These Bloch states are essential to achieve high MR ratios. In case of MgO as an insulating barrier these Bloch states couple to the Bloch states in MgO resulting in MR ratios of 200 %-500 %. A semiconductor at one of the electrodes is necessary to

perform either a spin-injection with a uniform spin orientation or a satisfying spin detection for a fully tunneling analysis [25, 26]. For example, Jiang *et al.* measured the spin-polarization of an injected current into GaAs within the CoFe/MgO/GaAs(001) multi-layer system by quantum well detectors [27]. Therefore, building a MgO/Co/GaAs multi-layer system allows perfectly a verification of the spin-tunneling process [28]. By thinning the deposited MgO and Co layer to thicknesses of $t \leq 12\,\mathrm{ML}$, interface effects like grain building, oxidation, compound or even alloy formation become dominating.

This work focuses on the analysis of the MgO/Co/GaAs multi-layer system. In detail, the chemical and structural properties are analyzed for very thin MgO and Co films on a GaAs substrate. As mentioned above, the focus is on the interfaces, i.e. MgO/Co and Co/GaAs interfaces. By exploring the lower thickness limits in order to epitaxially grow these films, structural distortion or even amorphous/crystalline alloys might form at the interface. An excellent tool to analyze the chemical properties for multi-layer systems is x-ray photoelectron spectroscopy (XPS) [29]. With XPS, element-specific chemical bondings can be observed. Next to XPS, x-ray photoelectron diffraction (XPD) measurements are performed as well. Therein, multiple angle-resolved XPS spectra are recorded. The XPS intensity modulation results in a XPD pattern from which precise structural information is obtained [30–32]. All measurements within this work were performed at a synchrotron radiation source since the x-ray photon energy is tunable and higher photon intensities are provided. Thus, films with various thicknesses and their buried interfaces can be probed [33, 34].

This thesis is divided into five main chapters. The first chapter 2 provides a theoretical background for the XPS and XPD measurements and analysis. Therein, the main theoretical background is provided to understand the photoemission process and the XPD analysis performed in this work. In chapter 3 the experimental setup is described. All experiments within this work are performed *in-situ* in an ultra-high vacuum chamber. Detailed information on the multi-layer preparation is given in chapter 4. Then, all results and their discussion are addressed in chapter 5. Therein, the results for each interface are shown and

discussed separately. In chapter 6 the results are summed up and an outlook on measurements, which will be performed in future, is provided.

2 Theory

2.1 X-Ray Photoelectron Spectroscopy (XPS)

2.1.1 Photoelectric Effect

X-ray photoelectron spectroscopy (XPS) is based on the photoelectric effect discovered by Heinrich Hertz in 1887 [35]. The photoelectric effect is also referred to as the Hallwachs effect, since Hertz's assistant Wilhelm Hallwachs provided in-depth knowledge with his experimental work [36]. In 1905, Albert Einstein was able to theoretically explain this effect and was then honored with the Nobel Prize in 1921 [37]. According to Einstein, light does have wave- and particle-characteristics. The light particle is an energy quantum called photon with an energy of $E_{\mathrm{Ph}} = \mathrm{h}\nu$. Therefore, the energy is related to the frequency of light ν by the Planck constant h. A photon can be absorbed by bonded electrons in a solid state. If Eq. 2.1 is fulfilled, these electrons have enough energy to be emitted from the solid with a kinetic energy of E_{kin} [37]:

$$\mathrm{h}\nu \overset{!}{\geq} E_{\mathrm{B}} + \phi_{\mathrm{A}} \tag{2.1}$$

$$\rightarrow E_{\mathrm{kin}} = \mathrm{h}\nu - (E_{\mathrm{B}} + \phi_{\mathrm{A}}). \tag{2.2}$$

The photon energy $\mathrm{h}\nu$ must be greater than the binding energy E_{B} and the work function ϕ_{A} combined in order to emit an electron. The binding energy E_{B} is the energetic difference of the Fermi level E_{F} and the binding state such as $1s$, $2s$, $2p$ etc. The work function $\phi_{\mathrm{A}} = E_{\mathrm{Vac}} - E_{\mathrm{F}}$ needs to be overcome to transfer the electron into a vacuum state. The work function differs for each material and is

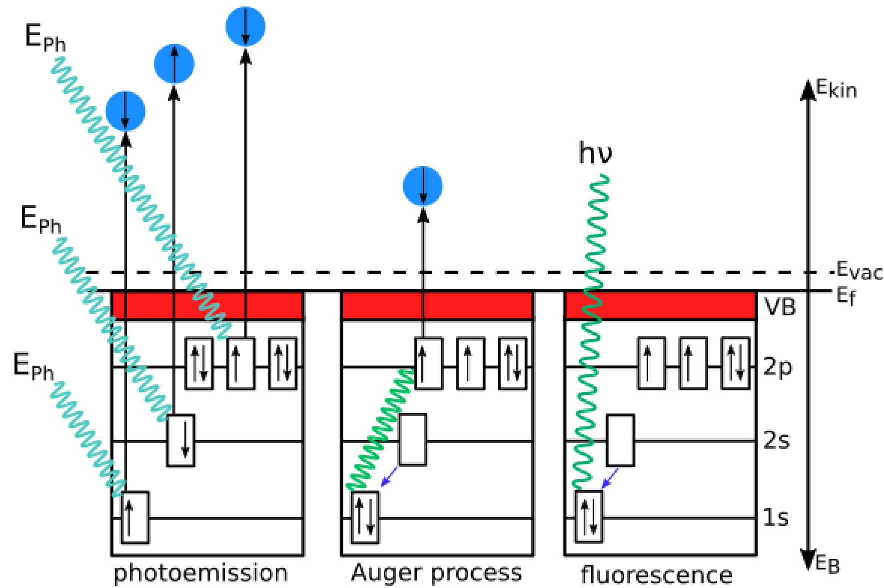

Figure 2.1: Relaxation processes after the photoemission process. The incoming photon energy of E_{Ph} is absorbed by an electron so that it is emitted from the solid state (left). The electron vacancy is refilled by an electron with a lower binding energy. The energy difference can be transferred to another electron causing it to be emitted. This process is called Auger process (center). The free energy can also be emitted from the solid state as fluorescence (right).

roughly $\phi_A = 2\,\text{eV} - 5\,\text{eV}$ [38]. Surplus energy from the photon is converted into the electron's kinetic energy.

The electron is emitted due to the photoelectric effect and the origin atom is ionized. Then relaxation processes occur in the solid state. They are shown in Fig. 2.1. The image on the left shows the photoemission process and the electron vacancies in the solid state. For instance, after emitting an electron from the $1s$ energy level a weaker bonded electron from the $2s$ orbital can relax to the $1s$ orbital. This relaxation is indicated with a blue arrow in the middle and in the right image. A distinct energy is then released that depends on the energetic difference of the initial and final energy only. This energy can either be observed as fluorescence as shown in the right image or absorbed by another electron as shown in the middle image. In this example, free energy is absorbed by an electron from the $2p$ orbital, so that it is emitted according to Eq. 2.2. The

emitted electron always has the same distinct kinetic energy, as the excitation energy only depends on the energetic difference of the involved orbitals. This process is called Auger process [39]. The probability for fluorescence or the Auger process depends on the atomic number Z of the probed material. The dominating relaxation process for $Z \leq 30$ is the Auger effect and for $Z \geq 60$ the fluorescence process occurs in most cases.

2.1.2 XPS Spectrum

Electrons with kinetic energies up to the energy $\mathrm{h}\nu - \phi_\mathrm{A}$ are emitted from the solid state. Therefore, the intensity of electrons is recorded as a function of their kinetic energy. This process is illustrated in Fig. 2.2. Mainly, electrons are either strongly bonded in core-levels or weakly bonded in the valence band. The weak binding energy of the valence band electrons results in kinetic energies near to the Fermi level E_F. Core-level electrons form distinct intensity lines. For an XPS measurement, it is necessary to use monochromatic light. Otherwise, these distinct core-level energy lines become continuous and a distinction of core-levels peak is not possible.

Depending on the incoming light, photoelectron spectroscopy can be distinguished into three different areas. The first one is ultraviolet photoelectron spectroscopy (UPS) whereas the energy is in range of $E_\mathrm{Ph} = 5\,\mathrm{eV} - 50\,\mathrm{eV}$. UPS is mainly used to analyze weakly bonded valence band electrons. The second one is x-ray photoelectron spectroscopy (XPS) with typical excitation energy in the range of $E_\mathrm{Ph} = 50\,\mathrm{eV} - 1500\,\mathrm{eV}$. With XPS, core-level electrons that are strongly bonded to the atoms are analyzed. An even higher energy of $E_\mathrm{Ph} \geq 1500\,\mathrm{eV}$ leads to the field of hard x-ray photoelectron spectroscopy (HAXPES). With this technique, thick films can be analyzed due to the larger inelastic mean free path of electrons, which is discussed below.

In order to yield quantitative information on the sample, a core-level peak is recorded in high resolution and the line shape is analyzed.

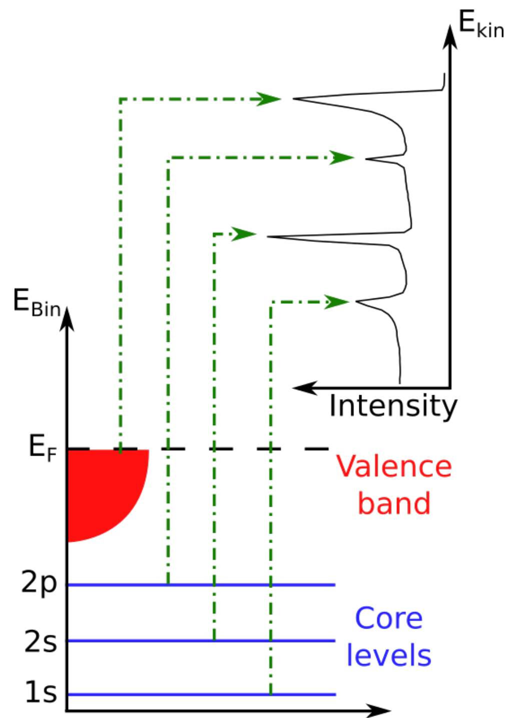

Figure 2.2: Core-levels (blue) have higher binding energies and form distinct energy lines. The valence band (red) is located near to the Fermi level E_F and is continuous. After excitation (green) the electron intensities are recorded as a function of their kinetic energies.

2.1.3 XPS Line Shape

Scanning over the full energy range of an XPS spectrum results in a survey spectrum. A survey spectrum serves as an overview of all the orbitals of the chemical elements within the analyzed sample that can be observed with the used excitation energy. Thus, it provides qualitative chemical information on the sample. It can be used to identify contaminations and undesired elements. In Fig. 2.3 a GaAs XPS survey spectrum recorded at an excitation energy of $\mathrm{h}\nu = 650\,\mathrm{eV}$ is shown. Clearly visible, O 1s and C 1s peaks arise indicating a strong contamination. Further, all observable Ga and As orbitals are labeled. Core-level electrons bonded higher than $E_\mathrm{B} \geq 650\,\mathrm{eV}$ can not be excited.

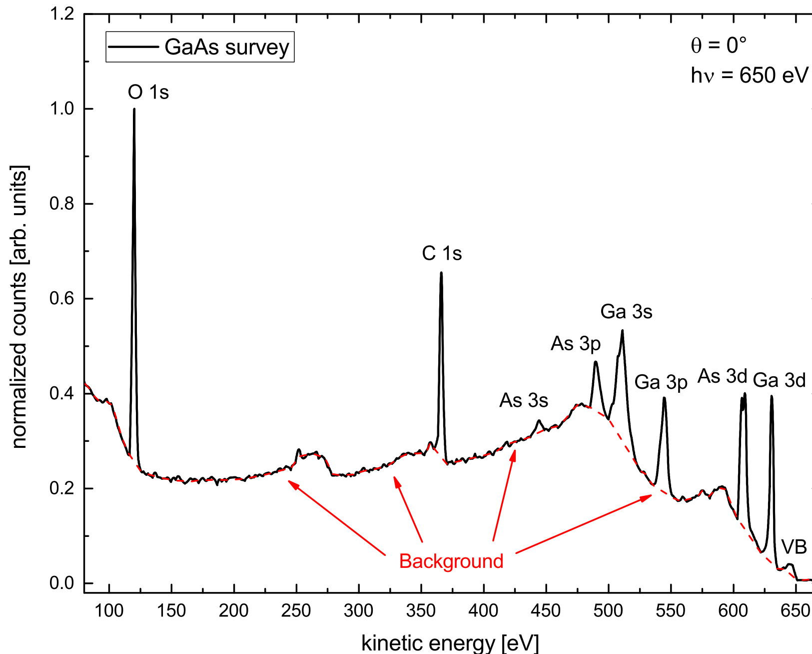

Figure 2.3: GaAs XPS survey spectrum recorded at a polar angle of $\theta = 0°$ and an incoming photon energy of $\mathrm{h}\nu = 650\,\mathrm{eV}$. Since the sample is not cleaned the O 1s and C 1s peaks are dominant. The background due to inelastic scattering is visualized in a dashed red line.

Most of the excited electrons lose some of their energy due to inelastic scattering like one-electron excitation or plasmon scattering. These electrons are recorded as background at lower kinetic energies than expected. In order to quantitatively analyze the line shape of a high resolution core-level peak, this background needs to be subtracted. In general, there are two different background models that need to be considered - the Shirley-background $B_{\mathrm{S}}(E)$ and the Tougaard-background $B_{\mathrm{TH}}(E)$ [40, 41]. The Shirley-background is defined as:

$$B_{\mathrm{S}}(E) = \int_{E}^{\infty} S(E')\mathrm{d}E' + c. \tag{2.3}$$

This background model turned out to be a successful approximation for most elements. For metals, an intrinsic asymmetry in the core-level peak arises. Since the Fermi level E_{F} lies in the conduction band, there is a high amount of unoc-

cupied states directly above the Fermi level E_F and a high amount of occupied states directly below E_F. Therefore, electron-hole pairs can easily be produced with lifetimes of a few femtoseconds [42]. Consequently, the excited electrons lose a small portion of their energy to produce these electron-hole pairs. This continuous process results in an asymmetry to lower binding energies in the XPS signal. To calculate the background for these elements correctly, a Tougaard-background is appropriate. It considers the energy loss function $F(E)$ of the analyzed material by convolving it with the measured spectrum $S(E)$ [43]:

$$B_\mathrm{TH}(E) = \lambda \times \int_E^\infty F(E' - E) S(E') \mathrm{d}E'. \tag{2.4}$$

The energy loss function $F(E)$ can either be calculated or determined by electron energy loss spectroscopy (EELS). In most cases, this function is unknown, since the analyzed sample can be harmed by the large energy needed for EELS. As this function also varies depending on the emission angle and on the surface reconstruction, a much more sophisticated approach is to assume a general energy loss function with free parameters and to adjust it to the experimental data. Hence, a five-parameter approximation for $F(T)$ with $T = E' - E$ is introduced [44]:

$$F(T, E_0, C, C', D) = \theta(T - E_0) \frac{B \times (T - E_0)}{(C + C' \times (T - E_0)^2)^2 + D \times (T - E_0)^2}. \tag{2.5}$$

The parameters E_0, C, C' and D can be manually defined or fitted to the experimental data within a least squares fit. Therefore, the Tougaard-background subtraction becomes more challenging compared to Shirley-background but describes the asymmetry, which occurs in metals, more accurately.

Core-level electrons are bonded at a distinct energy level. Yet, the measured XPS line shape of these core-level electrons is remarkably broadened by up to 5 eV depending on the analyzed material. This broadening occurs mainly due to the lifetime of electrons and influences by the apparatus. The resulting line shape of the high resolution XPS spectrum can be described as convolution of a Lorentz-function $L(E, E_0, \omega)$ and Gauss-function $G(E, E_0, \sigma)$. The resulting function is called Voigt-profile $V_\mathrm{G,L}(E, E_0, \sigma, \omega)$. As described previously for the Tougaard-

background, the Voigt-profile needs to be adjusted for an intrinsic asymmetry. Since the intrinsic asymmetry is a physical effect, the Lorentz-function is replaced by a Doniach-Šunjić-function (DS) $D(E, E_0, \omega, \alpha)$ with an asymmetry parameter α. The DS-function converges to the Lorentz-function for $\alpha = 0$ [45]. Hence, the Voigt-profile changes to $V_{\mathrm{G,DS}}(E, E_0, \sigma, \omega, \alpha)$. As the DS-function provides a more general approach, it is used to analyze the line shape of high resolution XPS spectra instead of the Lorentz-function. These functions are given here as:

$$G(E, E_0, \sigma) = \exp\left\{-\frac{1}{2}\left[\frac{(E-E_0)^2}{\sigma}\right]\right\} \tag{2.6}$$

$$D(E, E_0, \omega, \alpha) = \frac{\cos\left[\frac{\pi\alpha}{2} + (1-\alpha)\arctan\left(\frac{E-E_i}{\omega}\right)\right]}{\left((E-E_0)^2 + \omega^2\right)^{(1-\alpha)/2}} \tag{2.7}$$

$$L(E, E_0, \omega) = D(E, E_0, \omega, \alpha = 0) = \frac{1}{2\pi}\frac{\omega}{(E-E_0)^2 + (0.5\omega)^2} \tag{2.8}$$

$$V_{\mathrm{G,DS}}(E, E_0, \sigma, \omega, \alpha) = (G * D) = \int G(\tau, E_0, \sigma, \omega, \alpha) D(E-\tau, E_0, \sigma, \omega, \alpha) \mathrm{d}\tau\,. \tag{2.9}$$

The main variables to adjust the function to the high resolution XPS spectrum are E_0 for the energetic position of the functions maximum, σ for the Gaussian full width at half maximum (FWHM), ω for the Lorentzian FWHM, and α for the DS asymmetry factor. A high resolution XPS spectrum consists of several XPS components whereas each can be described by a Voigt-function.

In general, a solid state is characterized by a periodical arrangement of atoms that chemically bond to each other. The periodicity breaks at the crystal surface and atoms form new bondings due to free dangling bonds [38]. Depending on the electronegativity χ of the bonding atoms, bondings might be either weak with a binding energy of 30 meV like Van-der-Waals bonding or strong like metallic or even ionic and covalent bondings reaching up to 40 eV. In a bonding, the atom with the higher electronegativity χ attracts electrons. Therefore, they are negatively charged and the relative atomic number is reduced. Thus, the binding energy of core-level electrons is reduced due to the repulsive Coulomb force. According to Eq. 2.2, a lower binding energy results in higher kinetic

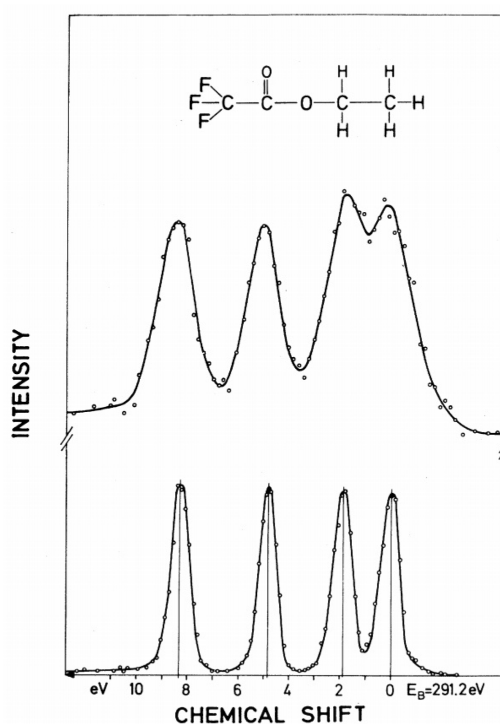

Figure 2.4: XPS spectrum of C 1s in ethyl trifluoroacetate. Due to the different chemical bondings four separated XPS peaks within the C 1s spectrum arise. F with the highest electronegativity causes a chemical shift of up to 8 eV. Taken from [46].

energy. Consequently, for the binding partner with the lower electronegativity χ, the binding energy of its core-level electrons is raised. This effect results in a chemical shift in the XPS signal. In 1981 Kai Siegbahn was honored with the Nobel Prize for his work on clearly identifying the chemical shifts and resolving them [46]. Within his work, he used a monochromatic x-ray source to resolve the chemical shifts within the C 1s XPS spectrum of ethyl trifluoroacetate. The effect is shown in Fig. 2.4. In ethyl trifluoroacetate, high chemical shifts are observable since C forms three bondings to H and F. The C bonding to three H atoms -CH_3 causes a lower C binding energy as the H electronegativity $\chi_\mathrm{H} = 2.20$ is lower than the C electronegativity $\chi_\mathrm{C} = 2.50$ [47]. F is the most electronegative element in the periodic system. Therefore, the bonding to three F atoms -CF_3- causes a higher binding energy since the F electronegativity $\chi_\mathrm{F} = 4.17$ is higher than the C electronegativity [47]. The same procedure can also be applied to a

single or double C-O bonding. As a result, a chemical shift of up to 8 eV occurs in ethyl trifluoroacetate. This example clearly shows that XPS is perfectly suited to observe chemical bondings within the sample.

In addition to the chemical shift, a shift occurs due to the spin-orbit coupling (SOC). The electron spin s and the angular momentum quantum number l couple, whereas the spin s might either be parallel (+) or anti-parallel (-) relatively to the angular momentum [48]. The sum of all electron spins S and angular momentums L result in the total angular momentum quantum number J [49]:

$$S = \sum_k s_k \tag{2.10}$$

$$L = \sum_k l_k \tag{2.11}$$

$$J_\pm = L \pm S\,. \tag{2.12}$$

A higher total angular momentum quantum number results in a lower binding energy, i.e. higher kinetic energy. The energetic difference of the two separated quantum states $\Delta_\mathrm{SOC} = E_{J_+} - E_{J_-}$ depends highly on the material and orbital. Further, the observed states in the XPS spectrum differ in height. The height ratio h_SOC of the XPS components is determined by the order of degeneracy:

$$h_\mathrm{SOC} = \frac{2 \times J_- + 1}{2 \times J_+ + 1}. \tag{2.13}$$

In this work, the orbitals As $3d$, Ga $3d$, Co $3p$, and Mg $2p$ are analyzed. In Tab. 2.1, their height ratios according to Eq. 2.13 and the energetic differences are provided. Therefore, depending on the analyzed orbital the XPS line shape consists not only of one $V_\mathrm{G,DS}$ but of two functions whereas the second one has the same set of (σ, ω, α) parameters. Since the two Voigt functions correspond to the same chemical state, they can be summed up by a single function $V^*_\mathrm{G,DS}$ corresponding to one chemical state:

$$V^*(E) = \underbrace{V_\mathrm{G,DS}(E)}_{J_+} + \overbrace{h_\mathrm{SOC}}^{\text{height ratio}} \times \underbrace{V_\mathrm{G,DS}(E - \Delta_\mathrm{SOC})}_{J_-} \tag{2.14}$$

Table 2.1: Background, curve profile, height ratio h_{SOC} and Δ_{SOC} for each analyzed element in the multi-layer system [50–53].

Element (layer system)	Background	Profile	h_{SOC}	Δ_{SOC} [eV]
As $3d$ (GaAs)	Shirley	$V_{\text{G,L}}$	2:3	0.69
Ga $3d$ (GaAs)	Shirley	$V_{\text{G,L}}$	2:3	0.45
As $3d$ (Co/GaAs)	Tougaard	$V_{\text{G,DS}}$	2:3	0.69
Ga $3d$ (Co/GaAs)	Tougaard	$V_{\text{G,DS}}$	2:3	0.45
Co $3p$ (Co/GaAs & MgO/Co)	Tougaard	$V_{\text{G,DS}}$	1:2	1.10
Mg $2p$ (MgO/Co/GaAs)	Shirley	$V_{\text{G,L}}$	1:2	0.28

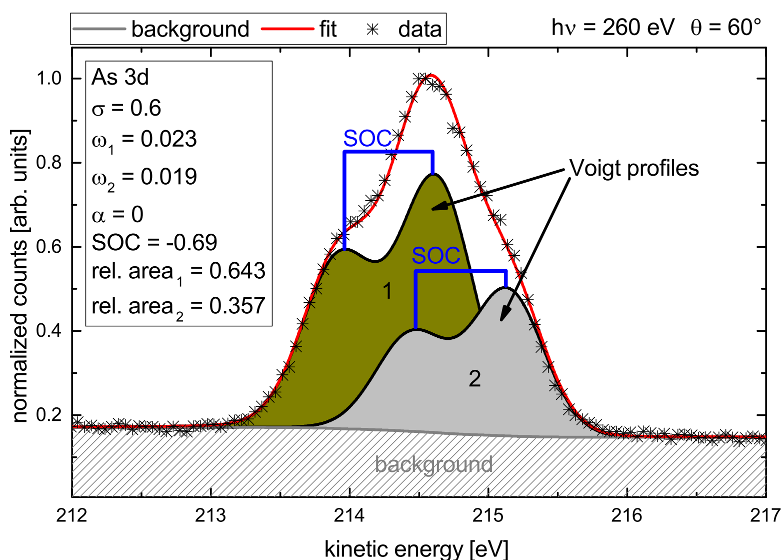

Figure 2.5: High resolution XPS spectra of As $3d$ at $\theta = 60\,^\circ$ and an incoming photon energy of hν = 260 eV. Two Voigt profiles with the parameters specified in the box are necessary to achieve a satisfying least squares fit. The background subtraction was performed with a Shirley function.

In the XPS spectrum, each $V^*(E)$ function corresponds to a chemical state wherein the SOC is considered. A sum of all the chemical shift functions $\sum V_i^*(E)$ with the calculated background $B(E)$ fully describes a high resolution XPS spectrum. In Fig. 2.5 all the discussed effects are shown for the As $3d$ spectrum. Since σ, ω, and α have the same values for an element-specific least squares fit

at $\theta = 0^\circ$ and $\theta = 60^\circ$, only the height of each individual fitting component is varied to achieve a fit to the experimental data. But since the background needs to be adjusted as well, a comparison of $\theta = 0^\circ$ and $\theta = 60^\circ$ with the components' heights can only be misleading. Therefore, the relative area of each component is taken into account.

2.1.4 Surface Sensitivity

In XPS measurements the surface sensitivity can mainly be controlled by the excitation energy E_{Ph} and the emission angle θ, i.e. the polar angle. Depending on the photon energy, excited core-level electrons have a corresponding kinetic energy. The kinetic energy of electrons correlates with the inelastic mean free path $\lambda(E)$ (IMFP) [54]. The IMFP provides information on the distance electrons can travel until the initial intensity I_0 decays to $\frac{I_0}{\mathrm{e}}$. The probability distribution of elastic scattering $P(L)$ decays exponentially, i.e. the longer the traveled distance is, the more electrons are inelastically scattered. This happens mainly due to one-electron-excitation or plasmon scattering [55]. This decay is shown in Fig. 2.6a. For example, the area beneath $P(L)$ from 0λ to 1λ amounts 63%. Therefore, 63% of the recorded electrons arise from an attenuation length of 0λ to 1λ [56]. Although higher attenuation lengths yield fewer elastically scattered electrons, the amount of electron from higher than 1λ is not negligible. This will be discussed in detail in section 2.2. From the probability distribution, it is clear that the recorded electron intensity $I(L)$ depends on the attenuation length L as well as on the IMFP λ according to [57]:

$$I(L) = I_0 \exp\left\{-\frac{L}{\lambda(E)}\right\} \tag{2.15}$$

$$\lambda(E) = \frac{E}{E_{\mathrm{plasmon}}^2[\beta \ln(\gamma E) - (C/E) + (D/E^2)]}. \tag{2.16}$$

As given in Eq. 2.16, the IMFP λ highly depends on the kinetic energy of electrons. A diagram of the kinetic energy dependence is shown in Fig. 2.6b. The experimental IMFPs for various materials and a theory curve are plotted. Eq. 2.15

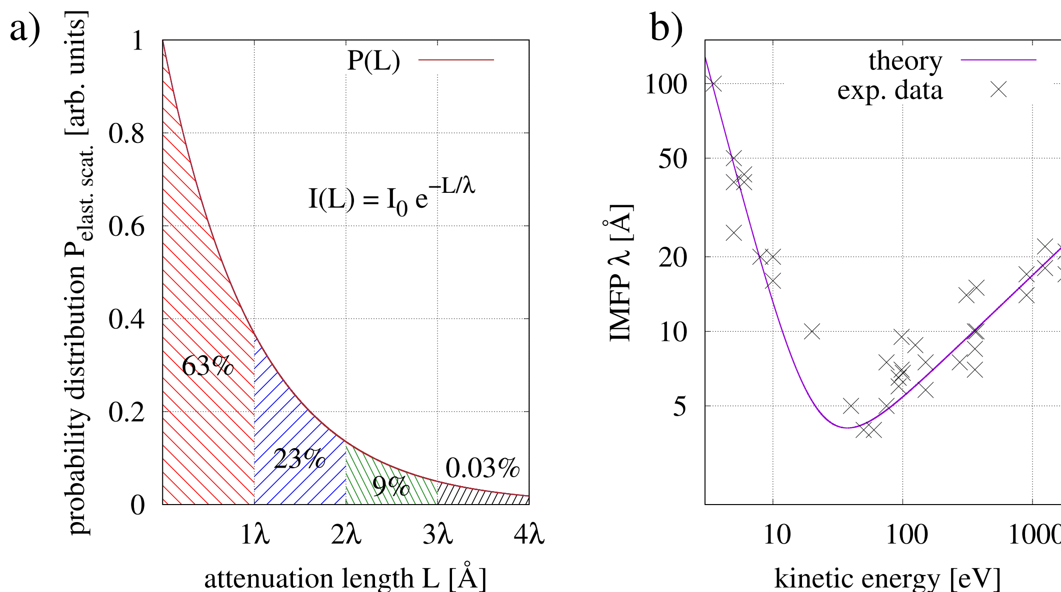

Figure 2.6: (a) The probability of elastic electron scattering P depending on the attenuation length l. The higher the distance traveled, the fewer elastically scattered electrons are recorded. (b) Inelastic mean free path (IMFP) of electrons λ depending on the kinetic energy. A minimum is reached for $E_{\text{kin}} \approx 50\,\text{eV}$. The IMFP λ considers 63% of elastically scattered electrons.

is universal and applies for all materials. However, measurements showed that there are slight differences in the IMFP for various material due to the number of valence electrons, the atomic weight, bandgap and density [56]. The free fit parameters β, γ, C and D adjust the theoretical curve to experimental data. For instance, as Na has less valence electrons than the C, the probability for electrons to inelastically scatter is much lower at a Na atom, i.e. the IMFP is higher. The theory curve can be used to roughly determine the IMFP. Depending on the kinetic energy and therefore on the resulting IMFP, a more surface sensitive or bulk sensitive measurement can be carried out. The highest surface sensitivity is achieved at an electron energy of $E_{\text{kin}} = 30\,\text{eV} - 60\,\text{eV}$. Lower and higher energies than this minimum cause a much higher IMFPs.

The second method to achieve a higher surface sensitivity is varying the polar angle θ which is defined as the angle between sample normal and the recording

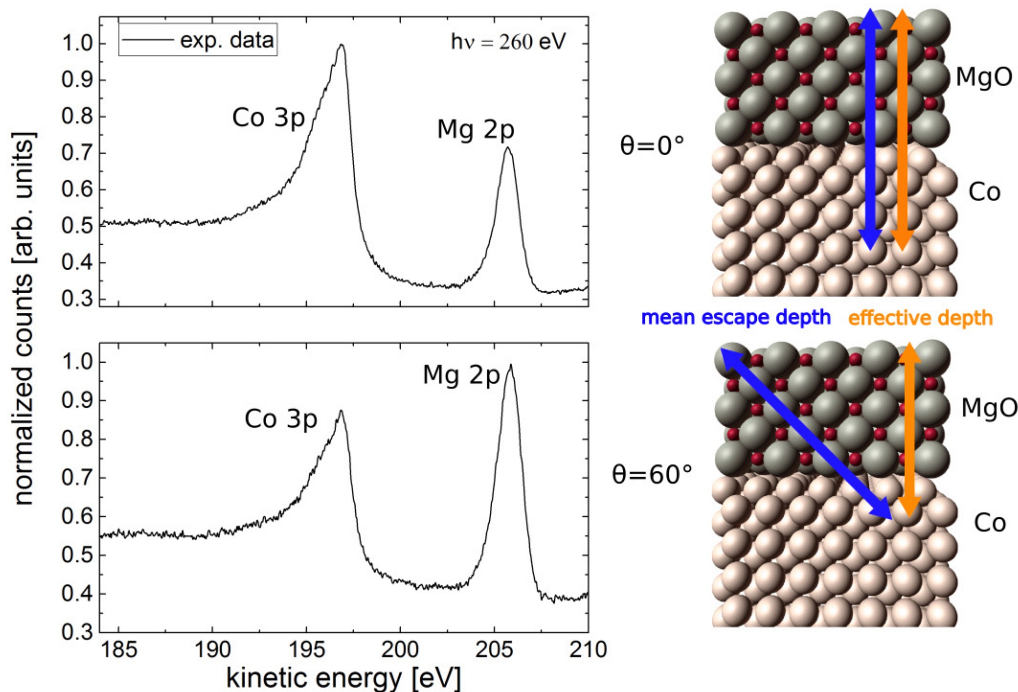

Figure 2.7: For an emission angle of $\theta = 0\,°$, the mean escape depth and the effective sample depth are the same. For an emission angle of $\theta = 60\,°$, the effective sample depth is reduced drastically although the mean escape depth is kept constant, since the electrons need to travel a significantly greater distance. As seen in the XPS spectrum for $60\,°$, the Mg 2p rises compared to Co 3p since MgO is laying on top of Co.

direction of the spectrometer [58]. The main concept is visualized in Fig. 2.7. In this example MgO lays on top of Co. The IMFP is constant for a specific electron energy. At an emission angle of $\theta = 0°$ relative to the sample normal, the Co 3p signal is maximized and the Mg 2p signal is minimized since the mean escape depth is identical to the effective sample depth. By varying the emission angle to $\theta = 60°$, the mean escape depth stays the same but is not parallel to the sample normal anymore. Consequently, the probing depth is shortened. Therefore, in the XPS signal the Co 3p intensity decreases and the Mg 2p signal increases. Thus, higher emission angles lead to a higher surface sensitivity. By this method, surface contaminations like oxidations or surface reconstructions

can be determined. Moreover, within an XPS spectrum surface bondings and bulk-type bondings can be distinguished.

2.2 X-Ray Photoelectron Diffraction (XPD)

X-ray photoelectron diffraction (XPD) is based on XPS and provides information on the atoms' local order in a solid state. Thereby, the elements' specific positions can be determined in a unit cell. The accuracy of this method is below 1 Å since the diffracted electrons show a strong decay within the solid and thus the long range order is neglected [59].

2.2.1 XPD Pattern

During the XPS process, spherical electron waves propagate from the emitters through the solid state and can be elastically scattered at the neighboring atoms. The schematic process is displayed in Fig. 2.8a. The resulting diffraction pattern arising from the XPS intensity modulation is shown in Fig. 2.8b. A photon

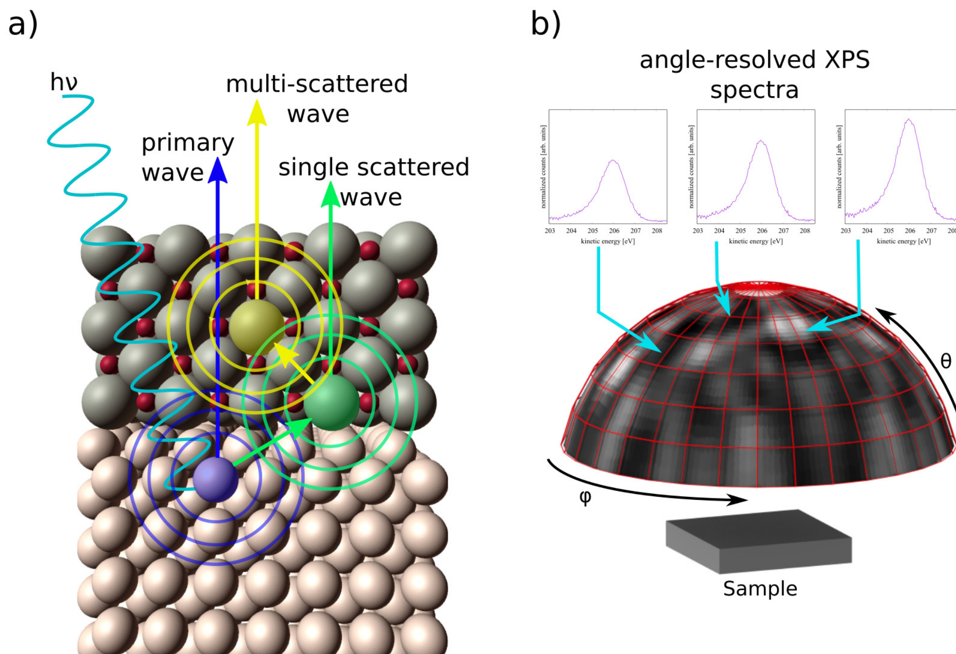

Figure 2.8: Schematic diagram of the electron wave diffraction process within a solid state (a). Illustration of the resulting diffraction pattern due to intensity modulation recorded in the hemisphere (b).

causes the emitter to produce an electron wave that is elastically scattered at a neighboring atom. In turn, the scattered wave can be scattered again becoming a (multi-)scattered wave. This happens for all emitters simultaneously in the solid state. Due to the locked phase and amplitude ratio of the primary and scattered waves, an interference pattern emerges in the hemisphere above the sample.

The initial electron wave amplitude ψ_{initial} decays from the emitting atom according to [60]:

$$\psi_{\text{initial}}(\vec{r}) \propto \frac{e^{ik|\vec{r}|}}{|\vec{r}|}. \tag{2.17}$$

Due to the strong decay, electron waves are mainly scattered at neighboring atoms and therefore the long range order is neglected [61]. Moreover, as the waves are scattered at the atom's potential of the specific element, XPD also becomes chemically sensitive in addition to its structural sensitivity. The single scattering case is described in detail. The scatter wave $\psi_i(\vec{r})$ can be derived from the primary wave ψ_{initial} according to:

$$\psi_i(\vec{r}) = \psi_{\text{initial}}(\vec{r}) \times f_j(\vec{k}) \times \frac{e^{ik|\vec{r}_j - \vec{r}|}}{|\vec{r}_j - \vec{r}|}. \tag{2.18}$$

Depending on the distance of the scatter atom to the emitter atom $|\vec{r}_j - \vec{r}|$ the initial wave amplitude $\psi_{\text{initial}}(\vec{r})$ decays exponentially according to Eq. 2.17. By considering the scattering factor amplitude $f_j(\vec{k})$ (SFA), a phase shift is applied to the scattered wave $e^{ik|\vec{r}_j - \vec{r}|}$. Since the SFA is element specific, the recorded intensity I depends strongly not only on the kinetic energies of the photoelectrons but also on the scatter atoms itself and its distance to the emitter atom [62]. Further, since direction and amplitude of $\vec{k}$ are not isotropic, the SFA also depends on the angle between the emitter and scatter atom. Exemplary, the SFA of Si, Ni, and O is discussed for different kinetic energies and different angles.

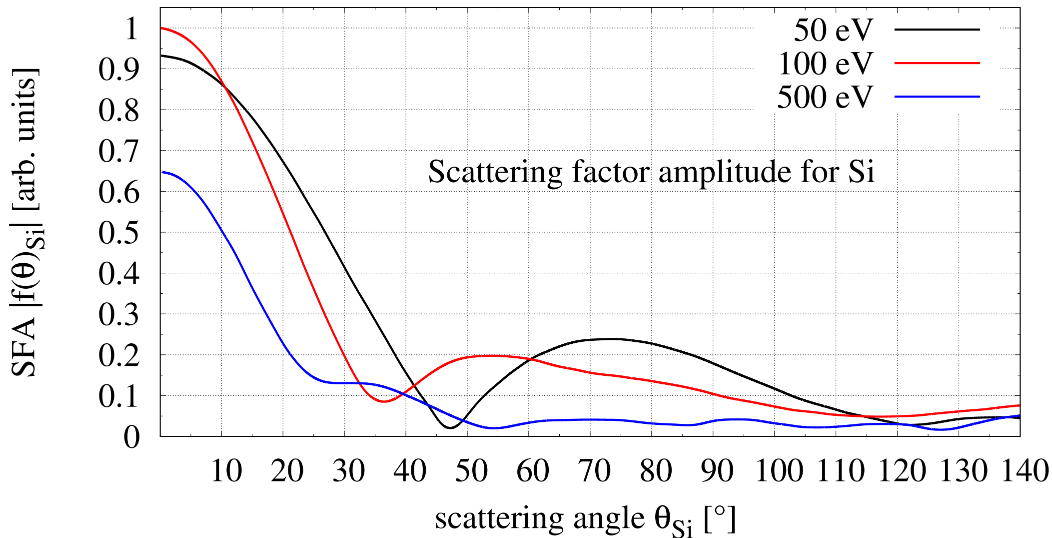

Figure 2.9: SFA for Si depending on the scattering angle Θ_{Si} for different kinetic energies. Taken from [60].

Next to the Debye-Waller factor, the dipole-matrix elements, and the polarization of the incoming photons, the SFA defines the form of the scattered electron waves and therefore the recorded XPD pattern [60]. More to the mathematical background is found in literature [34, 60, 62, 63]. The SFA is displayed for different kinetic energies as a function of the scatter angle in Fig. 2.9. For high kinetic energies $E_{\mathrm{kin}} \gg 500\,\mathrm{eV}$, the maximum of the SFA is at $\Theta_{\mathrm{Si}} = 0$. All side characteristics are negligible as their amplitude is rather low. This behavior is called *forward scattering* since neighboring atoms, that are not in a straight line between the scatter atoms, are missed out. In a solid state these straight lines between single atoms form long atom chains due to the periodicity of the sample [64]. Considering the high IMFP due to the elevated energy, the forward scattering process reveals mainly the overall crystal orientation and its structure. Since surface reconstructions or relaxations happen in the top most layers, they do not contribute significantly to the emerging XPD pattern. Further, the SFAs of different elements for high kinetic energies become indistinguishable. This is clearly seen for Ni and O in Fig. 2.10. While for a kinetic energy of $E_{\mathrm{kin}} = 60\,\mathrm{eV}$ a huge difference appears especially in the back-scattering regime, and they appear

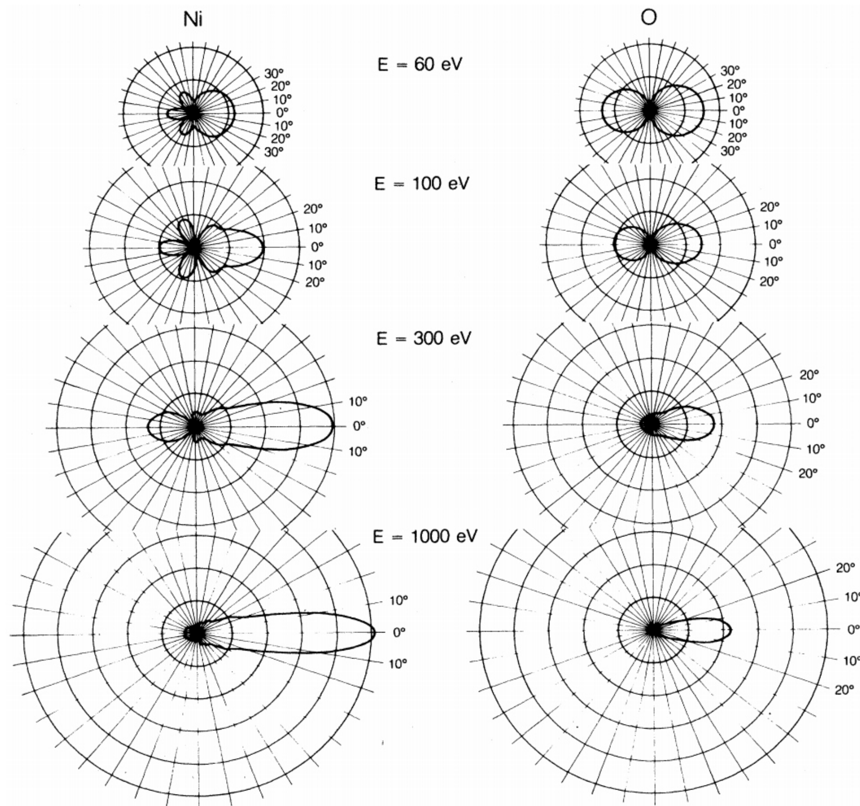

Figure 2.10: Polar plot of the SFA for Ni and O depending on the kinetic energy. Taken from [65].

to be very similar for $E_{\text{kin}} = 1000\,\text{eV}$. Therefore, the forward scattering regime does not only neglect surface reconstructions. The chemical information is only provided by the forward scattering amplitude. In this work, these patterns are abbreviated by FSXPD (*forward scattering x-ray photoelectron diffraction*)[1] patterns. For lower kinetic energies $E_{\text{kin}} \ll 500\,\text{eV}$, strong side characteristics arise at higher Θ angles. Therefore, atoms that are not in a straight line between two scatter atoms contribute the XPD pattern as well. Since the IMFP for these energies is rather low, non-bulk type formations like surface structures and small displacements in the unit cells are revealed. In this regime forward-scatter and back-scatter effects contribute significantly to the emerging XPD pattern. These full scattering XPD patterns are just called XPD patterns in this work.

[1]Note that this abbreviation is not common in literature. In this work, this abbreviation is necessary for a better distinction of the XPD patterns.

The limit for FSXPD and XPD is not fixed at 500 eV since each element has a distinguishable dipole-matrix element and cross-section. Both mentioned behaviors can also be combined. For instance, instead of analyzing either surface reconstructions or bulk structures, buried interface structures between two layers can be recorded as well. Depending on the thickness of the deposited film, that is usually in a range of 1 nm-2 nm, kinetic energies of 200 eV-550 eV are common [59, 63, 66].

2.2.2 XPD Analysis

As the waves are spherical, the interference effects are observed for each (θ_i, ϕ_j) combination in a step widths of $\Delta\theta = 2\,°$ and $\Delta\phi = 1.8\,°$ in the hemisphere above the sample. This is achieved by rotating the sample with respect to the spectrometer. The recorded intensity $I(\vec{k})$ is defined as:

$$I(\vec{k}) = \left| \psi_{\text{initial}}(\vec{k}) + \sum_i \psi_i(\vec{k}) \right|^2 . \tag{2.19}$$

By absolute squaring the sum of the initial electron wave ψ_{initial} and all scattered waves ψ_{i} the electron wave's phase information is lost. Therefore, a direct conclusion on the sample structure from the XPD pattern can not be drawn. Thus, an expected structure needs to be calculated resulting in a simulated XPD pattern that is then compared to the experimental XPD pattern. For this comparison the experimental data need to be prepared. An overview of each preparation step is provided in Fig. 2.11. Since each XPD data point consists of a complete XPS spectrum, the background for each spectrum needs to be subtracted according to the procedure described in section 2.1.3. The angle-depended XPS intensities are normalized resulting in the anisotropy function $\chi\,(\theta, \phi)$ defined as:

$$\chi\,(\theta, \phi) = \frac{I\,(\theta, \phi)}{\overline{I\,(\theta)}} - 1. \tag{2.20}$$

With this function, each XPS spectrum $I\,(\theta, \phi)$ is scaled by the mean intensity $\overline{I\,(\theta)}$ of its specific azimuth angle ϕ. This is crucial since depending on the photon intensity the absolute count rate may vary at each polar angle. With the anisotropy function the deviation of the mean intensity of the polar angle is provided. Then, statistical errors are reduced by symmetrizing the manipulated pattern and applying a weak Gaussian blur.

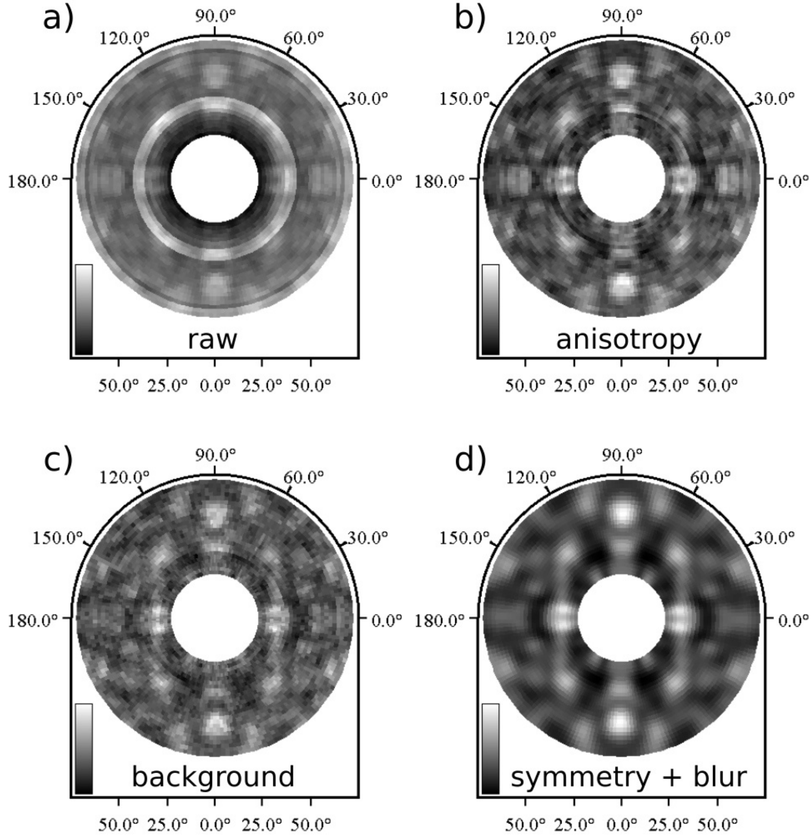

Figure 2.11: An anisotropy function is obtained from the experimental raw XPD pattern (a) so that the diffraction maxima und minima are clearly distinguishable (b). Then, the background is subtracted (c). Mostly, a symmetry function and a weak Gaussian blur is applied (d) to improve statistics.

After preparing the experimental data, an XPD pattern can be calculated and compared to the experimental one. The Reliability-factor (R-factor) provides quantitative information on this comparison [67, 68]. The R-factor is defined as:

$$R = \frac{\sum_i [\chi_{\text{exp}_i} - \chi_{\text{sim}_i}]^2}{\sum_i \left[\chi^2_{\text{exp}_i} + \chi^2_{\text{sim}_i}\right]}. \tag{2.21}$$

With this definition, the R-factor is in range of 0 to 2, whereas 0 indicates a perfect match, i.e. the XPD patterns are identical. For a R-factor of 2, the simulated and the experimental patterns are totally anti-correlated.

The simulated XPD patterns are calculated with the *Electron Diffraction in Atomic Clusters for Core Level Photoelectron Diffraction Simulations* (EDAC) tool [69]. In order to do so, an expected or assumed crystal structure consisting of several thousands different atoms with distinct location and orientation is generated. Then, by calculating the IMFP from the photoelectrons' kinetic energy used in the experiment, the scatter radius and electron emitters within the generated atom cluster are selected. With this information and the EDAC tool, a simulated pattern is calculated. The EDAC tool includes the multiple scatter effects [70]. Therefore, within the simulation, electrons are generated at the selected emitters and electron waves propagate through the crystal whereas all scatter paths up to a scattering order of $n = 20$ are taken into account. The strength of EDAC is that it does not make any approximations beyond the muffin-tin potential of the atom and, in particular, an exact representation of the free-electron Green function is considered. Gracía de Abajo *et al.* provide more details on the mathematical background [69].

To evaluate the best crystal structure that corresponds to the lowest R-factor, a genetic algorithm is used. For this process, not only an atom cluster but also boundaries for the lattice site variation are generated. The variations include translation, rotation, and scaling of either a set of atoms or of individual atoms. Within these variation boundaries, modified structures next to the original starting structure are generated. The genetic algorithm is crucial for determining the best correspondence between experimental and simulated data since it effectively avoids R-factor minima [68, 71]. The process is illustrated in Fig. 2.12.

There are two types of structure sets within this procedure: the set of current structures s_{cur} and the set of best structures s_{best} whereas each consists of 60 structures. The genetic algorithm starts by applying a random variation to the starting structure producing 60 structures s_0. It fills the current set s_{cur} with these starting structures. For all structures of s_{cur} corresponding simulated

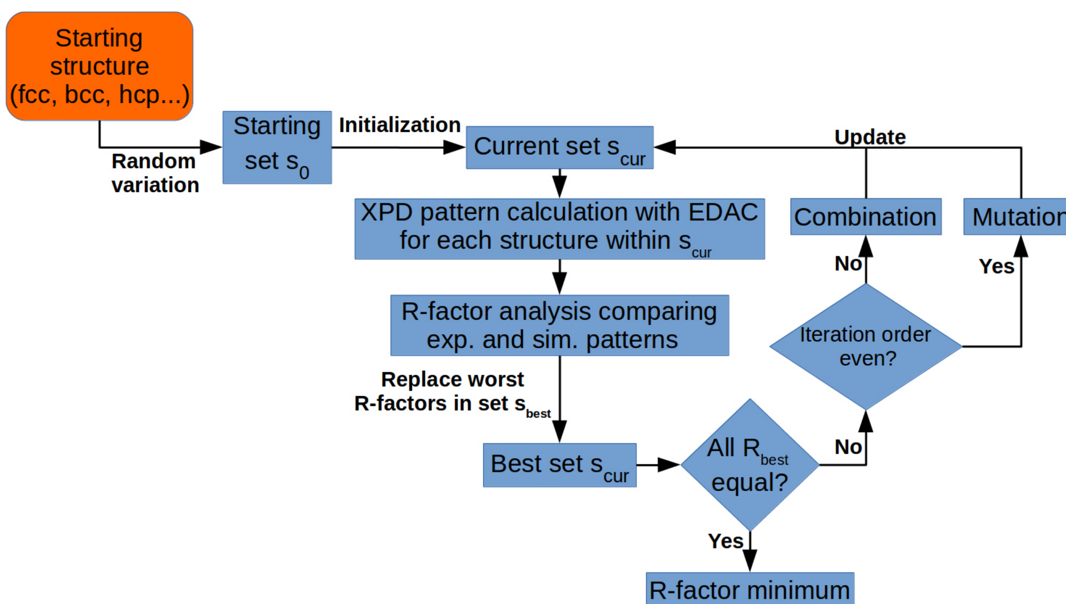

Figure 2.12: Flow chart of the R-factor minimization procedure of the genetic algorithm. Commencing with a starting structure, atom displacements are applied and the corresponding XPD patterns are compared to the experimental XPD pattern via the R-factor. A combination or mutation to the structures corresponding to the best R-factors is applied after each iteration. Thereby, a new set of new structures is generated. Once a R-factor minimum is found, the iteration stops.

patterns are calculated and then compared to the experimental data within the R-factor analysis. Then, all newly obtained R-factors are compared to the R-factors corresponding to the set s_{best} and eventually s_{best} is updated if better R-factors are obtained. If all R-factors within s_{best} are equal, the iteration stops since a global minimum is found. Otherwise, depending on the iteration order i new structures are produced by combining or mutating the s_{best} structures. These new structures are then updated into the current set s_{cur} and the procedure is repeated. More details to this process is provided in literature [71–73].

3 Experimental Aspects

All experiments were performed *in situ* in an ultra-high vacuum chamber at beamline 11 at the synchrotron radiation facility DELTA, TU Dortmund, Germany. The chamber is equipped with a *Low Energy Electron Diffraction* apparatus, a sputtergun, an electron spectrometer, and an electron beam evaporator.

3.1 UHV-chamber

In the ultra-high vacuum (UHV) chamber the base pressure is $p \approx 5 \times 10^{-11}$mbar. At this pressure it takes up to 10 h to cover 1 % of the surface with residuals [74]. For time-consuming experiments like XPD this pressure is crucial in order to sustain clean surface conditions. The UHV chamber is schematically shown in Fig. 3.1. The chamber consists of a sample transfer stage and a main chamber in which all experiments are performed. The sample transfer stage's base pressure $p_{\text{transfer}} \approx 10^{-9}$mbar is achieved within a few hours with a scroll pump and a turbo-molecular pump. This pressure is sufficient to a sample transfer into the main chamber without breaking UHV conditions. After the sample is transferred, the preparation procedures can be carried out. The manipulator is capable to move the sample in all three spatial directions as well as rotating the sample in azimuthal and polar direction. In the experimental used, XPS and XPD measurements are performed by an electron spectrometer with nine channeltrons. The spectrometer's energy step width was set to 0.045 eV. The electrons are focused within the spectrometer towards the hemispherical analyzer. The hemispherical analyzer's inner plate is on a positive potential and its outer sphere on a negative potential, i.e. it works like a capacitor with a deflec-

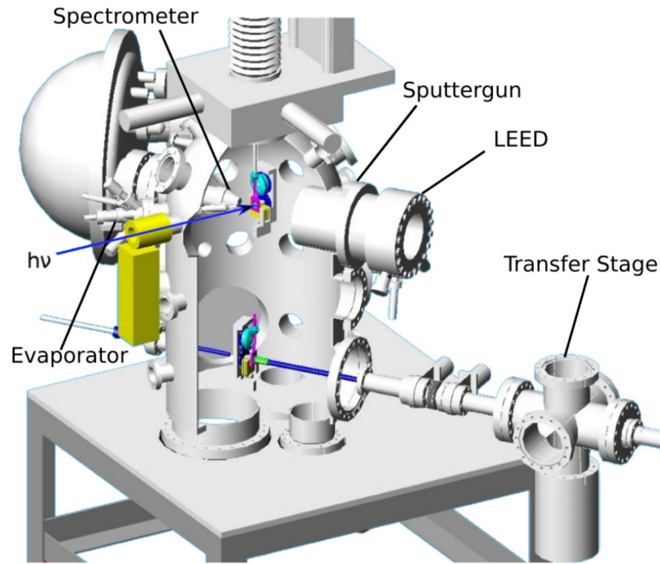

Figure 3.1: Main UHV chamber used to prepare the samples and perform all the experiments. The base pressure is $p \approx 5 \times 10^{-11}$mbar. Via a transfer stage the samples are transferred into the main chamber wherein a LEED system, a spectrometer, evaporator, and a spectrometer are installed.

tion voltage V. Only electrons with the passenergy E_{PE} travel exactly on a path with a radius R_0 since this path is on a equipotential line as seen in Fig. 3.2. Electrons with higher energies are deflected towards the outer sphere and electrons with lower energies towards the inner sphere, respectively. Therefore, an energy resolution is transferred into a spatial resolution. At the end of their path they are recorded via nine channeltrons. By varying the deflection voltage within the hemisphere the electrons with the desired kinetic energies can be recorded. The recorded signal is processed by computer where each channeltron is assigned to a kinetic energy with its number of counts.

3.2 Sample Holder

The sample holder for rotating and heating the sample is shown in Fig. 3.3. The cylindrical sample holder consists of a base frame, base plate, and three bronze

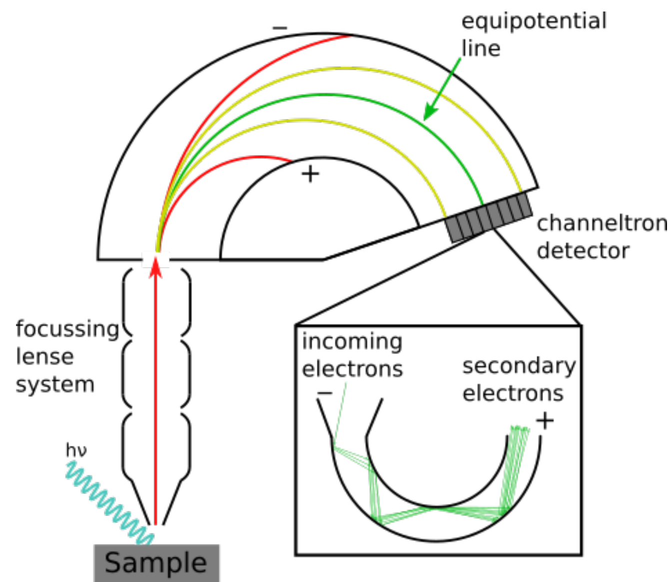

Figure 3.2: Schematic diagram of the spectrometer used to detect the electrons emitted from the sample depending on their energy. Nine channeltrons detectors are placed at the end of spectrometer to multiply the incoming electrons.

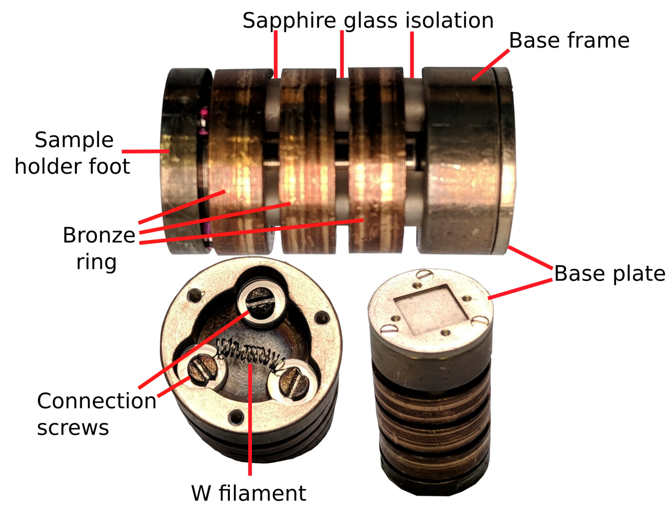

Figure 3.3: The sample holder used to prepare the samples in the UHV. Three bronze rings are isolated via sapphire isolations. Beneath the base plate two of the rings are connected to W filament. By applying a current to these two bronze rings the sample can be heated.

sliding rings that are separated by sapphire brackets to isolate them. All bronze contacts are connected to screws that lead to the base frame and provide three isolated contact options. Two of these screws are connected via a W filament with a thickness of $t = 0.15\,\mathrm{mm}$ and 15 turns. The filament is located beneath a sample plate wherein the sample is fixed by a steel ring. Below the sample holder foot a screw thread is located to fix the sample holder onto the manipulator of the UHV main chamber. At the manipulator three bronze pins are connected to the sample holder's sliding rings so that a current can flow through the filament. With a power of $P \approx 23\,\mathrm{W}$ a sample temperature of $550\,^\circ\mathrm{C}$ is achieved. The temperature is determined with a pyrometer.

3.3 Sputtergun

To remove adsorbate atoms and residuals from the sample surface, Argon ions Ar^+ are used to bombard the sample. Therefore, Ar is let into the chamber to a pressure of $p_{\mathrm{Ar}} = 2.5 \times 10^{-7}\mathrm{mbar}$. By applying a current to the filament in the sputtergun, electrons are generated due to the Edison effect, i.e. thermal electron emission [75], and then accelerated because of a high voltage between the filament and the anode. The accelerated electrons ionize the Ar atoms. With a second high voltage between the anode and the extractor the Ar^+ atoms are accelerated and then focused towards the sample by electro-optical lenses. The kinetic energies are typically in range of $E_{\mathrm{kin}}^{\mathrm{Ar}} = 500\,\mathrm{eV} - 1500\,\mathrm{eV}$. The ions hit the sample surface at an angle of $60\,^\circ$ with respect to the surface normal. At this angle, mainly surface layers are removed. Additionally, the grounded sample is constantly rotated at a speed of $1.8\,\frac{^\circ}{5\,\mathrm{s}}$ in azimuth angle ϕ. The damaged sample needs to be annealed after sputtering. These sputter-annealing cycles are repeated to prepare the sample surface.

In this work, GaAs was sputtered and annealed several times. For GaAs it is crucial to focus the Ar^+ beam on the sample only and to avoid sputtering at the fixing steel ring around the sample. Like most III-V semiconductors GaAs is very vulnerable to C contamination and therefore sputtering the steel ring at an

angle of 60° produces C contaminations on the surface. Thus, the sputter size needs to be adjusted to the sample surface.

3.4 Low Energy Electron Diffraction

Low Energy Electron Diffraction (LEED) is a method to analyze periodicities on the sample surface like surface reconstructions. Coherent electrons are focused towards the sample and the diffracted electrons are observed at a fluorescent screen. The LEED apparatus is shown schematically in Fig. 3.4. Electrons are

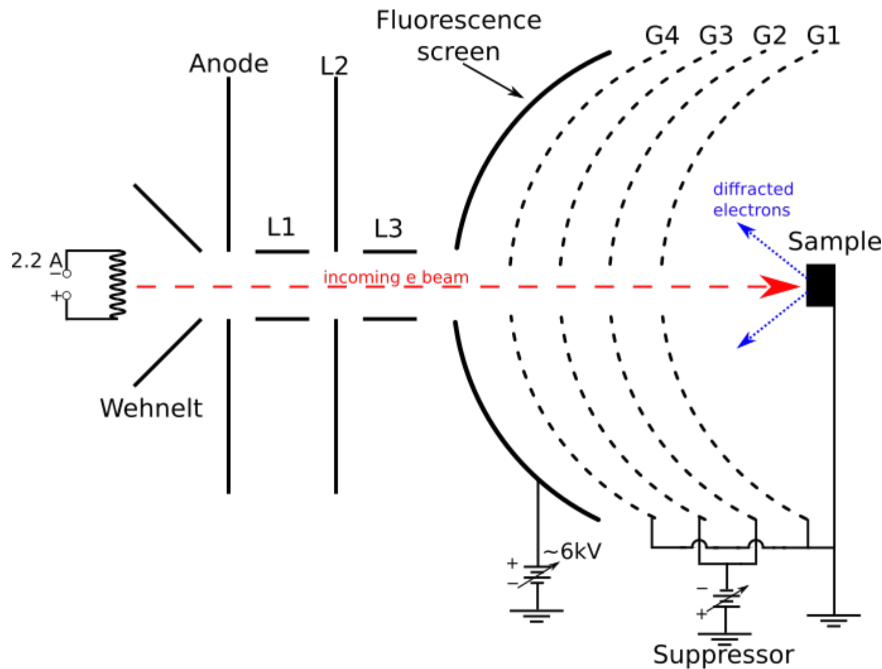

Figure 3.4: Schematic diagram of the LEED system. An electron beam is focused via electro-optical lenses on the sample. The diffracted electrons are separated from inelastically scattered ones by the supressor. The diffraction pattern is imaged at the fluorescence screen.

emitted from a filament and focused towards the sample by the wehnelt cylinder and the focusing lenses L1-L3. Due to the wave-particle duality, the incoming electrons can be described by a wave vector $\vec{k}_0$. At the sample surface, they can either be elastically scattered, i.e. $\left|\vec{k}_{\text{elast.}}\right| = \left|\vec{k}_0\right|$, or inelastically scattered

$\left|\vec{k}_{\text{inelast.}}\right| \neq \left|\vec{k}_0\right|$. More information on this process and the Laue equation is provided in literature [76–78]. The scattered electrons pass a four grid system. The first grid is grounded so that the electrons are not deflected on their way from the sample to the grid system and therefore the interference pattern is not distorted. The second grid is on a negative potential $-V_0$ that correlates with the incoming electron energy. It is set slightly lower than the accelerating potential within the electron gun. Since inelastic scattered electrons lost a portion of their energy, only elastic scattered electrons with $\left|\vec{k}_{\text{elast.}}\right| = \left|\vec{k}_0\right|$ pass the second grid. The third grid is set on the same potential like the second grid and can additionally be changed by the operator, i.e. $-(V_0 + \Delta V_{\text{var}})$. The fourth grid is grounded and the fluorescence screen voltage is set to 6 kV. The accelerated electrons produce fluorescence radiation on the screen. Depending on the amount of electrons on a distinct point on the screen, more light is emitted. The fact that only elastically scattered electrons reach the screen and due the Laue condition a sharp LEED pattern appears on the screen. If no reflexes are visible, the surface is not well-ordered or reconstructed.

3.5 Electron Beam Evaporator

An electron beam evaporator is used to evaporate single atomic layers . Again electrons are emitted from a filament and accelerated by a high voltage of $U_{\text{HV}} = 600 - 700\,\text{V}$ towards the material. Thereby, temperatures of $T \gg 1000\,°\text{C}$ are achieved and the material is sublimed. For Co evaporation a Co rod with a purity of 99.99+% is used. MgO granulate with a purity of 99.95+% is placed into a W crucible. It is necessary to use a W crucible since it conducts the heat to MgO. W is necessary here as it has a much higher sublimation temperature than MgO and no W is evaporated during this process. The electron beam evaporator is shown in Fig. 3.5. The filament and the crucible (or rod in case of Co) are located within a copper cylinder that is water cooled. Therefore, the UHV chamber is not heated. A shutter at the front of the evaporator is used to determine the exact evaporation time.

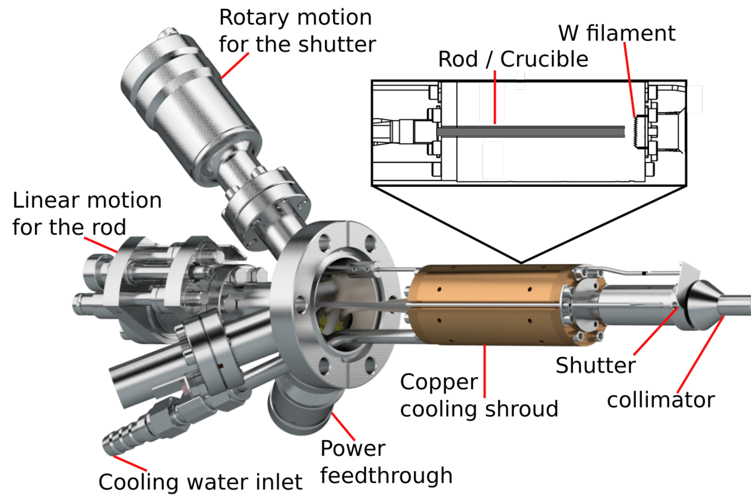

Figure 3.5: Electron beam evaporator used to deposit Co or MgO. For Co deposition, a Co rod is used. For MgO deposition, a crucible is used wherein a MgO chunk is placed. Taken from [79].

3.6 Synchrotron Light Source DELTA

Within this work all incoming photons for the experiments originated from the undulator U-55 at beamline 11 at DELTA in Germany. The storage ring is sketched in Fig. 3.6. The electrons are linearly accelerated and then preaccelerated in the BoDo. At position T_2 they can be injected into the Delta storage ring. The synchrotron's circumference is 115 m. Electrons with a kinetic energy up to 1.5 GeV and an electron beam current of 130 mA can be stored. The undulator U-55 located within the storage ring consists of 47.5 alternating permanent magnets. The magnets force the electron packages in the U-55 to perform a curved path. Due to the change in the electrons' velocity, bremsstrahlung is emitted in an energy range of $h\nu = 50\,\text{eV} - 1500\,\text{eV}$ towards beamline 11. In the beamline, a plane grating monochromator (PGM) selects a distinct energy producing monochromatic light with an energy resolution up to $\frac{E}{\Delta E} = 28.000$ [81]. After several focusing elements within the beamline a spot

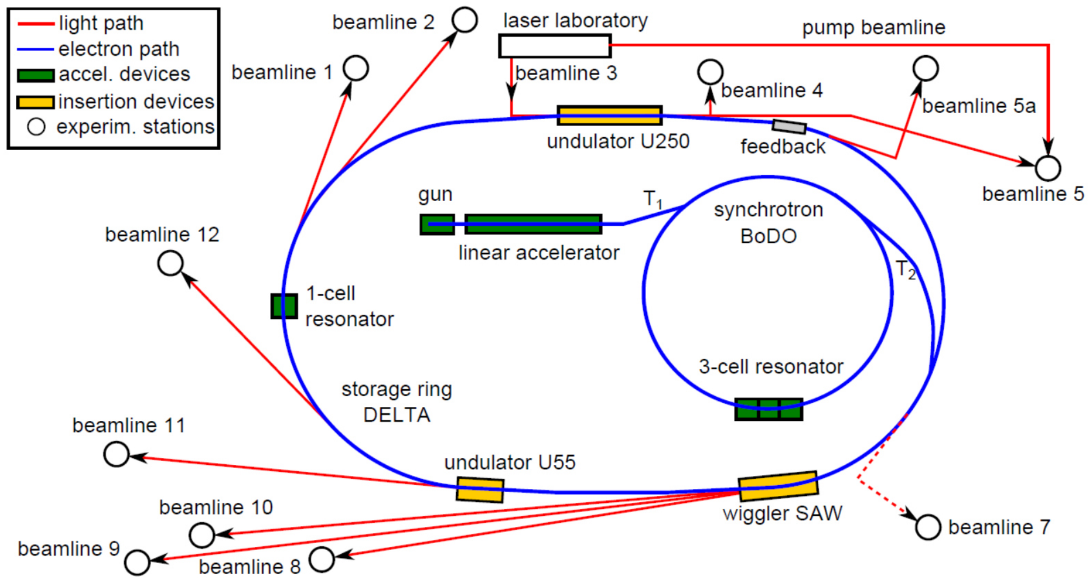

Figure 3.6: Schematic diagram of DELTA with all beamlines, the linear accelerator, and the synchrotron BoDo. The experiments within this work have been performed at soft x-ray beamline 11. Taken from [80].

size of $70 \times 30\,\mu\text{m}^2$ (hor.×vert.) results at the end of the beamline, i.e. in the UHV chamber. The sample is positioned at this focus point.

4 Multi-Layer System Characteristics & Preparation

4.1 GaAs

GaAs is a III-V semiconductor in zinc blende structure. Both elements Ga and As are in a face-centered cubic (fcc) structure and shifted by $\frac{1}{4}\mathrm{a}_{\mathrm{GaAs}}$ in space diagonal. The resulting lattice constant is $a_{\mathrm{GaAs}} = 5.65\,\text{Å}$. These covalent bonded elements have different sublimation temperatures in zinc blende structure. The sublimation of As starts at $T_{\mathrm{As}} \approx 350\,°\mathrm{C}$ at a pressure of $p \approx 10^{-10}$ mbar whereas the sublimation point of Ga is much higher $T_{\mathrm{Ga}} > 600\,°\mathrm{C}$. Therefore, by controlling the annealing temperature within the sputter-annealing cycles, Ga-terminated surfaces with various Ga:As ratios can be achieved. With the samples used here no As-terminated surfaces can be produced since the sample's Ga:As ratio is 1:1. By annealing the sample, only As can be removed from the sample, i.e. annealing leads to Ga-rich surfaces. In order to achieve As-rich surfaces the sample needs to be manufactured with an As capping layer with a thickness of several nanometers. Then, by choosing the annealing temperature and the annealing time different As-rich surfaces can be produced [82]. It is important to use a GaAs in a (001) orientation as a substrate instead of other orientations since a dead layer is formed between Co and GaAs otherwise [83–85]. This dead layer is non-magnetic and therefore reduces the TMR ratio significantly. No similar behavior has been reported for Ga-rich surface GaAs(001) reconstructions.

The resulting surface reconstructions for GaAs(001) in Wood notation starting from As-rich to Ga-rich ones are:

$$\text{As-rich}\begin{cases}\text{c}(4\times 4)\\ \text{c}(2\times 8)\end{cases}$$
$$\text{p}(1\times 6)\quad \text{p}(2\times 6)\quad \text{p}(3\times 6)\quad \text{p}(6\times 6)$$
$$\text{Ga-rich}\begin{cases}\text{c}(8\times 2)\\ \text{p}(4\times 6)\end{cases}.$$

The transition from As-rich to Ga-rich surface reconstructions leads to a formation of different domains called $(n\times 6)$ since the Ga:As ratio is not equal throughout the surface. Therefore, these reconstructions are not suitable for interface analysis as a variety of interface compound formations might occur. Moreover, it is well known that As diffuses into the evaporated layer [86]. The As diffusion needs to be reduced to a minimum to realize thin film based GaAs-applications. Thus, the Ga-rich c(8×2) surface is chosen since it effectively reduces As diffusion into evaporated materials [73, 87]. Further, it is the most stable one from all surface reconstructions next to the As-rich c(2×8) reconstruction, i.e. it can be prepared at a wide annealing temperature range $T = 500\,°\text{C} - 560\,°\text{C}$ [88]. The sputter and annealing parameters for the c(8×2) preparation are listed in Tab. 4.1.

Table 4.1: Parameters for the sputter-annealing cycles used to prepare the GaAs c(8×2) surface reconstruction. The variable r represents the cooling rate.

	Value	Evaporation time	
Degasing	$T_{\text{Degas}} = 500\,°\text{C}$, $r \approx 5\ °\text{C/min}$	60 min	
Sputtering	$E_{\text{sputter}} = 1000\,\text{eV}$	10 min	Repeated
Annealing	$T_{\text{anneal}} = 540\,°\text{C}$, $r \approx 10\ °\text{C/min}$	25 min	Repeated

It is crucial to degas the sample holder and the sample before actually proceeding to the sputter-annealing cycles. Like nearly all III-V compounds GaAs has a

high C affinity. It is crucial to ensure a pressure of $p < 1 \times 10^{-9}$mbar during the sputter-annealing cycles. The preparation starts with a degassing process. The temperature of $T_{\text{Degas}} = 500\,°\text{C}$ is kept for $t \approx 60\,\text{min}$ and cooled very slowly. Then, the actual surface preparation is carried out by several sputter-annealing cycles as mentioned above. Typically two to four cycles are enough to obtain a clean surface and a well ordered c(8×2) surface reconstruction. The clean surface is checked with XPS as shown in Fig. 4.1.

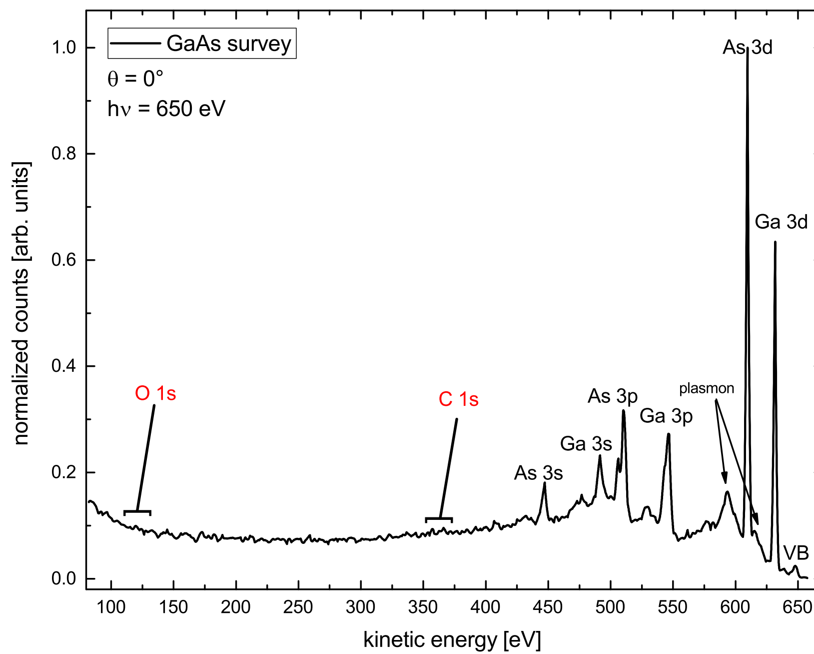

Figure 4.1: GaAs XPS survey spectrum at an incoming photon energy of hν = 650 eV and $\theta = 0°$. After several sputter-annealing cycles no indication of O and C contaminations are observed. All observable peaks corresponding to the GaAs orbitals are labeled as well.

An incoming photon energy of 650 eV, i.e. kinetic energies below 650 eV, results in a very surface sensitive measurement. In the survey spectrum recorded at an incoming photon energy of 650 eV no C or O contaminations are observed. Consequently, a LEED measurement is performed as shown in Fig. 4.2. The GaAs bulk unit cell is highlighted in red. Since the zinc blende structure is

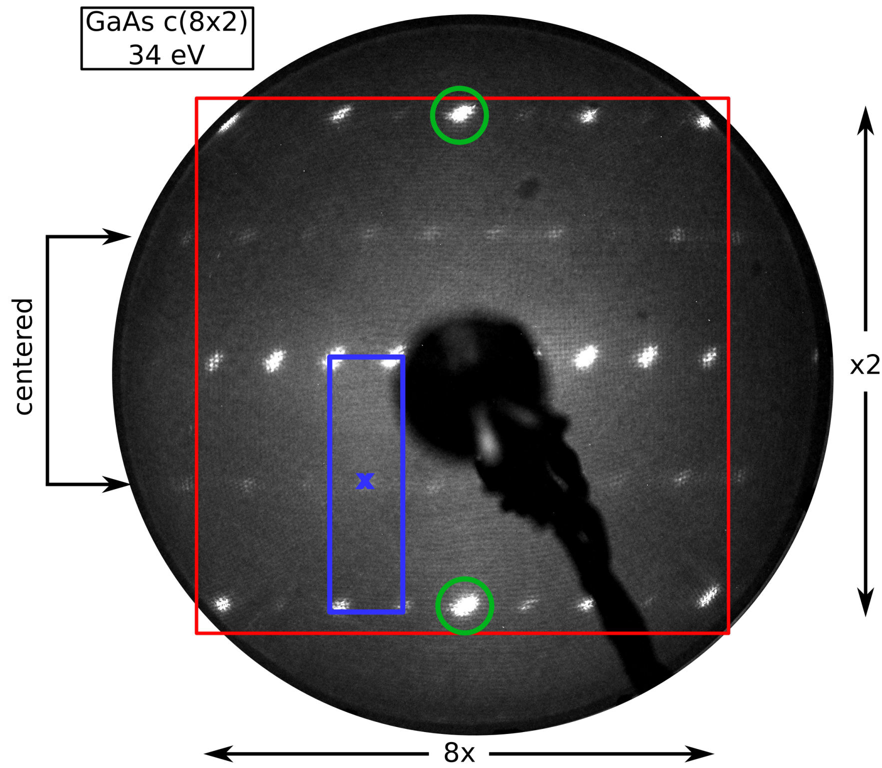

Figure 4.2: LEED pattern of the c(8×2) surface reconstruction of GaAs(001) recorded at an electron energy of $E_{\mathrm{kin}} = 34\,\mathrm{eV}$. The red square shows the cubic substrate unit cell. The blue rectangle indicates the actual centered surface reconstruction. It is found within the GaAs substrate unit cell in a (8x2) periodicity [89]. The green circles indicate a (4×2) periodicity due to the Ga sub-dimers.

cubic, the observed bulk unit cell is a square in the LEED pattern. The arising c(8×2) surface reconstruction is larger than a single unit cell, i.e. a smaller rectangle indicated in blue arises in the LEED pattern. The green circles indicate a smaller (4×2) periodicity. From literature, IV-LEED measurements showed that it might correspond to Ga sub-dimers [90, 91]. After the successful preparation of a c(8×2) GaAs surface reconstruction, Co is deposited.

4.2 Co/GaAs

Co is a transition metal and crystallizes naturally in a hexagonal close-packed (hcp) structure. Since the hcp structure is three-folded and the zinc blende structure is two-folded, growing thin Co(hcp) layers on GaAs is impossible. The zinc blende structure induces a body-centered cubic (bcc) structure onto Co within the Co film. The Co(bcc) structure is meta-stable since it makes a transition to Co(hcp) for a film thickness of $d_{\mathrm{Co}} > 50\,\mathrm{nm}$ [23, 92]. The lattice constant of Co(bcc) is compressed to $a_{\mathrm{Co,bcc}} = 0.5 \times a_{\mathrm{GaAs}} = 2.827\,\text{Å}$ to match GaAs' lattice constant. From XPS and RHEED measurements it is well known that Co(bcc) dissolves at a substrate temperature of $T_{\mathrm{GaAs}} > 300\,°\mathrm{C}$ and forms strong bondings to Ga and As [93]. Since the electronic structure of a (001)-bcc metal is necessary to obtain high TMR values, Co is evaporated on the GaAs(001) reconstruction at room-temperature (RT). In order to obtain a homogeneous sample Co is deposited at an angle of $\theta \approx 45\,°$ while constantly rotating the sample. The evaporation parameters for the evaporator are listed in Tab. 4.2.

Table 4.2: Evaporation parameters to deposit a Co layer thickness of $d_{\mathrm{Co}} = 12\,\mathrm{ML}$ onto GaAs in the UHV chamber.

Parameter	Value
Filament Current	$I_{\mathrm{Fil}} = 3.02\,\mathrm{A}$
High Voltage	$U_{\mathrm{High}} = 1000\,\mathrm{V}$
Emission Current	$I_{\mathrm{Em}} = 14.9\,\mathrm{mA}$
Resulting Power	$P = U_{\mathrm{High}} \times I_{\mathrm{Fil}} = 14.9\,\mathrm{W}$
Evaporation Time	$t = 6\,\mathrm{min}$
Resulting Thickness	$d_{\mathrm{Co}} = 12\,\mathrm{ML}$

As described in chapter 1, a thickness of $d_{\mathrm{Co}} = 12\,\mathrm{ML}$ [1] is chosen to analyze the lower boundaries of possible MTJs and thin film effects. From literature it is known that possible interface interaction are formed below a thickness of $d_{\mathrm{Co}} < 6\,\mathrm{ML}$ [94]. Therefore, a thickness of $d_{\mathrm{Co}} = 12\,\mathrm{ML}$ is ideal to probe the interface interactions of Co/GaAs as well as the first layers of pure Co(bcc).

[1] 1 monolayer (ML) of Cobalt corresponds to 0.14 nm

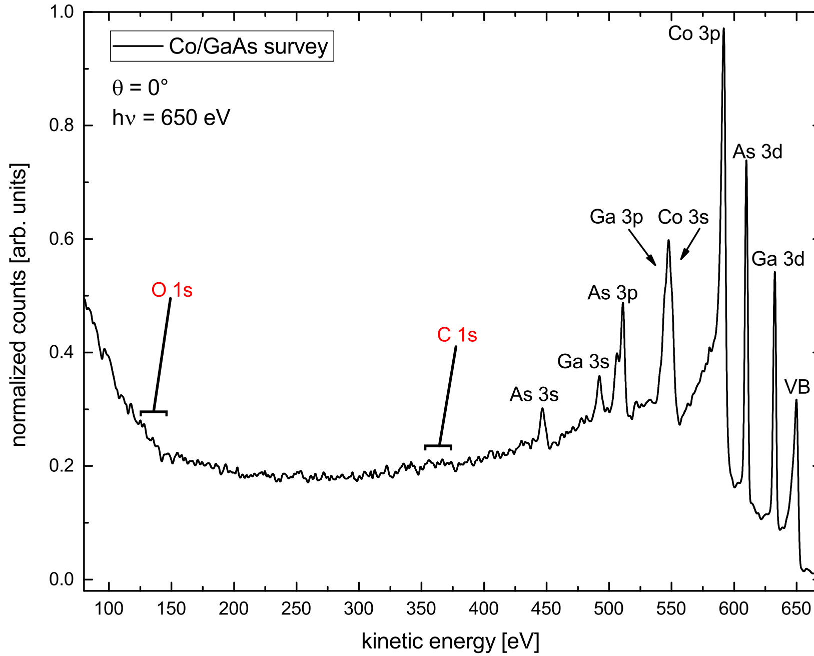

Figure 4.3: Co/GaAs XPS survey spectrum at an incoming photon energy of hν = 650 eV and $\theta = 0°$. Since the Co rod has been degassed before usage and the base pressure is kept $p \approx 8 \times 10^{-10}$ mbar during evaporation, no O and C contaminations are observed. The binding energies of the Ga 3p and Co 3s orbitals differ only by $\Delta \approx 5$ eV and thus appear as one peak due to the high passenergy.

After Co deposition LEED and XPS measurements are performed. The XPS survey spectrum is displayed in Fig. 4.3. As indicated no O or C signals are observed. This is mainly due to excessive degassing of the Co rod and a base pressure of $p \approx 8 \times 10^{-10}$ mbar during the deposition. Due to the low Co film thickness, the Ga and As signals are still observable. As expected, the LEED measurement yielded no pattern [93]. In contrast to reflection high-energy electron diffraction (RHEED) measurements, the LEED pattern for Co/GaAs does not persist for thickness of $d_{\mathrm{Co}} > 2$ Å. A comprehensive LEED discussion is provided in literature [93] and will be further discussed in section 5.1.3. Subsequently, MgO is evaporated on the Co/GaAs(001) sample.

4.3 MgO/Co/GaAs

MgO forms a halite structure with a lattice constant of $a_{\mathrm{MgO}} = 4.212\,\text{Å}$. With a band gap of $\Delta = 7.8\,\mathrm{eV}$ it belongs to the group of insulators. MgO is deposited on Co(bcc) by using a MgO crystal with a purity of 99.95% in a crucible. The evaporation parameters for the evaporator are listed in Tab. 4.3. In order to

Table 4.3: Evaporation parameters to deposit MgO with a thickness of $d_{\mathrm{MgO}} = 3\,\mathrm{ML} - 5\,\mathrm{ML}$ onto Co/GaAs.

Parameter	Value
Filament Current	$I_{\mathrm{Fil}} = 3.02\,\mathrm{A}$
High Voltage	$U_{\mathrm{High}} = 600\,\mathrm{V}$
Emission Current	$I_{\mathrm{Em}} = 38.5\,\mathrm{mA}$
Resulting Power	$P = U_{\mathrm{High}} \times I_{\mathrm{Fil}} = 23.1\,\mathrm{W}$
Duration	$t = 1\,\mathrm{min} - 2\,\mathrm{min}$
Resulting Thickness	$d_{\mathrm{MgO}} = 3\,\mathrm{ML} - 5\,\mathrm{ML}$

investigate at which thickness MgO crystallizes on a Co(bcc) substrate, thicknesses of 3 ML-5 ML [2] in 1 ML steps are deposited. After each deposition step an XPS spectrum and an XPD pattern are recorded. The XPS survey spectrum is displayed for 5 ML in Fig. 4.4.

Since MgO is a compound, it is crucial not to use an evaporation power higher than 28 W. At this power, the Mg-O bonding is dissolved and it is possible that O bonds to Co and thin layers of pristine Mg are deposited. Therefore, after each evaporation step an XPS survey spectrum is recorded. A Mg:O ratio $r_{\mathrm{Mg:O}}$ is calculated from the O $1s$ and Mg $2p$ XPS areas. Since both elements have different energy-depended cross-sections σ_i, a normalization is necessary [95]. An accurate approximation of the ratio is performed according to:

$$h_i = \frac{P_i - U_i}{\sigma_i} \tag{4.1}$$

$$r_{\mathrm{Mg:O}} = \frac{h_{\mathrm{Mg}}}{h_{\mathrm{O}}} \tag{4.2}$$

[2] 1 monolayer (ML) of MgO corresponds to 0.21 nm

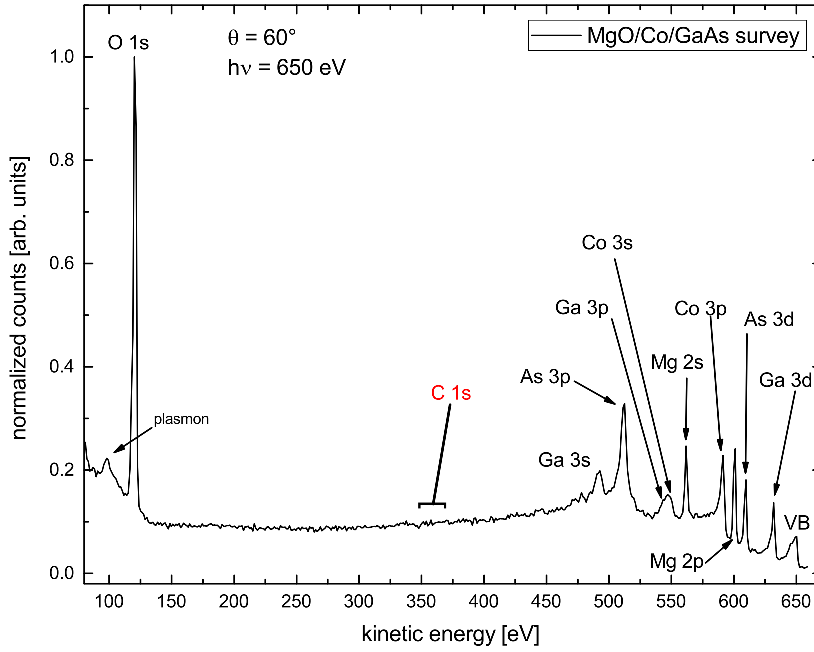

Figure 4.4: MgO/Co/GaAs XPS survey spectrum at an incoming photon energy of hν = 650 eV and $\theta = 60°$. The Mg 2p orbital appears between the Co 3p and As 3d orbitals. Here, the MgO thickness is 5 ML.

whereas P_i is the peak height and U_i is the corresponding background. This formula applies only for very thin films. Generally speaking, the electrons corresponding to O 1s and Mg 2p have different kinetic energies and therefore the probing depth for Mg 2p is higher than for O 1s. Here, since the MgO film is very thin, the electrons originate from all of the deposited layers. Therefore, the kinetic energy is negligible. The $\mathrm{Mg_{2p}}$:$\mathrm{O_{1s}}$ ratio was determined to be always $r_{\mathrm{Mg:O}} \approx$ 1:0.98, which indicates that homogeneous MgO layers are deposited.

5 Results & Discussion

This chapter is divided into two sections wherein the results for the Co/GaAs and MgO/Co interfaces are presented separately.
In the first section, the XPS spectra of As 3*d*, Ga 3*d*, and Co 3*p* before and after Co deposition are presented and analyzed. Then, the FSXPD patterns of these orbitals are analyzed qualitatively. In the second half of the first section, the Co 3*p* and Ga 3*p* XPD patterns and the corresponding simulations with the resulting Co_3Ga interface structure are shown and discussed.
In the second section, the Co 3*p* XPD pattern after MgO evaporation is shown. The structural behavior of MgO is discussed for thicknesses of $3\,\mathrm{ML} - 5\,\mathrm{ML}$. Additionally, the Mg 2*p* XPS spectrum, the corresponding XPD patterns, and the resulting distorted halite structure are shown and put into a scientific perspective.

5.1 Co/GaAs Interface

5.1.1 XPS Analysis

The GaAs(001) c(8×2) surface structure has been investigated by mainly x-ray diffraction (XRD) and scanning tunneling microscopy (STM) measurements in literature [96, 97]. The structure suggested by Kumpf *et al.* with its complex Ga surface- and sub-dimers is widely accepted [98]. In this work, the As 3*d* and Ga 3*d* XPS spectra are recorded and the chemical components are assigned to

Table 5.1: Parameters of the components in the As 3d and Ga 3d spectra resulting from the least squares fit before and after Co deposition. All As and Ga components corresponding to the c(8×2) surface reconstruction vanish after Co deposition in favor of newly arising bondings.

	Label	E_{kin} [eV]	rel. area $\vert_{0°}$	rel. area $\vert_{60°}$	Interpretation
As 3d	A1	214.63	0.812	0.643	As bulk
	A2	215.15	0.188	0.357	$GaAs_3$ surface
Ga 3d	G1	235.96	0.088	0.108	bulk-typed Ga bonding
	G2	236.32	0.294	0.287	Ga sub-surface dimers
	G3	236.55	0.475	0.300	Ga bulk
	G4	236.82	0.143	0.305	$GaAs_3$ surface
After Co deposition					
As 3d	CA1	214.70	0.935	0.875	Co-As
	CA2	214.16	0.042	0.059	As-As
	CA3	213.72	0.104	0.066	Co_xGaAs_{1-x}
Ga 3d	CG1	237.16	0.725	0.572	Ga interface bonding (1)
	CG2	237.04	0.275	0.428	Ga interface bonding (2)

the suggested surface reconstruction. Then, 12 ML of Co are evaporated and the formation of new bondings is observed.

With the element-specific parameters h_{SOC}, Δ_{SOC}, and the background subtraction shown in Tab. 2.1, the As 3d and Ga 3d spectra are fitted with Voigt-profiles. After Co deposition both element-specific spectra are fitted with a DS profile due to the asymmetric line shape. All components of the As 3d and Ga 3d orbitals are listed in Tab. 5.1. The interpretation of each component is provided there as well. The relative areas, the kinetic energies, and resulting interpretations are discussed in the following. The As 3d and Ga 3d spectra recorded at an incoming photon energy of $h\nu = 260\,\text{eV}$ are displayed in Fig. 5.1 and Fig. 5.2. For comparison, the spectra before (a) and after (b) Co deposition are shown in the respective figure. Starting with the XPS spectra before Co deposition, only two components A1 and A2 are necessary to achieve a satisfying fit to the ex-

perimental data in the As 3*d* spectrum. The A1 component at $E_{\text{kin}} = 214.63\,\text{eV}$ corresponds to main arsenic bulk bonding since its relative area decreases heavily from $0.812\big|_{0^\circ}$ to $0.643\big|_{60^\circ}$. The A2 component shifted by $\Delta E_{\text{kin}} = +0.52\,\text{eV}$ is obviously the surface component, also known as the $GaAs_3$ bonding [97], since its relative area increases from $0.188\big|_{0^\circ}$ to $0.357\big|_{60^\circ}$.

The $GaAs_3$ bonding is also found in the Ga 3*d* spectrum as well. The spectrum is shown in Fig. 5.2a. Therein, four components are necessary to achieve a satisfying least squares fit. G4's strong increase from a relative area of $0.143\big|_{0^\circ}$ to $0.305\big|_{60^\circ}$ highly indicates a surface component. Considering that the element-specific cross-section σ_i and the IMFP for both spectra are roughly the same [59, 95], it is remarkable that the relative area of G4 is roughly same as A2's area in the As 3*d* spectrum. Therefore, it is concluded that G4 corresponds to the $GaAs_3$ surface bonding as well [99]. The G1 component's relative area at $E_{\text{kin}} = 235.96\,\text{eV}$ does not change significantly for different emission angles θ. Therefore, this bonding is found in the surface and in the bulk equally. It might be a bulk-typed Ga bonding and can not directly be assigned to Kumpf's structure model. The G2 component at $E_{\text{kin}} = 236.32\,\text{eV}$ corresponds to the Ga subsurface dimers in the Kumpf c(8×2) model. Their kinetic energy corresponds well to the Ga-Ga bonding suggested in literature [100]. These dimers arise due to a Ga-rich surface reconstruction and the lack of As bonding partners. They cause an apparent (4×2) surface reconstruction in the LEED pattern and have been illustrated in Fig. 4.2. The G3 component at $E_{\text{kin}} = 236.55\,\text{eV}$ is the largest with a relative area of $0.475\big|_{0^\circ}$ and it decreases heavily to $0.300\big|_{60^\circ}$ in the surface sensitive measurement. Thus, it corresponds to the main Ga bulk component.

After Co deposition, all of the described components in the As 3*d* and Ga 3*d* XPS spectra, i.e. A1 - A2 and G1 - G4, vanish and new bondings are formed. Qualitatively, both spectra become asymmetric. This is due to the metalization of GaAs [87, 94]. By contacting GaAs to Co, the Ga and As spectra gain an intrinsic asymmetry since the new chemical bondings. Therefore, a DS profile with an asymmetry factor α is used instead of a Lorentz profile. The resulting least squares fits for As 3*d* and Ga 3*d* are shown in Fig. 5.1b and Fig. 5.2b,

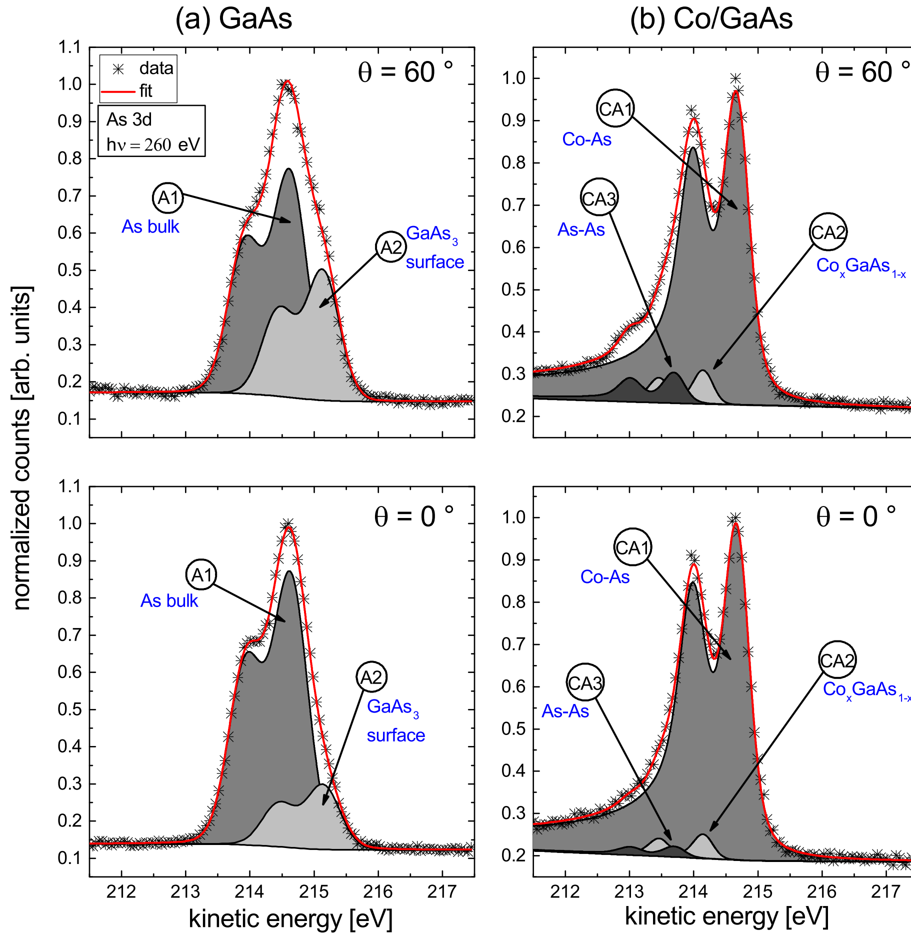

Figure 5.1: High resolution XPS spectra of As 3d before (a) and after (b) Co deposition at $\theta = 60\,°$ (top) and $\theta = 0\,°$ (bottom). The spectra were recorded at an incoming photon energy of hν = 260 eV. Compared to A1, the surface component A2 rises from 0 ° to 60 °. After Co deposition, A1 and A2 vanish and CA1 - CA3 arise. CA1 corresponds to the main amorphous Co-As phase. CA2 and CA3 correspond to minor near surface phases. The interpretation of each component is labeled in blue.

respectively. In the As 3d spectrum, the CA1 component matches to the Co-As bonding perfectly since it is the largest with a relative area of $0.935\big|_{0°}$ [87]. The minor CA2 and CA3 components do not change significantly in area. Sim-

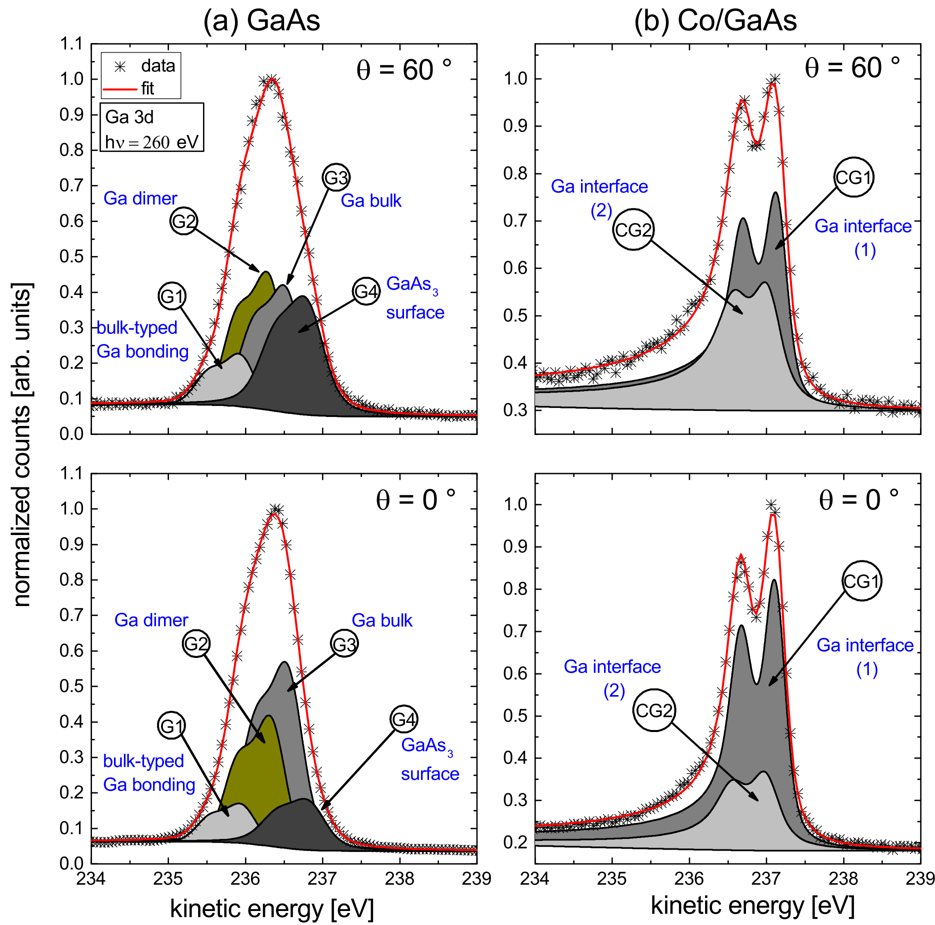

Figure 5.2: High resolution XPS spectra of Ga 3d before (a) and after (b) Co deposition at $\theta = 60\,°$ (top) and $\theta = 0\,°$ (bottom). The spectra were recorded at an incoming photon energy of hν = 260 eV. G1, G2, and G4 correspond to bondings within the c(8×2) surface reconstruction. G3 indicates the substrate bonding. All G1 - G4 components at $E_{\text{kin}} \leq 237$ eV vanish and the CG1 and CG2 components arise after Co deposition. This highly indicates that a new bonding is formed. The interpretation of each component is labeled in blue.

ilar behavior has been reported for the As-As and Co_xGaAs_{1-x} compounds in literature [94].

The Ga 3d spectrum reveals two newly formed components CG1 and CG2 that are shifted by more than $\Delta E_{\text{kin}} > 0.8$ eV to higher kinetic energies in comparison

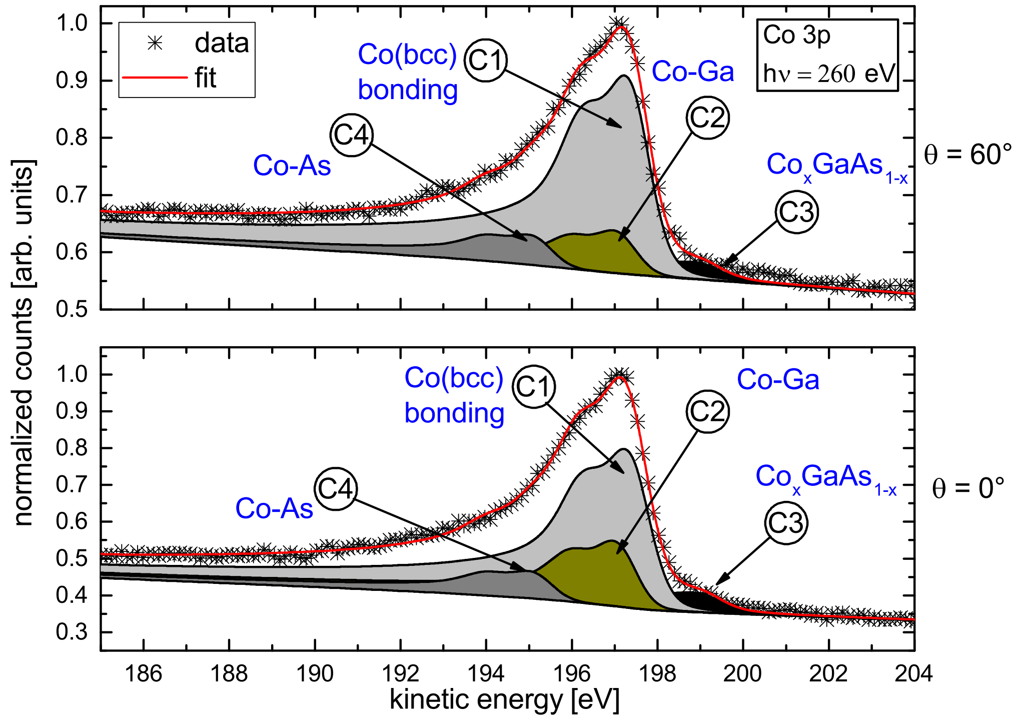

Figure 5.3: High resolution XPS spectra of Co 3p in Co/GaAs at $\theta = 60\,^\circ$ (top) and $\theta = 0\,^\circ$ (bottom). The spectra were recorded at an incoming photon energy of hν = 260 eV. C1 is the main Co(bcc) component where as C2 corresponds to the Co-Ga bonding. C4 indicates the amorphous $\mathrm{Co}_x\mathrm{As}_{1-x}$ phase suggested in the As 3d orbital. C3 corresponds to the $\mathrm{Co}_x\mathrm{GaAs}_{1-x}$ bonding. The interpretation of each component is labeled in blue.

to the G1 - G4 components in the pristine Ga 3d spectrum. This clearly shows that the former Ga-rich c(8×2) surface reconstruction is lifted in favor of newly formed Ga bondings. The CG1's relative area of $0.725\big|_{0^\circ}$ is significantly higher than CG2's $0.275\big|_{0^\circ}$. Yet at $\theta = 60°$, the area ratios are roughly the same with $0.572\big|_{0^\circ}$ for CG1 and $0.428\big|_{60^\circ}$ for CG2. This indicates that both bondings are stacked within the interface region, whereas CG2 is closer to the surface than CG1. Further, since only an energetic difference of $\Delta E_{\mathrm{kin}} = 0.12\,\mathrm{eV}$ is observed, it is concluded that both chemical states do not differ heavily from each other. In the As 3d spectrum a $\mathrm{Co}_x\mathrm{GaAs}_{1-x}$ is suggested. This component is missing

in the Ga 3d spectrum. A closer look at the experimental data at an energy of $E_{\text{kin}} \approx 236\,\text{eV}$ might suggest an additional component. Yet, since the CG1 and CG2 components are dominating the peak, no further conclusions can be drawn from the experimental data.

Table 5.2: Components for a least squares fit in the Co 3p spectra after Co deposition. A Tougaard background and a DS profile was used to obtain a satisfying fit to the data.

Label	E_{kin} [eV]	rel. area $\big\vert_{0^\circ}$	rel. area $\big\vert_{60^\circ}$	Interpretation
C1	197.45	0.589	0.689	main Co(bcc) bonding
C2	197.14	0.225	0.137	Co-Ga beneath Co(bcc)
C3	199.09	0.083	0.067	asym. shape correction
C4	195.27	0.103	0.106	amorphous Co-As

Similar behavior is seen in the Co 3p XPS signal as shown in Fig. 5.3. The resulting parameters from the least squares fit for these Co 3p spectra are listed in Tab. 5.2. The component labeled C1 at $E_{\text{kin}} = 197.45\,\text{eV}$ corresponds to the main Co bonding since it matches perfectly to the energetic position of Co provided in literature [101]. C2 indicates the Co-Ga bonding that has formed after Co deposition. Since it decreases from a relative area of $0.225\big\vert_{0^\circ}$ to $0.137\big\vert_{60^\circ}$, it is concluded that the C1 bonding is stacked on top of the C2 bonding. The component C3 located at $E_{\text{kin}} = 199.09\,\text{eV}$ corresponds perfectly to the Co_xGaAs_{1-x}. This is deduced from its relative area of $0.083\big\vert_{0^\circ}$ which is very small. The same behavior applies for the Co_xGaAs_{1-x} component CA2 in the As 3d spectrum. The component labeled C4 does not change significantly at different polar angles matching to the discussed Co-As bonding. This means that the interdiffused As forms a bonding to Co and is found throughout the whole deposited Co layers. But since its area is very small it is concluded that the As diffusion is kept very low. That fits to the expectation that a Ga-rich surface reconstruction suppresses As diffusion to a minimum.

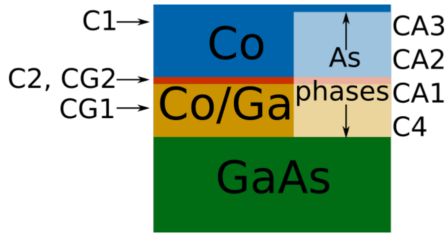

Figure 5.4: Schematic conclusion of the layer system from the XPS analysis.

The XPS analysis is summed up in Fig. 5.4. Concluding from the XPS analysis, after Co deposition no chemical states referring to the Ga sub-dimers or $GaAs_3$ compound are detected. In the As 3d and Ga 3d signals, all chemical states from the GaAs(001) c(8×2) reconstruction vanish in favor of newly formed bondings. The CoAs bonding is found throughout the sample whereas the As-As and Co_xGaAs_{1-x} compounds are located within the topmost deposited layers. From the Co 3p and Ga 3d spectra, it is concluded that two stacked Co-Ga chemical states arise beneath the Co(bcc) layers.

5.1.2 XPD Analysis

In the following, the structural analysis is first performed with FSXPD[1] in order to obtain qualitative information due to the interface's complexity and then the XPD patterns[2] are taken into account to determine the exact loacal environment of the interface structure. Note that the FSXPD patterns are recorded at an incoming photon energy of $E_{\mathrm{Ph}} = 550\,\mathrm{eV}$ and the XPD patterns correspond to the presented XPS spectra at $E_{\mathrm{Ph}} = 260\,\mathrm{eV}$. Therefore, the probing depth in FSXPD patterns is significantly larger than in the previously discussed XPS spectra.

The experimental FSXPD patterns of As 3d and Ga 3d before Co deposition are displayed in Fig. 5.5. In spite of the complex c(8×2) surface reconstruction, the zinc blende structure provides the dominating intensity modulations. This is well explained by the SFA. Compared to the bulk zinc blende structure, the surface reconstruction is very thin, i.e. two layers. Therefore, the atoms from the surface reconstruction do not contribute significantly to the measured FSXPD

[1]FSXPD: x-ray photoelectron diffraction wherein only forward scattering is considered.
[2]XPD: x-ray photoelectron diffraction wherein strong side characteristics in the SFA are considered as well.

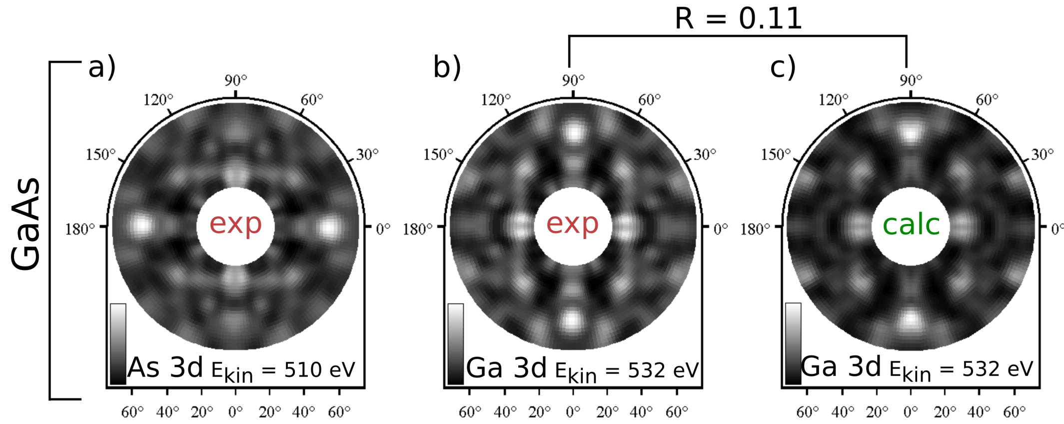

Figure 5.5: FSXPD pattern of As 3*d* (a) and Ga 3*d* (b) in GaAs. The calculated XPD pattern for Ga 3*d* (c) in GaAs is displayed as well. Since GaAs crystallizes in zinc-blende structure the As 3*d* (a) is rotated by 90 ° compared to Ga 3*d* (b).

pattern. This occurs due to the elevated kinetic energy of $E_{\text{kin}} > 500\,\text{eV}$ as discussed in chapter 2.2. Further, by simply rotating the As 3*d* pattern by 90°, it is transformed into the Ga 3*d* pattern due to the Ga and As positions in the zinc blende structure. Thus, to avoid redundancy only the calculated Ga 3*d* XPD pattern is presented in Fig. 5.5c. An R-factor of $R^{\text{GaAs}}_{\text{Ga } 3d} = 0.11$ indicates a good accordance between experiment and simulation. The resulting structure obtained from the Ga 3*d* XPD simulation is a pristine zinc blende structure without surface reconstruction.

After Co deposition, the intensity modulations change significantly for the As 3*d* and Ga 3*d* orbital as shown in Fig. 5.6a and Fig. 5.6b. Now, the As 3*d* pattern cannot be transfered into the Ga 3*d* pattern by simply rotating it by 90°. Instead, 4-folded symmetry elements are observed as highlighted in red. They are observed in the Ga 3*d* pattern after Co deposition as well. Obviously, these forward scattering maxima arise from the Co(bcc) structure on top of GaAs. Therefore, they appear in the As pattern as well since the As 3*d* photoelectrons are diffracted at the bcc structure on their path to the surface. Yet, in the As 3*d* pattern there are still intensity modulations that refer to the pristine zinc blende structure marked in blue. These modulations are not observed in the Ga

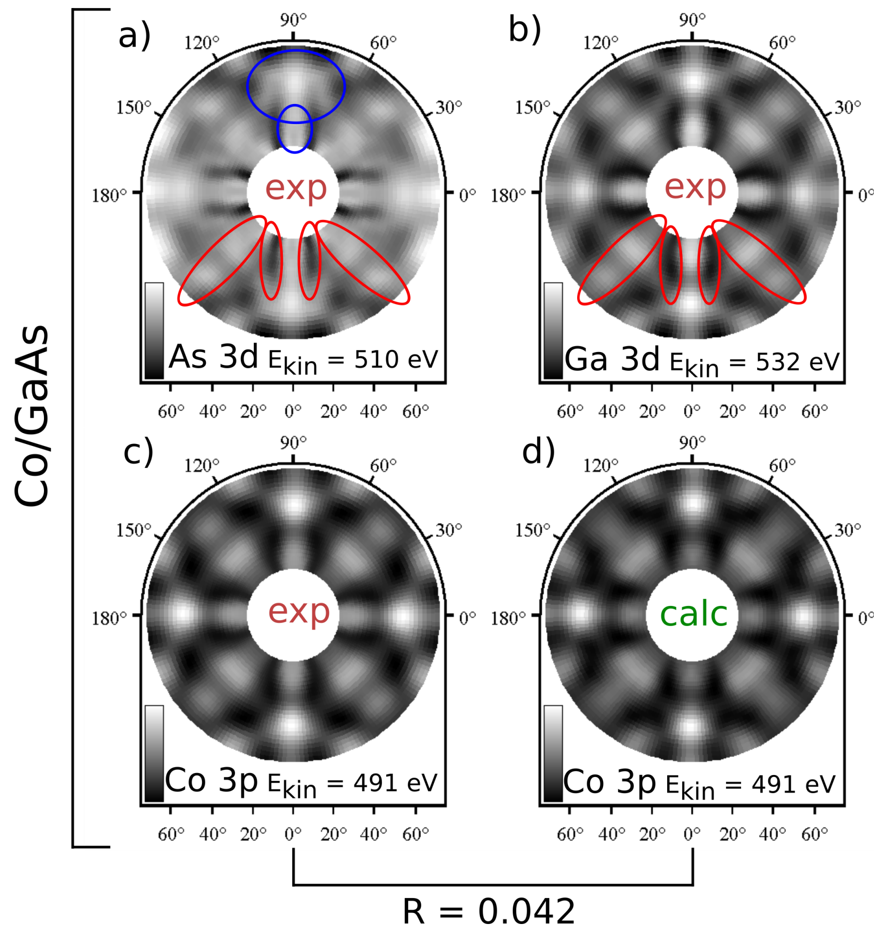

Figure 5.6: FSXPD pattern of As 3*d* (a) and Ga 3*d* (b) Co 3*p* (c) in Co/GaAs. The calculated XPD pattern for Co 3*p* (d) is displayed as well. After Co deposition, the Ga 3*d* pattern shows the same anisotropy function as Co 3*p*. The As 3*d* pattern shows elements of the GaAs zinc-blende (marked in blue) and the four-folded symmetry of the Ga 3*d* pattern (marked in red).

3*d* pattern. Apparently, the interface structure seems to dominate the Ga 3*d* pattern but not the As 3*d* pattern. Instead, the Ga 3*d* pattern shows the exact same modulation like the Co 3*p* pattern shown in Fig. 5.6c.

As discussed in chapter 2.2, the scattering factor amplitude (SFA) is sharp and has no secondary maxima for high kinetic energies. Thus, the FSXPD patterns for crystalline structures show distinct and sharp maxima in the intensity

modulation. Comparing the overall intensity modulation before and after Co deposition in the As $3d$ pattern, the expected sharp and strong modulations are smeared out. Large areas of relatively low intensity modulations arise. This strongly alludes to a chemical state that is amorphous, causing a significant reduction of the intensity modulation. Therefore, it is concluded that the modulations marked in blue arise from the zinc blende structure of GaAs and the modulations marked in red correspond to a 4-folded symmetric structure on top of GaAs. Therein, As is amorphous.

Since the Ga $3d$ and Co $3p$ patterns show the same intensity modulations, both elements are necessarily located in the same structural environment. As stated, it is well known that Co grows in a bcc structure. Again, to avoid redundancy only the Co $3p$ patterns is calculated for a pristine bcc structure in Fig. 5.6d. An astonishing R-factor of $R^{\mathrm{bcc}}_{\mathrm{Co}\ 3p} = 0.042$ is achieved. Because FSXPD is not chemically sensitive like full scattering XPD patterns, only a set of structures for the unknown Ga structure can be deduced from these patterns. Obviously, it needs to be a 4-folded cubic unit cell like in Co(bcc) structure. From the angle-resolved Ga $3d$ and Co $3p$ XPS measurements it becomes clear that the Ga structure formation is sandwiched between GaAs(001) and Co(bcc). Possible Ga structures are Ga(bcc), Ga(fcc), CoGa(NaCl), CoGa(CsCl), CoGa($D0_3$), combinations of these, like a NaCl structure stacked on top of CsCl structures, and even only partially face centered unit cells. All possible structures can be summed up by a distinct point group. In Hermann-Mauguin notation, it is the $m\bar{3}m$ point group or O_h in Schönfließ notation [102].

In order to determine the exact structure, chemical sensitive XPD is necessary. The XPD patterns corresponding to the presented XPS measurements at an incoming photon energy $E_{\mathrm{Ph}} = 260\,\mathrm{eV}$ are displayed in Fig. 5.7.

As seen in Fig. 5.7a, the As $3d$ XPD pattern shows no significant intensity modulations after Co deposition, i.e. all XPS components CA1 - CA3, that arise in the As $3d$ spectrum shown in Fig. 5.1, are amorphous. However, it is clear that within the probing depth only the As phases that do not correspond to the GaAs bulk are revealed since no bulk-typed XPS component is observed in the As $3d$

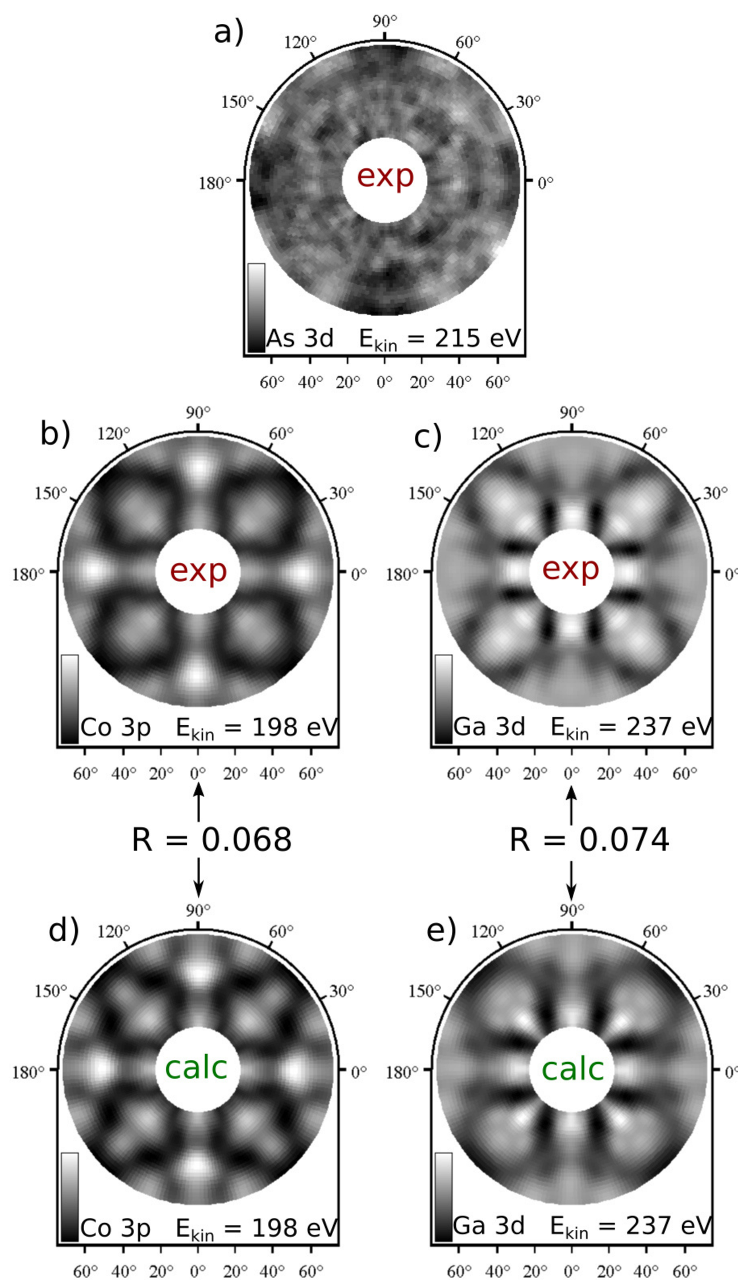

Figure 5.7: As 3*d* (a), Co 3*p* (b), and Ga 3*d* (c) XPD patterns at an incoming photon energy of $E_{\mathrm{Ph}} = 260\,\mathrm{eV}$ resulting in kinetic energies of $E_{\mathrm{kin}} = 198\,\mathrm{eV} - 237\,\mathrm{eV}$. Every point in the XPD pattern corresponds to a full XPS spectrum. As 3*d* shows a highly amorphous phase. The calculated Co 3*p* (d) and Ga 3*d* (e) patterns indicate a perfect accordance between simulation and experiment. Both calculated XPD patterns correspond to the $D0_3$ structure.

XPS spectrum. Any modulations from the bulk GaAs would have been detected at low polar angles, i.e. $\theta \leq 20°$. This matches the As 3d XPS spectrum perfectly because the main bulk component A1 vanishes after Co deposition. Therefore, no GaAs bulk material is probed in contrast to the FSXPD measurement wherein GaAs's zinc blende structure was observed.

The Co 3p and Ga 3d XPD patterns are displayed in Fig. 5.7b and Fig. 5.7c, respectively. They hugely differ to the FSXPD pattern where they showed exactly same intensity modulations. The difference occurs, because the element-specific potential plays a much larger role in the SFA in XPD measurements, as discussed in chapter 2.2.1. Yet, both patterns show roughly the same characteristics like the 4-folded symmetry and the intensity maxima at azimuth angles of $\phi = 30° - 60°$. Considering the conclusions from the FSXPD measurements, it is necessary to evaluate a structure that corresponds to the Ga 3d and Co 3p pattern equally well with a good R-factor. All structures from the $m\bar{3}m$ point group with different thicknesses have been taken into account. In Fig. 5.8 the Co 3p and Ga 3d R-factors for some interface structures from the $m\bar{3}m$ point group are presented. The $D0_3$ structure is the only structure that yields R-factors

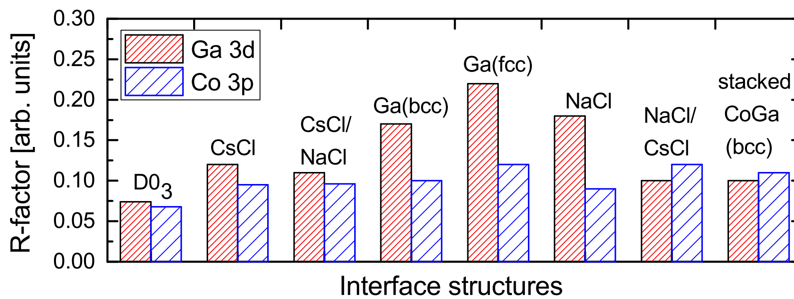

Figure 5.8: R-factor minima for various interface structure formation between Co(bcc) and GaAs in pristine zinc blende. The Co R-factor does not change significantly for different interface structures since its simulation is dominated by Co(bcc) on top of the interface.

$R_i < 0.1$ for Co and Ga. The calculated Co 3p and Ga 3d patterns are presented in Fig. 5.7d and Fig. 5.7e, respectively, and the corresponding structure is de-

picted in Fig. 5.9. With R-factors of $R^{\mathrm{D0_3}}_{\mathrm{Co}\,3p} = 0.068$ and $R^{\mathrm{D0_3}}_{\mathrm{Ga}\,3d} = 0.074$ a perfect match is indicated. The obtained Co:Ga ratio yields a Co_3Ga alloy formation.

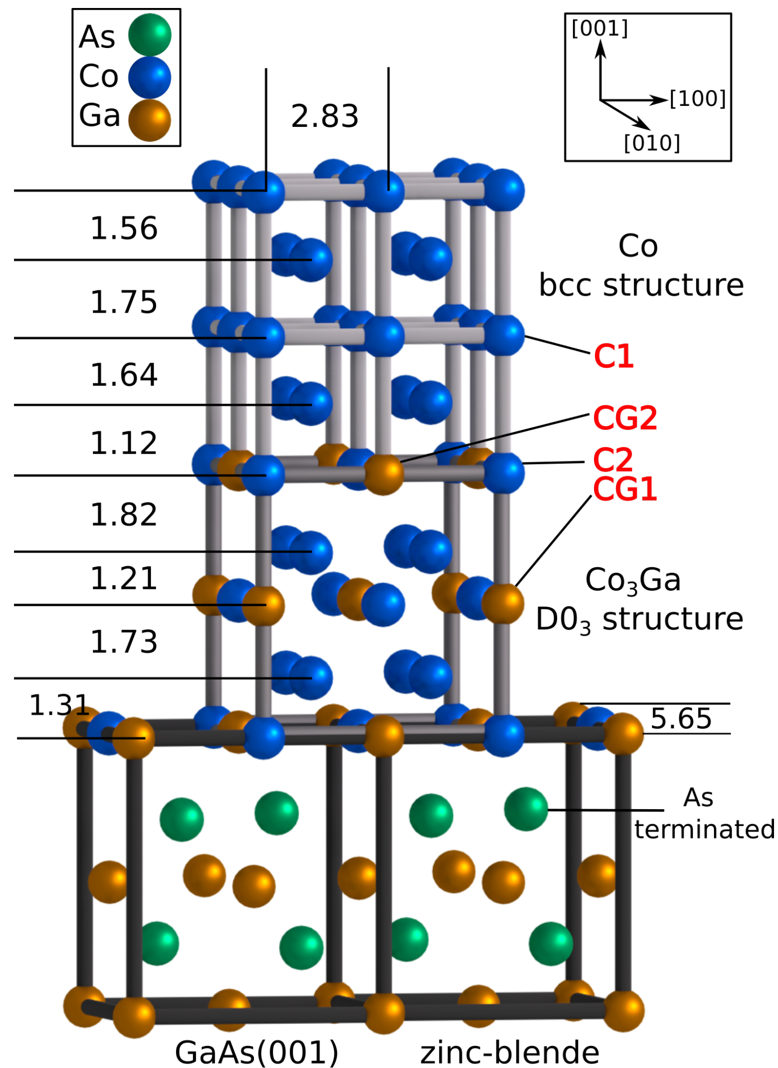

Figure 5.9: Resulting structure from the chemical state specific XPD analysis. A Co_3Ga alloy in $D0_3$ structure arises after Co deposition on a clean c(8×2) GaAs(001) surface reconstruction. The discussed XPS components C1, C2, CG1, and CG2 match perfectly to the evaluated structure. Their origins are labeled in red. The first layers of Co(bcc) grown after Co_3Ga formation show a relaxation in [100] direction.

All provided R-factors are the minima obtained from the genetic algorithm considering lattice site variations. The simulation algorithm shows that the Co $3p$ pattern is mainly sensitive to the Co(bcc) structure and shows only minor differences for various Co-Ga interface structures. This can be explained with the information from the Co $3p$ XPS signal. The C1 component corresponding to the main Co(bcc) bonding is the largest in area. Therefore, its intensity modulations conceal the modulations of the C2 component corresponding to the $D0_3$ interface. In contrast, a variation of the Co-Ga interface structure resulted in a much poorer R-factor minimum of up to $R^{\text{fcc}}_{\text{Ga }3d} = 0.22$ in the Ga $3d$ pattern. Even a stacked CoGa(bcc) structure was considered wherein each single bcc layer consists of either Co or Ga only. Although, this structure seems promising at a first glance since both R-factors are at $R_i \approx 0.1$, a significant improvement is achieved with the $D0_3$ structure. Further, the $D0_3$ structure corresponds perfectly to the Ga $3d$ XPS measurements. Both detected chemical environments CG1 and CG2 can be assigned to the $D0_3$ structure as labeled in Fig. 5.9.

In the Ga $3d$ XPS spectrum a weak energetic shift of $\Delta_{\text{CG1 - CG2}} = 0.12\,\text{eV}$ is observed. This shift is perfectly explained by their next nearest-neighbor bonding in the Co_3Ga alloy. The near-neighbor environment of one Ga atom always consists of three Co atoms within the Co_3Ga alloy. This corresponds to the CG1 bonding. The next nearest-neighbor bonding partner is either a Co atom from the bcc structure or a Ga atom from the $D0_3$ structure. Since the next nearest-neighbor atom has a relatively small but not negligible effect on the binding energy, the difference in kinetic energies for CG1 and CG2 is very small in the XPS spectrum. Therefore, the next nearest-neighbor bonding environment leads to the CG2 XPS component. Thus, all Co and Ga chemical components from the XPS measurements can be assigned to the evaluated $D0_3$ structure. They are labeled in red in Fig. 5.9. Additionally, the exact atom lattice sites are provided as well. In [100] and [010] directions, the lattice constants match to the GaAs' lattice constant $a_{\text{GaAs}} = 5.654\,\text{Å}$ perfectly. Due to the interface interaction each layer of the $D0_3$ unit cell is slightly shifted in [001] direction, i.e. a relaxation occurs.

On top of the $D0_3$ alloy, Co(bcc) grows epitaxially with a lattice constant of $a_{\mathrm{Co}} = 2.83\,\text{Å}$ in [100] and [010] direction. Yet, large shifts occur in each layer in [001] direction as labeled in Fig. 5.9. The effects of these shifts will be discussed in chapter 5.1.3.

5.1.3 Discussion

Xu *et al.* reported that the GaAs surface reconstruction is preserved after growing a Co film on either GaAs(110) or GaAs(001) [103]. Here, no indication of a preserved surface reconstruction is found. With Xu's Co thickness depending XPS measurements, a precise chemical resolution within the Co layers was achieved. Yet, no structural determination was possible. From the XPD measurements in this work, a precise lattice site determination with chemical resolution is provided. In Fig. 5.10 the experimental Ga 3*d* XPD pattern (a) is compared to the calculated Ga 3*d* patterns resulting from a lifted surface reconstruction (b) and a preserved reconstruction (c).

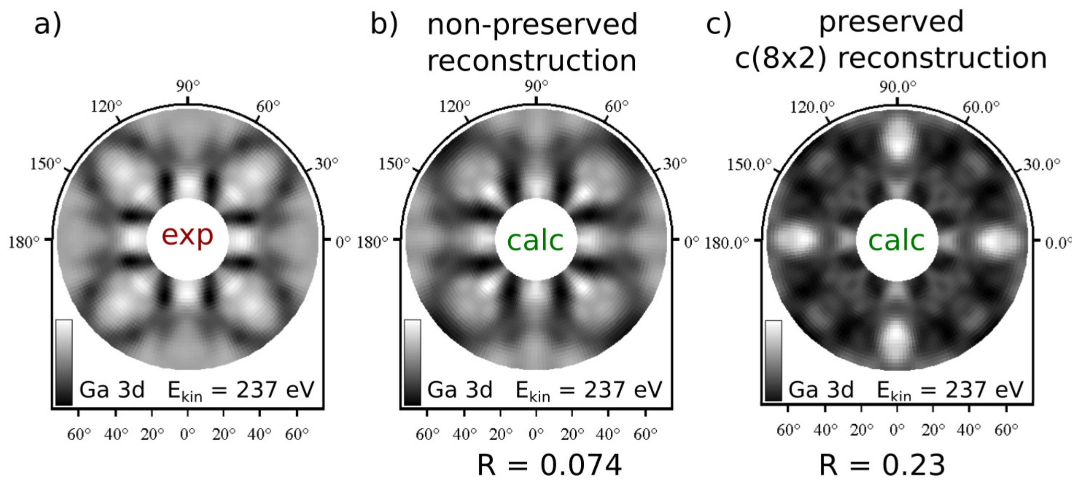

Figure 5.10: Experimental Ga 3*d* XPD pattern (a), calculated Ga 3*d* XPD pattern with an As-terminated GaAs(001) structure (b) and calculated Ga 3*d* XPD pattern with a preserved GaAs(001) c(8×2) surface reconstruction (c). With a lifted surface reconstruction the R-factor is remarkably better with $R = 0.074$ compared to a preserved surface reconstruction which yields $R = 0.23$.

Choosing the GaAs c(8×2) surface reconstruction beneath the $D0_3$ structure yields a R-factor of $R_{\mathrm{Ga}\ 3d} = 0.23$, which is remarkably higher than the evaluated one for the non-preserved As-terminated reconstruction $R^{\mathrm{D0_3}}_{\mathrm{Ga}\ 3d} = 0.074$. Therefore, it is concluded that the GaAs c(8×2) surface reconstruction is lifted

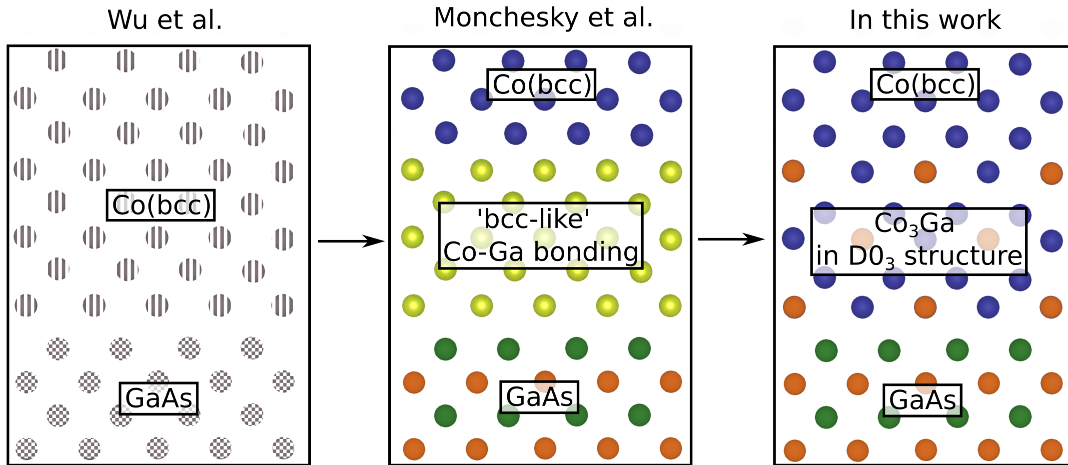

Figure 5.11: Comparison of interface models suggested by Wu *et al.* [105, 106] derived from TEM measurements, Monchesky *et al.* [104] derived from RHEED measurements, and within this work derived from XPD measurements. Clearly, without chemical information the $D0_3$ structure is indistinguishable from a pristine bcc structure.

in favor of As-terminated GaAs structure. A Ga-termination results in a rise of the R-factor by 0.001, which is insignificant. This is because the XPD measurements do not penetrate the top most layers effectively. Therefore, the intensity modulations from Co_3Ga and Co(bcc) are dominating. It can be concluded that no surface reconstruction is found but either an As- or a Ga-terminated zinc blende structure is formed.

Wu *et al.* performed transmission electron microscopy (TEM) measurements and Monchesky *et al.* investigated the Co/GaAs interface region with reflection high-energy electron diffraction (RHEED) [104–106]. Wu *et al.* determined the lattice constant of GaAs and Co(bcc) with remarkable precision and found an abrupt interface according to their TEM measurements. Monchesky *et al.* refined that statement and predicted a 'bcc-like' Co-Ga interface structure with an amorphous As phase near to the surface. Yet, both methods do not provide chemical sensitive information. Within the presented $D0_3$ structure model Co and Ga are located at the same lattice sites as Co atoms in a bcc structure. In Fig. 5.11 the evolution of the interface determination is presented. Neglecting the chemical information, the Co_3Ga alloy looks like a pristine Co(bcc) film.

Therefore, with techniques like TEM and RHEED the Co_3Ga alloy in $D0_3$ was not resolvable. Only a chemical sensitive technique like XPD can distinguish the local environment of Ga and Co within the interface.

Addressing the lack of any LEED spots shown in the preparation section 4, Blundell *et al.* compared Fe/GaAs(001) and Co/GaAs(001) by LEED and RHEED measurements [93]. They found out that after depositing 2 Å of Co the LEED pattern vanishes while the RHEED pattern persists. With the angle-resolved XPS spectra provided here in Fig. 5.1, it is clearly shown that As compounds, namely CA2 and CA3, are located within the top most Co layers. As shown in Fig. 5.7, the As 3*d* XPD pattern reveals that these compounds are amorphous. Considering that in LEED measurements low energetic electrons are used, it is clear that amorphous compounds break the symmetry of the top most layers and therefore no LEED pattern arises. In contrast, since in RHEED measurements high energetic electrons are used, a larger periodicity and area are probed and thus it is averaged over the amorphous As components. Thereby, the lack of LEED spots during the Co/GaAs(001) preparation is explained.

Taking the XPS measurements into account, only two components where observed in the Ga 3*d* spectrum and three components in the As 3*d* spectrum after Co deposition. Lüdge *et al.* performed very low energetic XPS measurements at $E_{\mathrm{kin}} \approx 100\,\mathrm{eV}$ [94]. Although components CG1 and CG2 from the Ga 3*d* spectrum and components CA1-CA3 from the As 3*d* spectrum were observed as well, their spectrum yielded one additional component in each spectrum. This is mainly because of the GaAs surface reconstruction, which they used. They prepared an As-rich c(4×4) surface reconstruction which leads to a stronger As diffusion in general [87]. Moreover, a non-magnetic dead layer arises after Co deposition on an As-rich surfaces due to As microstructure formation [83]. In this work, a Ga-rich surface is chosen, since it effectively reduces the As diffusion. A strong indicator for that is the lack of a Ga XPS component at $E_{\mathrm{kin}} \approx 235.0\,\mathrm{eV}$ and an As XPS component at $E_{\mathrm{kin}} \approx 215.5\,\mathrm{eV}$ [87]. Further, the CG1 and CG2 component, that also have been observed by Lüdge *et al.*, can directly be as-

signed to the $D0_3$ structure resulting from the angle-resolved XPS measurement and XPD calculations leaving no room for further interface speculations.

In general, finding a Co_3Ga alloy in $D0_3$ structure on GaAs(001) is very remarkable in terms of current research. For example, the ferromagnetic Fe_3Si alloy is found to have the same $D0_3$ structure on GaAs(001) as well [107]. Fe_3Si shows significantly high magnetic moments with a value of 1050 emu/cm^3 [3] and thus exceeds the one of the Co_2FeSi Heusler alloy by a factor of 2 [108]. Further, Manzke *et al.* optimized the Fe_3Si fabrication on GaAs(001) and showed that for application it is much more suitable than Co_2FeSi [109, 110]. As derived from the XPD calculations, Co_3Ga's lattice constants match to the one of GaAs(001) perfectly. The same behavior is seen for Fe_3Si, which mainly arises due to the $D0_3$ structure for both. Therefore, a Co_3Ga might be promising in terms of current spintronic research as well.
Fe_3Ga is another example, which is very similar to Co_3Ga not only because of the $D0_3$ structure but also due to a bonding of a ferromagnetic transition metal to Ga. Fe_3Ga is well known as *galfenol*. Because of a bonding to Ga in a 1:3 ratio, Fe's magnetostrictive effect is enhanced by a factor of up to 10 [111]. Thus, discovering a Co_3Ga crystalline alloy might lead to similar behavior.
Jamer *et al.* showed that V_3Al becomes an antiferromagnetic gapless semiconductor arising from the $D0_3$ structure with promising thermoelectric properties [112, 113]. Therefore, the Co_3Ga alloy might as well show a significant change in band structure.

[3] 1 emu= 10^{-3} Am^2 = $10^{-3}\frac{\text{J}}{\text{T}}$

5.2 MgO/Co interface

5.2.1 XPS Analysis

The research the MgO/Co(bcc) interface has mainly been carried out by TEM, x-ray magnetic circular dichroism (XMCD), and x-ray diffraction (XRD) measurements in literature [7, 114]. As a result, Yuasa *et al.* showed that the interface structure of MgO/Co(bcc) is flatter and more suitable for applications than MgO/Fe(bcc). In this work the MgO/Co(bcc) interface is analyzed by XPS and (FS)XPD measurements.

Therefore, a MgO film of a thickness of 3 ML-5 ML is deposited on Co(bcc) in steps of 1 ML. After each evaporation step, Co 3*p* and Mg 2*p* XPS spectra as well as XPD patterns are recorded.

Like in chapter 5.1, the analysis starts with the recorded XPS spectra. In Fig. 5.12 the Co 3*p* spectra for 0 ML and 5 ML and the Mg 2*p* spectra for 3 ML and 5 ML of MgO are presented. The Co 3*p* and Mg 2*p* XPS spectra are recorded with an incoming photon energy of $h\nu = 260\,\mathrm{eV}$. As a first result, the Co 3*p* XPS spectrum does not change significantly after MgO deposition. Even after depositing 5 ML of MgO no changes are observed aside poorer statistics for higher MgO film thicknesses. According to literature, possible Co-O formation should arise at $E_{\mathrm{kin}} < 194\,\mathrm{eV}$ [101]. Clearly, Co does not oxidize nor does it form new bondings.

For Mg 2*p*, a similar behavior is observed. The overall XPS line shape does not change meaning the photoelectron intensity ratios of bondings in a MgO film with a thickness of 3 ML are the same as for a 5 ML film. For a quantitative analysis, the Mg 2*p* XPS spectra with a coverage of 5 ML recorded at $\theta = 0°$ and $\theta = 60°$ are fitted. With the element-specific parameters h_{SOC}, Δ_{SOC}, and the background subtraction shown in Tab. 2.1, a Voigt-profile is considered for Mg 2*p* spectrum. The XPS spectrum is depicted in Fig. 5.13. In there, only two components are necessary to achieve a satisfying least squares fit. Both

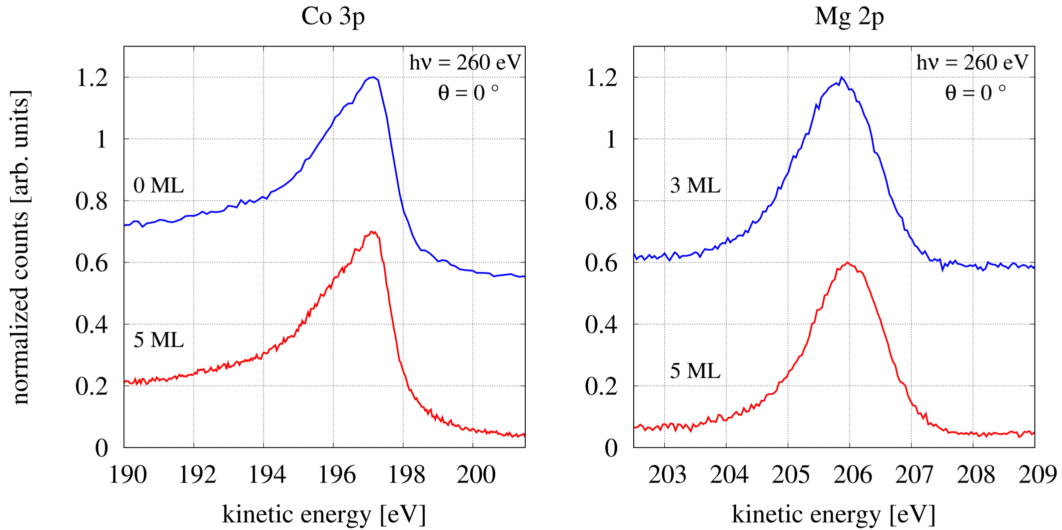

Figure 5.12: High resolution Co 3*p* (left) and Mg 2*p* (right) XPS spectra for 0 ML, 3 ML, and 5 ML of MgO recorded at hν = 260 eV and $\theta = 0°$. Qualitatively, both spectra do not change significantly for different film thicknesses.

Table 5.3: Components in the Mg 2*p* spectrum from the least squares fit after depositing 5 ML of MgO. Depositing 3 ML results in the same components with higher experimental uncertaintybars during the fit procedure.

Component	E_{kin} [eV]	rel. area$\big\|_{0°}$	rel. area$\big\|_{60°}$	Interpretation
M1	205.84	0.884	0.829	main Mg-O bonding
M2	204.81	0.116	0.171	surface effect

components and their relative areas are listed in Tab. 5.3. As seen in the As 3*d*, Ga 3*d*, and Co 3*p* XPS spectra, bondings lead to a significant change in relative area in angle-resolved XPS measurements. Here in the Mg 2*p* spectrum, the relative area of the minor component M2 at $E_{\text{kin}} = 204.81$ eV rises from $0.116\big|_{0°}$ to $0.171\big|_{60°}$ according to the fitting parameters. This change is considered to be rather small and therefore highly unlikely to be a surface bonding effect. From the XPS measurement, no more interpretation can be performed for M2. The M1 component with a relative area of $0.884\big|_{0°}$ corresponds to the main Mg-O

bonding and fits to XPS measurements in literature [115]. This is discussed in detail below in section 5.2.3.

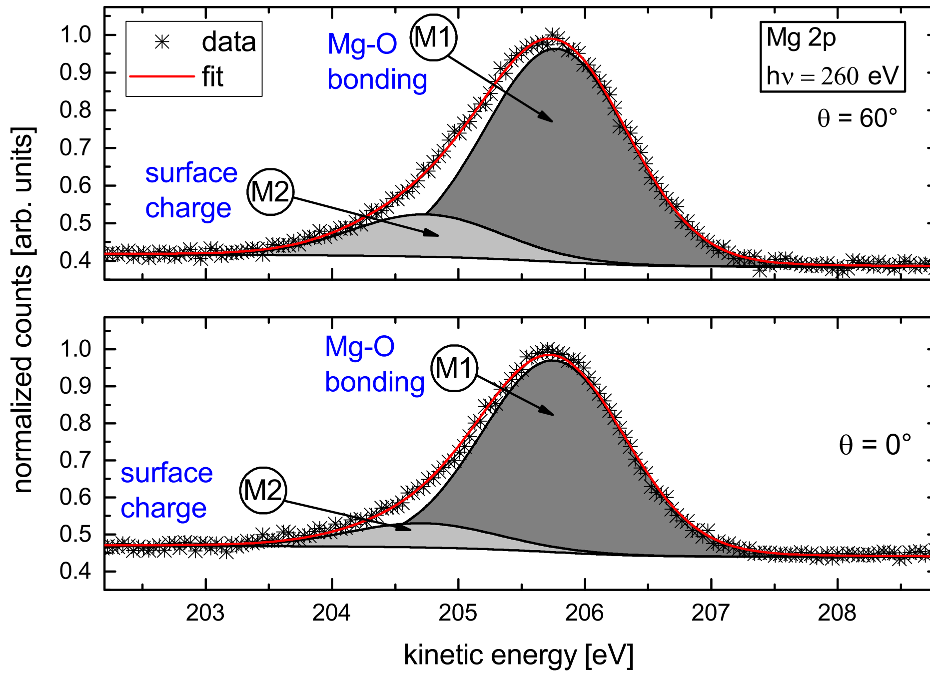

Figure 5.13: High resolution XPS spectra of Mg $2p$ after deposition 5 ML of MgO at $\theta = 60°$ (top) and $\theta = 0°$ (bottom). The spectra were recorded at an incoming photon energy of hν = 260 eV. Compared to M1, the surface component M2 rises from $\theta = 0°$ to $\theta = 60°$ by 6%. M1 corresponds to the main Mg-O bonding and M2 indicates a surface effect. The interpretation of each component is labeled in blue.

Since the relative area ratios in the Mg $2p$ XPS spectrum are the same for 3 ML-5 ML, it is derived that the deposited MgO film does not form any higher oxidation states like $Mg_xO_{1\text{-x}}$ or any compounds other than MgO. The Mg-O bonding remains intact for all thicknesses. This is further supported by the O_{1s}:Mg_{2p} ratio of 0.98:1 from the XPS survey spectrum, as stated in section 4.3. Since no additional peaks arise in Co $3p$ XPS spectrum, it is concluded that no bonding or oxidation occurs at the interface.

5.2.2 XPD Analysis

For the structural determination, Co 3*p* and Mg 2*p* XPD patterns are recorded after each evaporation step. First, the Co 3*p* XPD pattern is considered. The Co 3*p* XPD pattern before and after depositing 5 ML of MgO is shown in Fig. 5.14. A R-factor of $R = 0.049$ indicates a nearly perfect match between both experi-

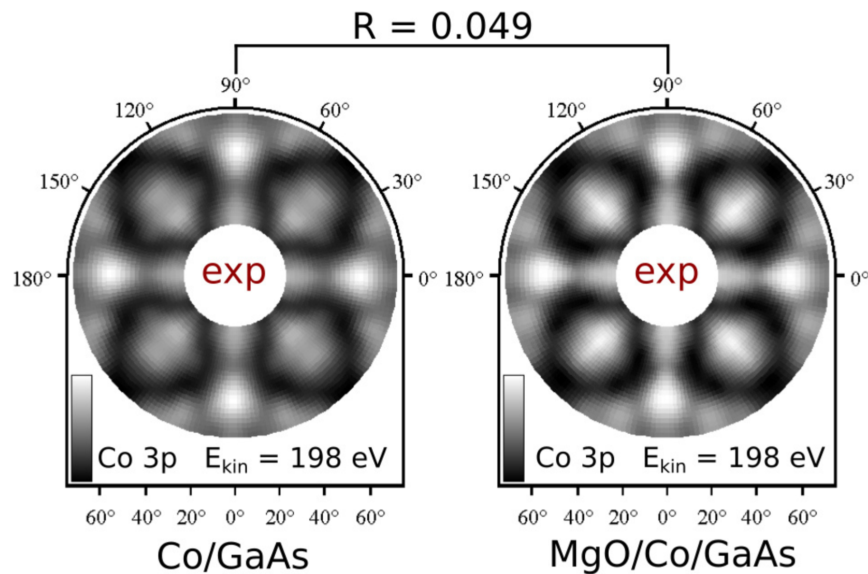

Figure 5.14: Co 3*p* pattern before (left) and after (right) depositing 5 ML of MgO. All Co 3*p* diffraction characteristics remain the same which is indicated by a R-factor of $R = 0.049$. Since the lattice constants of MgO(halite) and Co(bcc) do not match, averaging the diffraction patterns of all Co emitters cancels out every intensity modulation.

mental XPD patterns, i.e. the Co 3*p* XPD pattern does not change significantly after MgO deposition. At a first glance, one might conclude that MgO does not form a crystalline structure on top of Co(bcc), at which the emitted Co 3*p* photoelectrons can not be diffracted. Thus, that is the reason why Co 3*p* XPD pattern seems to remain unchanged for a MgO thickness of 5 ML. Considering the Mg 2*p* XPD pattern shown in Fig. 5.15, it becomes clear that this interpretation is misleading.

Indeed, the Mg 2p XPD pattern does not show any intensity modulations for film thicknesses of 3 ML and 4 ML. This clearly shows that MgO is amorphous for these thicknesses and thus the photoelectrons from the Co 3p orbital are not diffracted at a crystalline MgO structure. Therefore, the Co 3p pattern remains unchanged for these MgO thicknesses. But for a MgO film thickness of $t \geq 5\,\mathrm{ML}$ the Mg 2p XPD pattern reveals strong intensity modulations although the Co 3p pattern still remains unchanged. This behavior can be explained by a lattice mismatch of the crystalline MgO film on Co(bcc). For the lattice determination a qualitative XPD analysis is performed. The Mg 2p XPD patterns with incoming photon energies of $E_{\mathrm{kin}} = 260\,\mathrm{eV}$ and $E_{\mathrm{kin}} = 650\,\mathrm{eV}$ are recorded to cover the FSXPD and XPD regime. The obtained XPD patterns are shown in Fig. 5.15.

As stated in section 2.2.2, a structural assumption is necessary in order to use the genetic algorithm. From literature, it is well known that MgO grows in a halite structure, i.e. NaCl structure [38, 102]. Therefore, no further structure consideration is necessary. Yet, since the lattice constants of Co(bcc) $a_{\mathrm{Co}} = 2.83\,\text{Å}$ and pristine MgO $a_{\mathrm{MgO}} = 4.21\,\text{Å}$ do not match, a distortion for very low MgO thicknesses is taken into account. Although no structural reorientation or distortion is expected for Co(bcc), since the Co 3p XPD pattern remains unchanged, small atom displacements of up to 0.1 Å are considered within the genetic algorithm. Further, no Co oxidation or compound formation are considered, since the Co 3p XPS spectrum remains unchanged after MgO deposition as well. Still, in the discussion section 5.2.3 these options and CoO formation will be discussed in detail.

As a result, the structure presented in Fig. 5.16 is obtained. The R-factors for the FSXPD and XPD calculations are $R^{\mathrm{FSXPD}}_{\mathrm{Mg\ 2p}} = 0.052$ and $R^{\mathrm{XPD}}_{\mathrm{Mg\ 2p}} = 0.022$, respectively. These remarkably low R-factors of $R_i \ll 0.1$ for two different kinetic energies clearly show that the evaluated structure matches to the experimental data perfectly. Yet, it is also clear that the chemical sensitive XPD simulation reveals a highly distorted unit cell. For instance, every second layer of the MgO film is shifted by 0.22 Å into the $[00\bar{1}]$ direction making the unit cell asymmetric. In the [010] and [100] plane the lattice constant is compressed by 0.05 Å

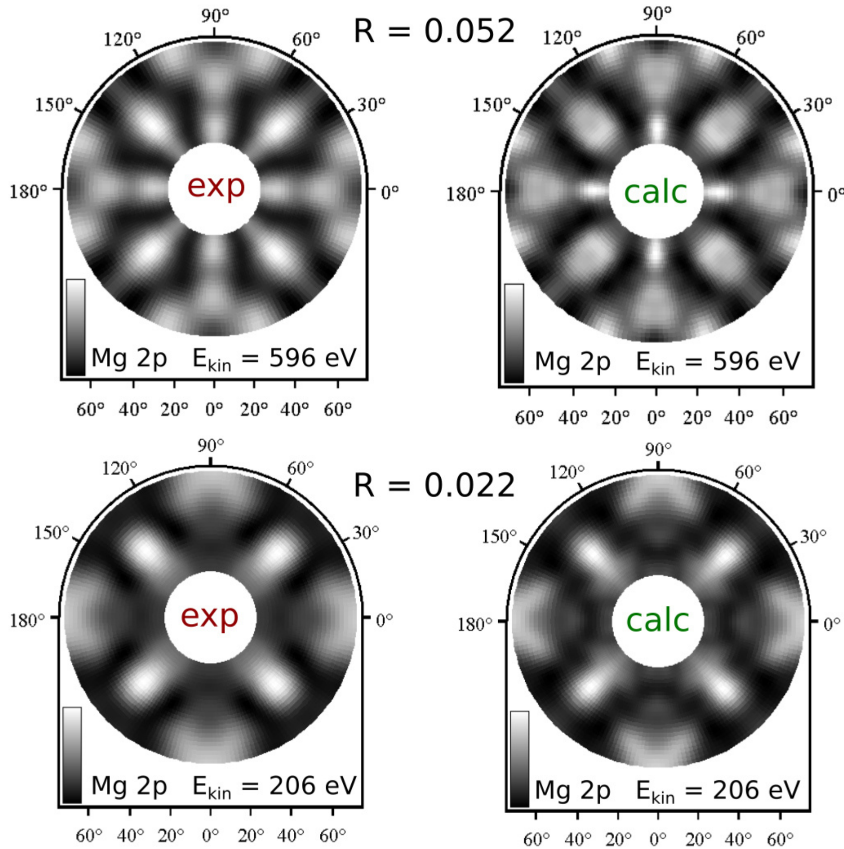

Figure 5.15: Mg 2*p* FSXPD (top) and XPD (bottom) pattern after depositing 5 ML of MgO. The patterns were recorded with incoming photon energies of hν = 650 eV and hν = 260 eV, respectively. A distorted halite structure results in astonishing R-factors of $R = 0.052$ and $R = 0.022$.

compared to bulk-typed MgO and, interestingly, stretched by 0.05 Å in [001] direction. Although a Co atom displacement of 0.1 Å is allowed within the genetic algorithm, the same Co(bcc) structure arises as presented for the Co/GaAs interface. This correlates with the finding, that the Co 3*p* XPS spectrum does not change after MgO deposition as well as the M1 component.

A main result here is that the in-plane lattice constant of MgO is slightly compressed to $a_{\mathrm{MgO}} = 4.16$ Å but still does not match the lattice constant of Co(bcc) $a_{\mathrm{Co}} = 2.83$ Å. This explains very well why the Co 3*p* XPD pattern recorded after

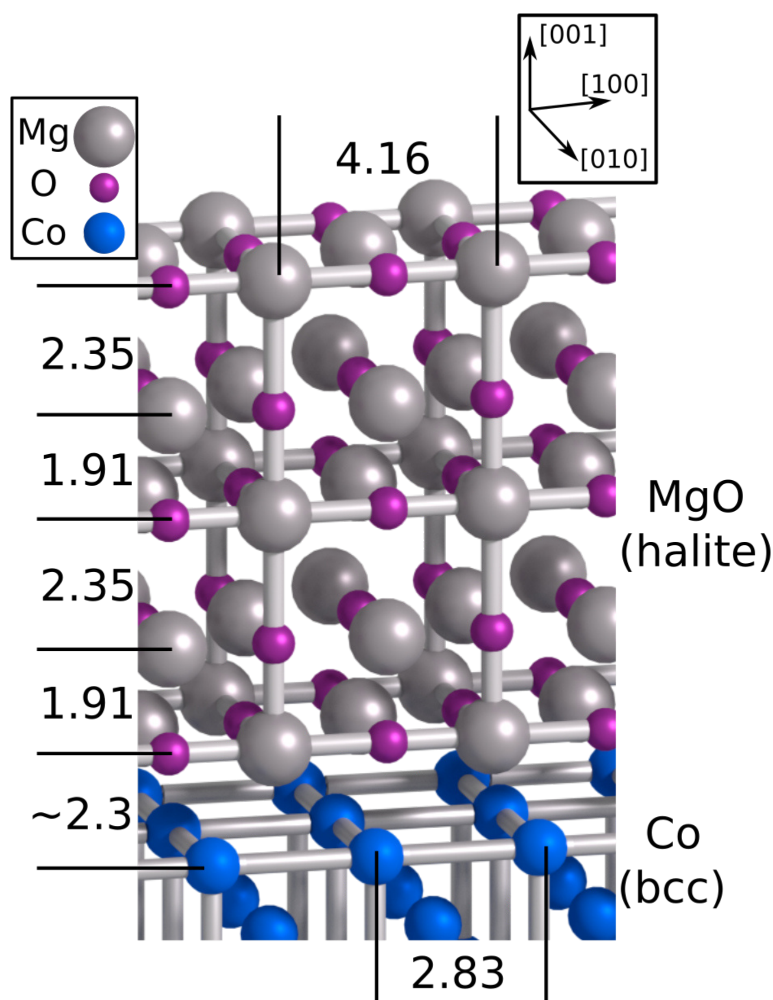

Figure 5.16: Resulting MgO/Co interface from the XPD analysis as shown in Fig. 5.15. The distance between Co(bcc) and MgO showed high experimental uncertaintybars. The Mg 2p XPS analysis yielded that every second MgO layer is shifted in $[00\bar{1}]$ direction by 0.22 Å. The lattice constants do not match and therefore a sharp interface is formed without any Co oxidation or compound formation.

depositing 5 ML of MgO does not change. Since the photon spot on the sample is $70 \times 30\,\mu\mathrm{m}^2$ in size, the recorded XPD pattern is averaged over $\approx 10^{10}$ unit cells. Further, as the diffraction pattern is highly sensitive to the near environment only due to the exponential decay of the electron wave, larger periodicities do not contribute to the experimental pattern. Considering the lattice mismatch,

each electron emitting Co atom is in a slightly different local environment with respect to the MgO molecules. Therefore, averaging over all Co atoms within the photon spot size, the crystalline MgO does not contribute to Co $3p$ XPD measurement, whereas in fact the Mg $2p$ XPD patterns themselves show clear intensity modulations. But this also means that the distance of Co(bcc) to MgO can only be estimated from angle-resolved XPS intensity measurements. This is performed according to

$$d = \lambda(E_{\text{kin}}) \cos(\theta) \times \ln \left(\frac{I_0(\theta)}{I'(\theta)} \right) \tag{5.1}$$

whereas the Co $3p$ intensity without MgO film I_0 and after deposition I' is recorded at a polar angle θ [116]. This is performed for several angles. The distance between Co(bcc) and MgO is then estimated by subtracting the thickness obtained from the XPD calculation from the thickness obtained from Eq. 5.1. The distance of $\approx 2.3\,\text{Å}$ is indicated in Fig. 5.16. Yet, the experimental uncertainty on this distance is significantly higher than the uncertainty on the lattice constants obtained from the XPD simulations. Since XPD is a highly near environment diffraction measurement, the uncertainty in lattice constant determination is as low as $0.01\,\text{Å}$ according to literature [31]. The uncertainty from calculations according to Eq. 5.1 mainly arise due to the IMFP. As stated in section 2.1.4, there are slight differences in the IMFP since it depends on the number of valence electrons, the atomic weight, bandgap and density of the material [56]. It even becomes more complex for multi-layer systems. Therefore, only an approximation can be performed with the presented fit curve. Since the experimental uncertainty on the IMFP contributes linearly to the estimated thickness the experimental uncertainty can be as large as $1\,\text{Å}$-$2\,\text{Å}$.

To sum up the results from the experiments performed on the MgO/Co interface, the deposited MgO layers are amorphous up to a thickness of $t \leq 4\,\text{ML}$ because the Mg $2p$ XPD patterns for 3 ML and 4 ML show no signs of intensity modulations. MgO crystallizes for thicknesses of $t \geq 5\,\text{ML}$. Thin MgO films show a distortion in lattice constant due to the lattice mismatch to Co(bcc). At the MgO/Co interface, Co(bcc) itself does not form any compounds nor does it

oxidize since the Co 3*p* XPS spectrum does not show any new peaks after MgO deposition. The Co 3*p* XPD patterns do not change for any MgO thickness due to the lattice mismatch of Co and MgO. These findings will be discussed in detail in section 5.2.3.

5.2.3 Discussion

Here, the XPS and XPD measurements show that Co does not oxidize after MgO deposition. Recently, Mallik *et al.* showed that thin Co films evaporated on MgO do not oxidize as well, which fits to the findings presented in this work [117]. Although no Co-O oxidation peaks arise in the Co 3*p* spectrum, a Co 3*p* XPD pattern is calculated for a single oxidized Co layer at the MgO/Co interface. The result is shown in Fig. 5.17.

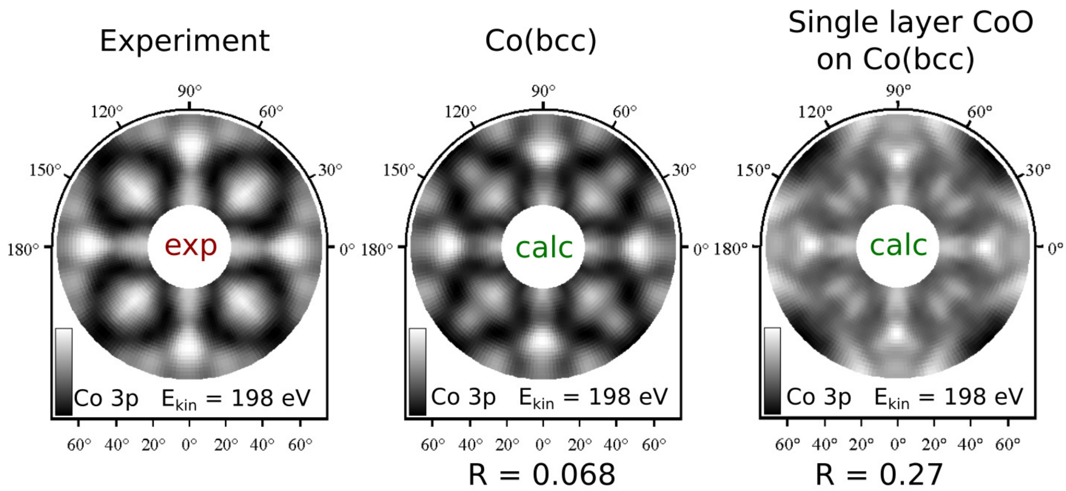

Figure 5.17: Comparison of the experimental Co 3*p* XPD pattern after MgO deposition (left), the calculated XPD pattern for a pristine Co(bcc) surface (middle), and a single CoO layer on Co(bcc).

A single CoO layer results in a much poorer R-factor of $R^{\mathrm{CoO}}_{\mathrm{Co\ 3p}} = 0.27$. This clearly shows that the XPD calculations match to the Co 3*p* XPS spectrum and no oxidation occurs at the interface. In contrast to Co, Fe forms small FeO islands at the MgO/Fe interface [118, 119]. Although Yuasa *et al.* showed clearly that it is possible to maintain unoxidized Fe beneath MgO, the necessary effort is tremendous making it unsuitable for applications [120]. Even small oxidized impurities lead to a heavy decrease of the TMR ratio making Fe less suitable for MTJs than Co.

A main result for the MgO/Co interface is that MgO is amorphous for $t \leq 4\,\mathrm{ML}$. Similar results have been shown for MgO grown on CoFeB. Therein, MgO is

amorphous up to a thickness of $t \leq 3\,\mathrm{ML}$ [121]. Yuasa *et al.* performed RHEED measurements. They showed that very faint diffraction spots appear after depositing 4 ML on amorphous CoFeB [121]. The RHEED spots become very strong for 5 ML. Since in this work MgO shows strong intensity modulations for a thickness of $t \geq 5\,\mathrm{ML}$ as well, it is clearly concluded that the crystallization of MgO is independent from the substrate. With this crystallized structure, MTJs were built with various MgO thicknesses of up to 2 nm [15, 119]. Yet, at these very low thicknesses when deposited on Co(bcc), a shift in every second MgO layer into the [001] direction by 0.22 Å occurs. Interestingly, a similar shift in every second MgO layer is also found when growing MgO on Fe(bcc) [86]. Therein, this shift does not occur in [001] direction but in [100] direction by 0.5 Å, i.e. a lateral shift. This might occur due to the difference in Co and Fe growth. Co grows almost perfectly apart from relaxations in each layer. In contrast, Fe grows in a pyramidal structure, i.e. a huge strain applies at the GaAs(001) surface. With every grown layer the strain gets smaller until bulked-type Fe(bcc) is grown [118]. For thin films the Fe-MgO lattice mismatch is as low as 0.8 Å, which is significantly smaller than the lattice mismatch presented here for MgO/Co derived from the XPD measurements. Bonell *et al.* support this interpretation [122]. They performed electron diffraction studies on MgO/FeV(bcc) and observed different MgO relaxations by varying the lattice match. Therefore, the relaxation of 0.22 Å for MgO layer on Co is explained well by lattice mismatch of 46%. Moreover, it can be generalized that MgO shows strong relaxations when evaporated on bcc metals.

Furthermore, the main XPS characteristics of Mg 2p are the same for MgO/Co(bcc) and MgO/Fe(bcc) [86]. Two peaks arise with an energetic shift of $\Delta E \approx 1\,\mathrm{eV}$. In previous studies, the main component was assigned to the Mg^{2+} bonding within the halite structure [86, 123, 124]. The interpretations of the minor component ranged from impurities during the electron beam evaporation process to bulk-state Mg-O bondings or Mg^0 state [29]. Yet, impurities can be ruled out, since the Mg:O ratio is observed to be $r \approx 1:1$. Further, Serin *et al.* showed clearly by TEM measurements that evaporating MgO granules by electron beam

epitaxy preserves the Mg-O bonding and crystalline structures are grown homogeneously [119]. A surface bonding has been ruled out in section 5.2.1.

To investigate the minor component M2, the Mg 2p XPD pattern is deconvolved. This time-consuming technique needs high resolution XPS spectra for each measured XPD point [60, 125, 126]. Each (θ_i, ϕ_j) XPS spectrum within the Mg 2p XPD pattern is fitted according to the Mg 2p XPS spectrum presented in Fig. 5.13. This yields two XPD patterns each corresponding the local environment of each XPS component. The result is presented in Fig. 5.18.

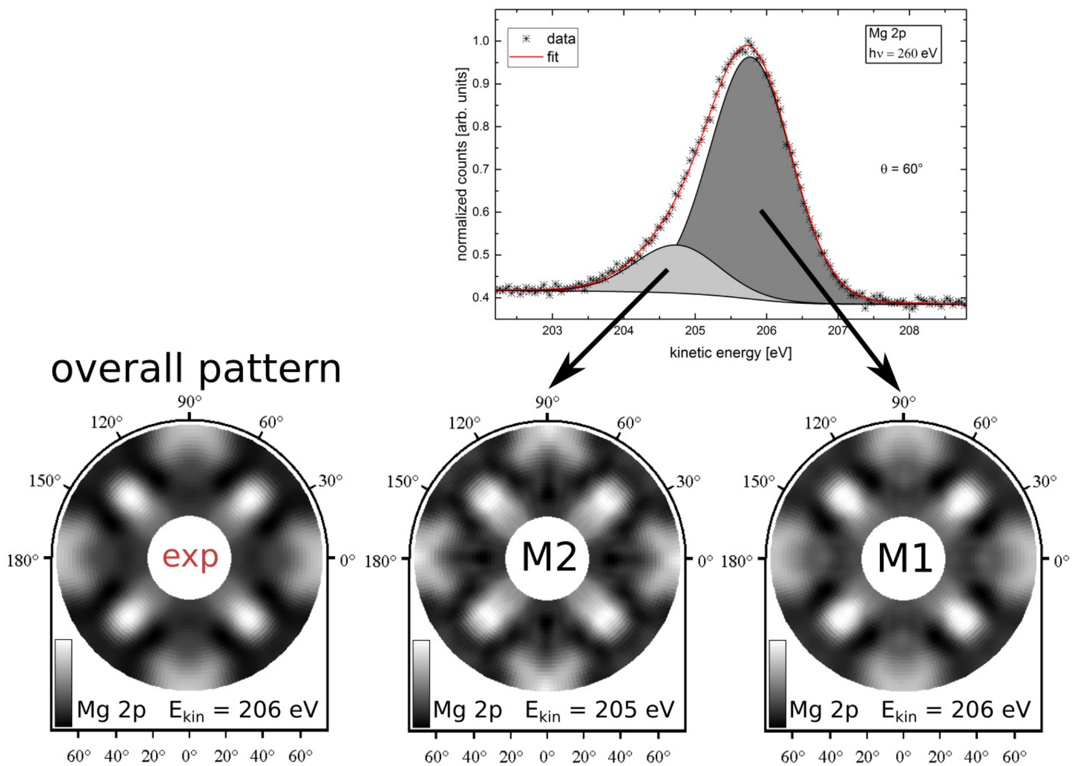

Figure 5.18: Deconvolution of the Mg 2p XPD pattern. The resulting XPD patterns corresponding to the M1 and M2 XPS components show the same intensity modulation for every (θ, ϕ) point. Further, they do not differ significantly from the overall Mg 2p XPD pattern. Therefore, the chemical environment for both components is the same.

It is expected that the two different bondings are located in different chemical environments since the binding energy differs by $\Delta E \approx 1\,\text{eV}$. Yet, the diffrac-

tion patterns corresponding to M1 and M2 are nearly identical according to a R-factor of $R_{\mathrm{M1,\,M2}} = 0.056$. Therefore, the local environments match as well. This is in clear contrast to previous interpretations for thin MgO films found in literature, since the minor Mg 2*p* XPS peak was always regarded as a different chemical bonding. Recently, Nelin *et al.* analyzed a MgO substrate with XPS. They suggested that a shift of $\approx 1\,\mathrm{eV}$ might occur due to a surface core-level binding energy shift for MgO [127]. A surface core-level shift occurs due to difference in the coordination number of the surface atoms compared the bulk atoms [128]. Depending on the valence electrons of the surface, the shifts occur to higher kinetic energies for a lower valence electron density and to lower kinetic energies for a higher valence electron density. Nelin *et al.* found a shift of 0.94 eV which matches perfectly to the shift of 1.03 eV observed here [127]. The small difference might occur since Nelin *et al.* performed their measurements with a Al K_α X-ray source. Therefore, the M2 components can clearly be assigned to the surface core-level shift of Mg^{2+}. Further, by deconvolving the XPD patterns it is concluded that the M1 and M2 component belong the same chemical environment. Similar behaviors for other insulators have not been reported yet since deconvolving an XPD pattern is a time-consuming technique that requires a very high resolution of each XPS spectrum in order to perform the deconvolution. But here, one can clearly tell that the M2 component corresponds to the Mg^{2+} bonding within the halite structure as well as the M1 component.

With this information at hand, the predicted and measured TMR ratios from the past years will be discussed in detail. Zhang *et al.* performed one of the earliest First Principle Calculations (FPC) on a MgO-based MTJ with Co and Fe as electrodes [17, 129]. They predicted a TMR ratio of $\approx 1000\,\%$ for Co/MgO/Co at room-temperature (RT). Yet, Yuasa *et al.* experimentally determined the TMR ratio for the same multi-layer system to be $\approx 410\,\%$ only [130]. From literature, it is well known that interface impurities or a high lattice mismatch lead to a significant TMR ratio reduction [19, 129]. From an experimental point of view, much effort has been put to reduce these defects [117, 131]. Yet, the theoretically predicted TMR ratio by Zhang *et al.* has never been achieved. In general, the predicted ratios in MgO-based MTJs are roughly larger by a factor of 2. In this

work, the Mg 2p XPD pattern reveals a highly distorted unit cell. Zhang *et al.* assumed the MgO unit cell lattice constant to be $a_{\mathrm{MgO}} = \sqrt{2} \times a_{\mathrm{Co(bcc)}} \approx 3.99\,\text{Å}$ due to the MgO-Co lattice mismatch. Further, they did not consider a relaxation of every second MgO layer as presented in this work. Here, the XPD simulations lead to an in-plane lattice constant of 4.16 Å which is $\approx 5\,\%$ larger than assumed. This might seem negligible at a first glance, but it has been shown that FPC and electron structure calculations for MTJs depend highly on the lattice (mis)match as well as on the structure of the tunneling barrier [132]. Moreover, since ultra-thin tunneling barriers are necessary to achieve efficient MTJs, the shift in every second MgO layer needs to be considered. As this shift breaks the symmetry within a unit cell, new FPC calculations can be performed with the structure obtained from FSXPD and XPD measurements. It is expected to significantly reduce the predicted TMR ratio of $\approx 1000\,\%$ in order to possibly match the experimental results.

6 Summary & Outlook

6.1 Summary

In summery, this thesis presents an in-depth interface analysis of MgO/Co(bcc)/GaAs(001) in terms of structural and chemical properties. The main results are summed up in Fig. 6.1. The Ga-rich c(8×2) GaAs(001) sur-

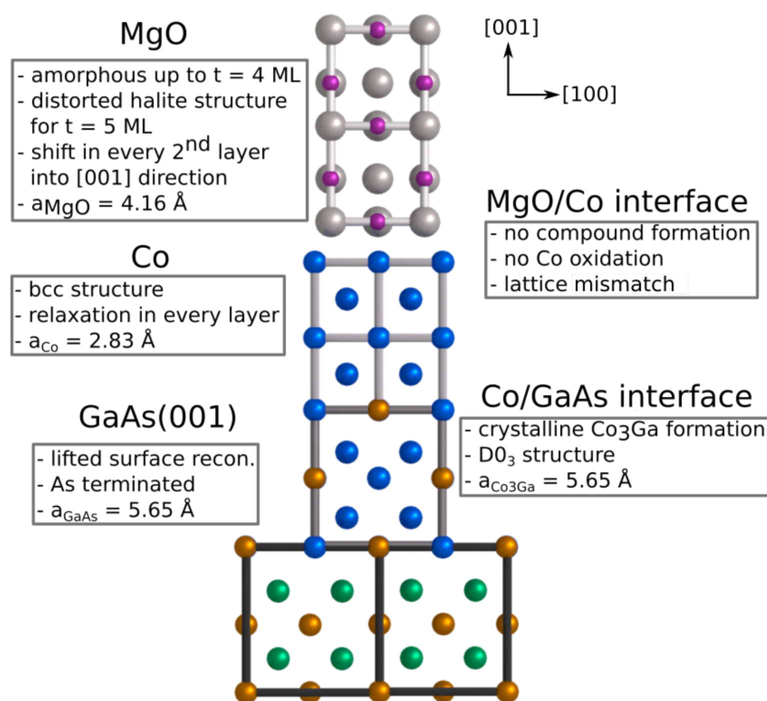

Figure 6.1: Conclusion from the x-ray photoelectron spectroscopy and x-ray photoelectron diffraction analysis for the MgO/Co/GaAs(001)-c(8×2) multi-layer system.

face reconstruction was successfully prepared and confirmed by LEED and XPS measurements. With the angle-resolved high resolution As 3d and Ga 3d XPS spectra the sub-surface Ga dimers and the $GaAs_3$ compound have been assigned to the fitted XPS components. After depositing 12 ML of Co all observed As 3d and Ga 3d XPS components vanished in favor of new strong bondings. The high resolution As 3d XPS spectrum shows minor As-As and Co_xGaAs_{1-x} compounds at the sample surface next to the main Co-As bonding. The high resolution Ga 3d XPS spectrum clearly showed two Ga bondings on top of each other within the Co/GaAs(001) interface region. The high resolution Co 3p XPS spectrum yielded that the Co-Ga bonding is located beneath the Co(bcc) bonding. Derived from the forward scattering XPD measurements, the Ga and Co atoms are located in the same structural environment. From that the possible interface structures were reduced to the $m\bar{3}m$ point group. To evaluate the near environment structure with chemical resolution, the As 3d, Ga 3d, and Co 3p full scattering XPD patterns at $E_{\mathrm{kin}} \approx 200\,\mathrm{eV}$ were taken into account. The As 3d XPD pattern showed no signs of intensity modulations, i.e. the compounds from the As 3d XPS measurement are clearly amorphous. The XPD calculations for the Ga 3d and Co 3p orbital yielded the lowest R-factors by far for a Co_3Ga alloy in a rare $D0_3$ structure sandwiched between Co(bcc) and As-terminated GaAs(001). The lattice constant of this alloy $a_{\mathrm{Co_3Ga}} = 5.65\,\mathrm{\AA}$ is the same as for a pristine GaAs(001) in zinc blende structure. The GaAs(001) surface reconstruction itself is lifted due to the alloy formation.

After depositing MgO, the Co 3p XPS spectrum did not change. Therefore, Co did not oxidize or form chemical bondings at the MgO/Co interface. Further, the Mg 2p XPS spectrum did not change for any MgO thickness, i.e. only two components were observed. MgO was epitaxially grown with a Mg:O ratio of 1:1 on Co. The Mg 2p forward scattering XPD and full scattering XPD patterns showed no signs of intensity modulations for a MgO thickness of $t \leq 4\,\mathrm{ML}$. Therefore, MgO is amorphous for these thicknesses. After depositing 5 ML of MgO, both Mg 2p patterns showed strong modulations. The resulted structure is a highly distorted halite structure wherein every second layer is shifted by $0.22\,\mathrm{\AA}$ in $[\bar{1}00]$. The in-plane lattice constant is compressed to $a_{\mathrm{MgO}} = 4.16\,\mathrm{\AA}$.

The Co $3p$ XPD pattern showed the same intensity modulations as for pristine Co for every MgO thickness. For a thickness of $t \leq 4\,\mathrm{ML}$, the Co $3p$ diffraction pattern corresponds to the Co structure only due to the missing near-field order within the MgO layers. For a thickness of $t \geq 5\,\mathrm{ML}$, the Co $3p$ diffraction remained unchanged although a crystalline MgO film was grown. This is due to the lattice mismatch of MgO and Co. The calculations showed that the MgO lattice constant and Co lattice constant differ by 46%. Therefore, each Co emitter is in slightly different local environment with respect to the MgO layers. Averaging this shift over the synchrotron spot size of $70 \times 30\,\mu\mathrm{m}^2$, no periodic local environment exists in terms of deposited MgO layers. Therefore, the Co $3p$ XPD pattern does not change although MgO is crystalline.

6.2 Outlook

Within in a decade the TMR effect became one of the most discussed phenomena in spintronic research. By exploring different combinations of tunneling electrodes such as Co, Fe, and CoFeB with tunneling barriers like MgO and Al_2O_3, the TMR effect at room temperature is pushed to even higher values. By understanding the physics of this phenomenon and building solid theories, TMR predictions and material exploration is performed more effectively. This work focused on this point in terms of exploring lower thickness limits and interface behaviors. The Co_3Ga alloy in $D0_3$ structure seems promising considering its magnetic and electronic properties. Therefore, a layer system consisting of Co_3Ga/GaAs only without any Co(bcc) can be investigated with T-MOKE or ARPES measurements in the future. With pulsed laser deposition or a dual evaporator, a constant Ga supply during Co evaporation can be ensured and by that higher Co_3Ga thicknesses can be prepared. Thus, a new tunneling electrode with a bcc-like structure can be created for MTJs.

For MgO as a tunneling barrier, it is clear that experimental and predicted TMR ratios differ mostly by a factor of 2. The distorted MgO unit cell for very low thicknesses used in MTJs leads to the suspicion that a yet unknown mechanism lowers the TMR ratio. Newer first principle calculations that consider the distortion might answer the question whether this particular behavior is the reason why the experimental TMR value is much lower than the predicted one. Further, in this work MgO/Co has been analyzed. Yet, for MTJs the Co/MgO interface is important as well. Thin layers of MgO might get distorted even further, when Co is deposited on them. Therefore, performing XPD measurements on the Co/MgO interface is necessary to fully cover the MgO analysis in terms of a possible unit cell distortion.

Bibliography

[1] Ikhtiar, H. Sukegawa, X. Xu, M. Belmoubarik, H. Lee, S. Kasai, and K. Hono, Appl. Phys. Lett. **112**, 022408 (2018).

[2] P. Zhao, J. Li, H. Jin, L. Yu, B. Huang, and D. Ying, Phys. Chem. Chem. Phys. **20**, 10286 (2018).

[3] T. Song, X. Cai, M. W.-Y. Tu, X. Zhang, B. Huang, N. P. Wilson, K. L. Seyler, L. Zhu, T. Taniguchi, K. Watanabe, M. A. McGuire, D. H. Cobden, D. Xiao, W. Yao, and X. Xu, Science **360**, 1214 (2018).

[4] T. Endoh, H. Koike, S. Ikeda, T. Hanyu, and H. Ohno, IEEE Journal on Emerging and Selected Topics in Circuits and Systems **6**, 109 (2016).

[5] J.-Y. Chen, Y.-C. Lau, J. M. D. Coey, M. Li, and J.-P. Wang, Sci. Rep. **7**, 42001 (2017).

[6] M. Julliere, Phys. Lett. **54**, 225 (1975).

[7] S. Yuasa and D. D. Djayaprawira, J. Phys. D: Appl. Phys. **40**, R337 (2007).

[8] S. Meena and S. Choudhary, Phys. Chem. Chem. Phys. **19**, 17765 (2017).

[9] J. P. Singh, S. Gautam, W. C. Lim, K. Asokan, B. B. Singh, M. Raju, S. Chaudhary, D. Kabiraj, D. Kanjilal, J.-M. Lee, J.-M. Chen, and K. H. Chae, Vacuum **138**, 48 (2017).

[10] G. Binasch, P. Grünberg, F. Saurenbach, and W. Zinn, Phys. Rev. B **39**, 4828 (1989).

[11] M. N. Baibich, J. M. Broto, A. Fert, F. N. Van Dau, F. Petroff, P. Etienne, G. Creuzet, A. Friederich, and J. Chazelas, Phys. Rev. Lett. **61**, 2472 (1988).

[12] T. Miyazaki and N. Tezuka, J. Magn. Magn. Mater. **139**, L231 (1995).

[13] J. S. Moodera, L. R. Kinder, T. M. Wong, and R. Meservey, Phys. Rev. Lett. **74**, 3273 (1995).

[14] L. Martins, J. Ventura, R. Ferreira, and P. Freitas, Appl. Surf. Sci. **424**, 58 (2017).

[15] H. Kubota, A. Fukushima, K. Yakushiji, T. Nagahama, S. Yuasa, K. Ando, H. Maehara, Y. Nagamine, K. Tsunekawa, D. D. Djayaprawira, N. Watanabe, and Y. Suzuki, Nat. Phys. **4**, 37 (2008).

[16] C.-F. Pai, M.-H. Nguyen, C. Belvin, L. H. Vilela-Leão, D. C. Ralph, and R. A. Buhrman, Appl. Phys. Lett. **104**, 082407 (2014).

[17] X.-G. Zhang and W. H. Butler, Phys. Rev. B **70**, 172407 (2004).

[18] H.-M. Tang and K. Xia, Phys. Rev. Applied **7**, 034004 (2017).

[19] S. Yuasa, T. Katayama, T. Nagahama, A. Fukushima, H. Kubota, Y. Suzuki, and K. Ando, Appl. Phys. Lett. **87**, 222508 (2005).

[20] M. Hoppe, S. Döring, M. Gorgoi, S. Cramm, and M. Müller, Phys. Rev. B **91**, 054418 (2015).

[21] S. S. P. Parkin, C. Kaiser, A. Panchula, P. M. Rice, B. Hughes, M. Samant, and S.-H. Yang, Nat. Mater. **3**, 862 (2004).

[22] D. Bagayoko, A. Ziegler, and J. Callaway, Phys. Rev. B **27**, 7046 (1983).

[23] T. Nozaki, H. Kubota, A. Fukushima, and S. Yuasa, Appl. Phys. Lett. **106**, 022405 (2015).

[24] J. Zhou, W. Zhao, S. Peng, J. Qiao, J. O. Klein, X. Lin, Y. Zhang, and A. Bournel, IEEE Trans. Magn. **53**, 1 (2017).

[25] T. A. Peterson, S. J. Patel, C. C. Geppert, K. D. Christie, A. Rath, D. Pennachio, M. E. Flatté, P. M. Voyles, C. J. Palmstrøm, and P. A. Crowell, Phys. Rev. B **94**, 235309 (2016).

[26] M. Bowen, V. Cros, F. Petroff, A. Fert, C. Martínez Boubeta, J. L. Costa-Krämer, J. V. Anguita, A. Cebollada, F. Briones, J. M. de Teresa, L. Morellón, M. R. Ibarra, F. Güell, F. Peiró, and A. Cornet, Appl. Phys. Lett. **79**, 1655 (2001).

[27] X. Jiang, R. Wang, R. M. Shelby, R. M. Macfarlane, S. R. Bank, J. S. Harris, and S. S. P. Parkin, Phys. Rev. Lett. **94**, 056601 (2005).

[28] R. Tholapi, I. A. Karateev, B. S. Roshchin, V. E. Asadchikov, T. Slobodskyy, W. Hansen, and A. L. Vasiliev, J. Appl. Phys. **121**, 205308 (2017).

[29] M. Müller, F. Matthes, and C. M. Schneider, J. Appl. Phys. **101**, 09G519 (2007).

[30] C. S. Fadley, Nucl. Instrum. Methods Phys. Res., Sect. A **601**, 8 (2009).

[31] L. H. de Lima, L. Barreto, R. Landers, and A. de Siervo, Phys. Rev. B **93**, 035448 (2016).

[32] M. Sagurton, E. L. Bullock, and C. S. Fadley, Surf. Sci. **182**, 287 (1987).

[33] M. Greif, T. Nagy, M. Soloviov, L. Castiglioni, M. Hengsberger, M. Meuwly, and J. Osterwalder, Struct. Dyn. **3**, 059901 (2016).

[34] J. Osterwalder, E. A. Stewart, D. Cyr, C. S. Fadley, J. Mustre de Leon, and J. J. Rehr, Phys. Rev. B **35**, 9859 (1987).

[35] H. Hertz, Ann. Phys. (Berl.) **267**, 983 (1887).

[36] W. Hallwachs, Ann. Phys. (Berl.) **269**, 301 (1888).

[37] A. Einstein, Ann. Phys. (Berl.) **322**, 132 (1905).

[38] C. Kittel, *Einführung in die Festkörperphysik*, 1st ed. (Oldenbourg Wissenschaftsverlag, Munich, Germany, 2006).

[39] P. Auger, J. Phys. Radium **6**, 205 (1925).

[40] D. A. Shirley, Phys. Rev. B **5**, 4709 (1972).

[41] S. Tougaard, Surf. Interface Anal. **11**, 453 (1988).

[42] X. Cui, C. Wang, A. Argondizzo, S. Garrett-Roe, B. Gumhalter, and H. Petek, Nat. Phys. **10**, 505 EP (2014).

[43] M. Repoux, Surf. Interface Anal. **18**, 567 (1992).

[44] R. Hesse, M. Weiß, R. Szargan, P. Streubel, and R. Denecke, J. Electron. Spectrosc. Relat. Phenom. **186**, 44 (2013).

[45] S. Doniach and M. Šunjić, J. Phys. C **3**, 285 (1970).

[46] K. Siegbahn, Rev. Mod. Phys. **54**, 709 (1982).

[47] A. Allred and E. Rochow, J. Inorg. Nucl. Chem. **5**, 264 (1958).

[48] T. Fließbach, *Quantenmechanik: Lehrbuch zur Theoretischen Physik III*, 5th ed. (Spektrum Akademischer Verlag, Berlin Heidelberg, Germany, 2008).

[49] W. Nolting, *Grundkurs Theoretische Physik 5/1: Quantenmechanik Grundlagen*, 7th ed. (Springer-Verlag, Berlin Heidelberg, Germany, 2013).

[50] P. R. Varekamp, M. C. Håkansson, J. Kanski, D. K. Shuh, M. Björkqvist, M. Gothelid, W. C. Simpson, U. O. Karlsson, and J. A. Yarmoff, Phys. Rev. B **54**, 2101 (1996).

[51] D. Mao, M. Santos, M. Shayegan, A. Kahn, G. Le Lay, Y. Hwu, G. Margaritondo, L. T. Florez, and J. P. Harbison, Phys. Rev. B **45**, 1273 (1992).

[52] A. Lebugle, U. Axelsson, R. Nyholm, and N. Mårtensson, Phys. Scripta **23**, 825 (1981).

[53] P. V. Attekum and J. Trooster, J. Electron Spectrosc. Relat. Phenom. **18**, 135 (1980).

[54] H. Shinotsuka, S. Tanuma, C. J. Powell, and D. R. Penn, Surf. Interface Anal. **47**, 871 (2015).

[55] B. Feuerbacher, B. Fitton, and R. Willis, *Photoemission and the electronic properties of surfaces*, 1st ed. (Wiley, Chichester, England, 1978).

[56] S. Tanuma, C. J. Powell, and D. R. Penn, Surf. Interface Anal. **43**, 689 (2011).

[57] M. P. Seah and W. A. Dench, Surf. Interface Anal. **1**, 2 (1979).

[58] A. Jablonski and C. Powell, J. Electron. Spectrosc. Relat. Phenom. **100**, 137 (1999).

[59] C. S. Fadley, J. Electron. Spectrosc. Relat. Phenom. **178-179**, 2 (2010).

[60] C. Westphal, Surf. Sci. Rep. **50**, 1 (2003).

[61] E. V. Shalaeva and M. V. Kuznetsov, J. Struct. Chem. **44**, 465 (2003).

[62] C. S. Fadley, Phys. Scr. **1987**, 39 (1987).

[63] C. S. Fadley and S. Nemšák, J. Electron. Spectrosc. Relat. Phenom. **195**, 409 (2014).

[64] C. Brundle, C. Evans, S. Wilson, and L. Fitzpatrick, *Encyclopedia of Materials Characterization: Surfaces, Interfaces, Thin Films*, braille ed., Characterization Series (Butxetworch-Heinemann, Stoneham, USA, 1992).

[65] M.-L. Xu, J. J. Barton, and M. A. Van Hove, Phys. Rev. B **39**, 8275 (1989).

[66] D. Mori, Y. Oyama, T. Hirose, T. Muro, and F. Matsui, Appl. Phys. Lett. **111**, 201603 (2017).

[67] D. P. Woodruff and A. M. Bradshaw, Rep. Prog. Phys. **57**, 1029 (1994).

[68] I. Razado-Colambo, J. Avila, D. Vignaud, S. Godey, X. Wallart, D. P. Woodruff, and M. C. Asensio, Sci. Rep. **8**, 10190 (2018).

[69] F. J. García de Abajo, M. A. Van Hove, and C. S. Fadley, Phys. Rev. B **63**, 075404 (2001).

[70] J. Pendry, Surf. Sci. **299-300**, 375 (1994).

[71] R. Döll and M. A. V. Hove, Surf. Sci. **355**, L393 (1996).

[72] T. Lühr, *Messung und Simulation von XPD-Mustern der Si(110)/SiO2-Grenzschicht*, Master's thesis, Technische Universität Dortmund, Dortmund (2009).

[73] K. Shamout, P. Espeter, P. Roese, R. Hönig, U. Berges, and C. Westphal, J. Phys. Condens. Matter **30**, 075003 (2018).

[74] M. Henzler and W. Göpel, *Oberflächenphysik des Festkörpers*, 1st ed., Teubner Studienbücher Physik (Vieweg+Teubner Verlag, Stuttgart, Germany, 1994).

[75] W. H. Preece, Proc. Royal Soc. Lond. **38**, 219 (1884).

[76] C. Davisson and L. H. Germer, Phys. Rev. **30**, 705 (1927).

[77] N. Ashcroft and N. Mermin, *Festkörperphysik*, 4th ed. (Oldenbourg Wissenschaftsverlag, Munich, Germany, 2011).

[78] W. H. Bragg and W. L. Bragg, Proc. Royal Soc. Lond. **88**, 428 (1913).

[79] *Focus GmbH*, "Efm 3 evaporator," (18 July 2018).

[80] P. Espeter, *Structure determination of silicon nano-ribbons by means of photoelectron spectroscopy and photoelectron diffraction*, Ph.D. thesis, Technische Universität Dortmund, Dortmund (2017).

[81] C. Westphal, U. Berges, S. Dreiner, R. Follath, M. Krause, F. Schäfers, D. Schirmer, and M. Schürmann, J. Electron. Spectrosc. Relat. Phenom. **144**, 1117 (2005).

[82] M. H. Engelhard, A. Lyubinetsky, and D. R. Baer, Surf. Sci. Spectra **23**, 83 (2016).

[83] K. Byung-Sub, C. Jean-Soo, K. Hee-Jae, and O. Suhk-Kun, Phys. Status Solidi **242**, 2447 (2005).

[84] D. Mao, M. Santos, M. Shayegan, A. Kahn, G. Le Lay, Y. Hwu, G. Margaritondo, L. T. Florez, and J. P. Harbison, Phys. Rev. B **45**, 1273 (1992).

[85] T. Soda, S. Minakawa, M. Ohtake, M. Futamoto, and N. Inaba, IEEE Trans. Magn. **51**, 1 (2015).

[86] D. Handschak, T. Lühr, F. Schönbohm, S. Döring, C. Keutner, U. Berges, and C. Westphal, Phys. Rev. B **88**, 045313 (2013).

[87] K. Lüdge, B. D. Schultz, P. Vogt, M. M. R. Evans, W. Braun, C. J. Palmstrøm, W. Richter, and N. Esser, J. Vac. Sci. Technol., B **20**, 1591 (2002).

[88] J. C. Thomas, A. Van der Ven, J. M. Millunchick, and N. A. Modine, Phys. Rev. B **87**, 075320 (2013).

[89] P. Drathen, W. Ranke, and K. Jacobi, Surf. Sci. **77**, L162 (1978).

[90] X. Hou, G. Dong, X. Ding, and X. Wang, J. Phys. C: Solid State Phys. **20**, L121 (1987).

[91] W. G. Schmidt, P. H. Hahn, and F. Bechstedt, in *High Performance Computing in Science and Engineering '01*, edited by E. Krause and W. Jäger (Springer, Berlin, Heidelberg, 2002) pp. 178–188.

[92] G. A. Prinz, Phys. Rev. Lett. **54**, 1051 (1985).

[93] S. J. Blundell, M. Gester, J. A. C. Bland, C. Daboo, E. Gu, M. J. Baird, and A. J. R. Ives, J. Appl. Phys. **73**, 5948 (1993).

[94] K. Lüdge, P. Vogt, W. Richter, B.-O. Fimland, W. Braun, and N. Esser, J. Vac. Sci. Technol. B **22**, 2008 (2004).

[95] J. J. Yeh and I. Lindau, At. Data Nucl. Data Tables **32**, 1 (1985).

[96] A. Ohtake, S. Tsukamoto, M. Pristovsek, N. Koguchi, and M. Ozeki, Phys. Rev. B **65**, 233311 (2002).

[97] A. Ohtake, Surf. Sci. Rep. **63**, 295 (2008).

[98] C. Kumpf, L. D. Marks, D. Ellis, D. Smilgies, E. Landemark, M. Nielsen, R. Feidenhans'l, J. Zegenhagen, O. Bunk, J. H. Zeysing, Y. Su, and R. L. Johnson, Phys. Rev. Lett. **86**, 3586 (2001).

[99] M. Larive, G. Jezequel, J. Landesman, F. Solal, J. Nagle, B. Lépine, A. Taleb-Ibrahimi, G. Indlekofer, and X. Marcadet, Surf. Sci. **304**, 298 (1994).

[100] G. Cossu, G. Ingo, G. Mattogno, G. Padeletti, and G. Proietti, Appl. Surf. Sci. **56-58**, 81 (1992).

[101] F. Sirotti, M. De Santis, and G. Rossi, Phys. Rev. B **48**, 8299 (1993).

[102] R. Groß, *Festkörperphysik*, 1st ed. (Oldenbourg Wissenschaftsverlag, Munich, Germany, 2012).

[103] F. Xu, J. J. Joyce, M. W. Ruckman, H.-W. Chen, F. Boscherini, D. M. Hill, S. A. Chambers, and J. H. Weaver, Phys. Rev. B **35**, 2375 (1987).

[104] T. L. Monchesky and J. Unguris, Phys. Rev. B **74**, 241301 (2006).

[105] Y. Z. Wu, H. F. Ding, C. Jing, D. Wu, G. L. Liu, V. Gordon, G. S. Dong, X. F. Jin, S. Zhu, and K. Sun, Phys. Rev. B **57**, 11935 (1998).

[106] Y. Wu, H. Ding, C. Jing, D. Wu, G. Dong, X. Jin, K. Sun, and S. Zhu, J. Magn. Magn. Mater. **198-199**, 297 (1999).

[107] J. Herfort, H.-P. Schönherr, and K. H. Ploog, Appl. Phys. Lett. **83**, 3912 (2003).

[108] A. Hirohata, W. Frost, M. Samiepour, and J.-Y. Kim, Materials **11** (2018).

[109] Y. Manzke, J. Herfort, and M. Ramsteiner, Phys. Rev. B **96**, 245308 (2017).

[110] P. Bruski, S. C. Erwin, J. Herfort, A. Tahraoui, and M. Ramsteiner, Phys. Rev. B **90**, 245150 (2014).

[111] I. Golovin, V. Palacheva, A. Bazlov, J. Cifre, N. Nollmann, S. Divinski, and G. Wilde, J. Alloys Compd. **656**, 897 (2016).

[112] M. E. Jamer, B. A. Assaf, G. E. Sterbinsky, D. Arena, L. H. Lewis, A. A. Saúl, G. Radtke, and D. Heiman, Phys. Rev. B **91**, 094409 (2015).

[113] X. Chen, Y. Huang, and H. Chen, RSC Adv. **7**, 44647 (2017).

[114] K. Miyokawa, S. Saito, T. Katayama, T. Saito, T. Kamino, K. Hanashima, Y. Suzuki, K. Mamiya, T. Koide, and S. Yuasa, Jpn. J. Appl. Phys. **44**, L9 (2005).

[115] R. Jerome, P. Teyssie, J. Pireaux, and J. Verbist, Appl. Surf. Sci. **27**, 93 (1986).

[116] J. Watts and J. Wolstenholme, *An Introduction to Surface Analysis by XPS and AES*, 1st ed. (Wiley, Chichester, England, 2003).

[117] S. Mallik, S. Mallick, and S. Bedanta, J. Magn. Magn. Mater. **428**, 50 (2017).

[118] D. Krull, M. F. Tesch, F. Schönbohm, T. Lühr, C. Keutner, U. Berges, H.-C. Mertins, and C. Westphal, Appl. Surf. Sci. **367**, 391 (2016).

[119] V. Serin, S. Andrieu, R. Serra, F. Bonell, C. Tiusan, L. Calmels, M. Varela, S. J. Pennycook, E. Snoeck, M. Walls, and C. Colliex, Phys. Rev. B **79**, 144413 (2009).

[120] S. Yuasa, A. Fukushima, T. Nagahama, K. Ando, and Y. Suzuki, Jpn. J. Appl. Phys. **43**, L588 (2004).

[121] S. Yuasa, Y. Suzuki, T. Katayama, and K. Ando, Appl. Phys. Lett. **87**, 242503 (2005).

[122] F. Bonell and S. Andrieu, Surf. Sci. **656**, 140 (2017).

[123] M. Sicot, S. Andrieu, F. Bertran, and F. Fortuna, Phys. Rev. B **72**, 144414 (2005).

[124] J. Du, L. Zhang, E. Fu, X. Ding, K. Yu, Y. Wang, Y. Wang, J. Baldwin, X. Wang, and P. Xu, Appl. Surf. Sci. **410**, 585 (2017).

[125] S. Ulstrup, P. Lacovig, F. Orlando, D. Lizzit, L. Bignardi, M. Dalmiglio, M. Bianchi, F. Mazzola, A. Baraldi, R. Larciprete, P. Hofmann, and S. Lizzit, Surf. Sci. **678**, 57 (2018).

[126] P. Espeter, C. Keutner, P. Roese, K. Shamout, U. Berges, G. Wenzel, L. Bignardi, N. F. Kleimeier, H. Zacharias, and C. Westphal, Nanotechnology **28**, 455701 (2017).

[127] C. J. Nelin, F. Uhl, V. Staemmler, P. S. Bagus, Y. Fujimori, M. Sterrer, H. Kuhlenbeck, and H.-J. Freund, Phys. Chem. Chem. Phys. **16**, 21953 (2014).

[128] S. Hüfner, *Photoelectron Spectroscopy*, 3rd ed. (Springer-Verlag, Berlin, 2003).

[129] W. H. Butler, X.-G. Zhang, T. C. Schulthess, and J. M. MacLaren, Phys. Rev. B **63**, 054416 (2001).

[130] S. Yuasa, A. Fukushima, H. Kubota, Y. Suzuki, and K. Ando, Appl. Phys. Lett. **89**, 042505 (2006).

[131] S. Andrieu, F. Bonell, T. Hauet, F. Montaigne, L. Calmels, E. Snoeck, P. Lefevre, and F. Bertran, J. Appl. Phys. **115**, 172610 (2014).

[132] W. H. Rippard, A. C. Perrella, F. J. Albert, and R. A. Buhrman, Phys. Rev. Lett. **88**, 046805 (2002).

Publications

Articles

1. P. Espeter, C. Keutner, N.F. Kleimeier, P. Roese, K. Shamout, G.Wenzel, U. Berges, H. Zacharias, and C. Westphal, *Structure determination of silicene nanoribbons on Ag(110)*, TechConnect Briefs: Advanced Materials **1**, (2017)

2. P. Espeter, C. Keutner, P. Roese, K. Shamout, U. Berges, G. Wenzel, L. Bignardi, N. F. Kleimeier, H. Zacharias, and C. Westphal, *Facing the interaction of absorbed silicon nano-ribbons on silver*, Nanotechnology **28**, 455701 (2017)

3. K. Shamout, P. Espeter, P. Roese, R. Hönig, U. Berges, and C. Westphal, *Revealing the interfaces of the hybrid system MgO/Co/GaAs(001): a structural and chemical investigation with XPS and XPD*, J. Phys. Condens. Matter **30**, 075003 (2018)

4. R. Hönig, P. Roese, K. Shamout, T. Ohkochi, U. Berges, C. Westphal *Structural, Chemical, and Magnetic Properties of Cobalt Intercalated Graphene on Silicon Carbide*, Nanotechnology **30**, 025702 (2019)

5. P. Roese, K. Shamout, P. Espeter, R. Hönig, U. Berges, C. Westphal *Structure determination of substrate influenced silicon nano-ribbon growth*, Appl. Surf. Sci. (2019)

6. W. Tillmann, D. Stagnier, P. Roese, K. Shamout, U. Berges, C. Westphal *On the structural and mechanical properties of carbon incorporation in DC/HiPIMS CrAlN coatings*, (submitted 2018)

Acknowledgment - Danksagung

An dieser Stelle möchte ich mich bei denjenigen bedanken, die mich unterstützt haben diese Dissertation zu erarbeiten und zu verfassen.

In erster Linie danke ich Herrn Prof. Dr. Carsten Westphal, der mir nicht nur als Doktorvater diente sondern auch als akademischer und menschlicher Mentor. Dadurch entwickelte ich eine große Begeisterung für die experimentelle Oberflächenphysik, die sehr lange anhalten wird. Weiterhin danke ich Ihnen dafür, dass Sie selbstlos meine eigenen Forschungsziele unterstützt haben, um so meine charakterliche Entwicklung voranzutreiben. Anfangs sehr impulsiv, habe ich dank Ihnen gelernt im akademischen Feld diplomatischer und durchdachter zu handeln.

Herrn Mirko Cinchetti danke ich nicht nur für das Zweitgutachten, sondern auch für seine Expertise in der Oberflächenphysik. Durch sein Engagement im Kolloquium und bei Konferenzen, habe immer wieder Impulse erhalten, um über den Tellerrand hinauszuschauen und so meine Arbeit in einem größeren Kontext zu sehen.

Ich bedanke mich bei der gesamten Arbeitsgruppe EIb für das kollegiale und freundschaftliche Arbeitsverhältnis in den vergangen Jahren. Der Großteil meines Dankes gilt meinen beiden Büro-Freunden Peter Roese und Philipp Espeter. Ohne euch wäre diese Arbeit sicherlich nicht so entstanden. Dank euch war ich jeden Tag motiviert die Experimente durchzuführen und auch die Theorie dahinter zu verstehen. Diese Motivierung entstand nicht nur durch sachliche und fachliche Inhalte sondern auch durch Diskussionen über Politik, Moral, Arbeits- und Lebenseinstellungen und viel mehr. Egal wie die einzelnen Projekte verliefen - mit Humor schafft man alles.

Dem DELTA Personal bin ich dankbar für jedes einzelne Photon und die detaillierten Erklärung aller Mechanismen am DELTA.

Besonderes möchte ich meiner Familie und meiner Freundin danken, die mich moralisch, mental und fachlich in den vergangen Jahren unterstützt haben. Ihr habt mich im Guten und im Schlechten ertragen. Ohne euch hätte ich es definitiv nicht geschafft.

Danke Sehr